Carlota Pereira de
Almeida Carlos

**Espectroscopia óptica avançada de novos materiais
para concentradores solares luminescentes**

**Advanced optical spectroscopy of new materials for
luminescent solar concentrators**

Carlota Pereira de
Almeida Carlos

Espectroscopia óptica avançada de novos materiais para concentradores solares luminescentes

Advanced optical spectroscopy of new materials for luminescent solar concentrators

COMPETE 2020   PORTUGAL 2020   UNIÃO EUROPEIA Fundo Europeu de Desenvolvimento Regional

Aos meus pais,
à Laura e à Matilde.

o júri / the jury

presidente / president   **Prof. Doutor Leonel Marques Vitorino Joaquim**
Professor Associado da Universidade de Aveiro

vogais / examiners committee   **Prof. Doutora Maria Rute de Amorim e Sá Ferreira André**
Professora Associada com Agregação da Universidade de Aveiro

Doutora Ana Maria de Matos Charas
Investigadora Sénior do Instituto de Telecomunicações

agradecimentos

Em primeiro lugar, gostaria de agradecer à Professora Doutora Maria Rute André e à Doutora Jana Neider, pela permanente disponibilidade, orientação e apoio que incansavelmente proporcionaram ao longo deste percurso. Deixo ainda o meu agradecimento por todo o conhecimento transmitido, que contribuiu não só para o crescimento e desenvolvimento deste trabalho, como também para o meu, a nível académico e pessoal.

Da mesma forma, quero agradecer à Doutora Sandra Correia e ao Doutor Oleksandr Savchuk pelo apoio na caracterização dos materiais luminescentes e por toda a partilha de conhecimento e experiência.

Ao Doutor Lianshe Fu, pela síntese dos materais híbridos. À Mestre Marita Alves Cardoso e à Dr Rita Frias pela ajuda prestada na síntese dos materiais e por toda a disponibilidade demonstrada.

Agradeço ainda ao INL - International Iberian Nanotechnology Laboratory a oportunidade de desenvolver trabalho nas suas instalações e toda a disponibilidade demonstrada.

Num tom mais pessoal, quero ainda agradecer a todos os amigos que fiz durante o meu percurso académico, por me terem acompanhado ao longo destes cinco anos e por todos os momentos de convívio que isso implica.

Ao Pedro Mealha, por toda a ajuda prestada ao longo deste ano, assim como aos amigos de sempre.

Ao Pedro e à Beatriz, pelo companheirismo e simpatia, que tornaram a adaptação a uma cidade nova tão mais fácil.

Um agradecimento especial ao Luís, pela companhia constante nas incontáveis noites de estudo, e à Ana Luís, pela amizade e todo o apoio. A ambos por me fazerem sentir em casa.

Por fim, um enorme obrigada à minha família, particularmente aos meus pais, pelo amor e apoio incondicional que me guiaram até hoje.

Palavras-chave

Energia fotovoltaica, edifícios de energia zero, sustentabilidade, concentrador solar luminescente, eficiência ótica de conversão, eficiência quântica externa, híbrido orgânico-inorgânico, corantes orgânicos naturais.

Resumo

A transição da matriz energética atual para fontes de energia competitivas de baixo impacto ambiental é uma problemática central no século XXI. A arquitetura energeticamente sustentável é um ponto estratégico nesse esforço, através da realização dos chamados edifícios de energia zero. Por definição, estes edifícios fazem uso de sistemas de produção de energia renovável local, como por exemplo a fotovoltaica, para satisfazer as suas necessidades energéticas. Assim, novas tecnologias que integrem dispositivos de coleção de energia solar em edifícios existentes ou recém-construídos são de crescente relevância.

Os concentradores solares luminescentes são dispositivos compostos por uma matriz transparente com centros óticos ativos incorporados. Estes absorvem a radiação incidente, que é posteriormente reemitida com um comprimento de onda específico e transportada por reflexão interna total até à célula fotovoltaica localizada nas extremidades da matriz. Esta configuração permite a produção de dispositivos fotovoltaicos incorporados em fachadas de edifícios e janelas, permitindo que estes sejam transformados em unidades de produção de energia.

Atualmente, um dos desafios na áreas dos concentradores solares luminescentes é a incorporação de moléculas orgânicas naturais como centros óticos. Neste âmbito, foram fabricados e processados híbridos orgânico-inorgânicos semitransparentes, denominados por ureiasils, modificados por dois corantes orgânicos naturais, clorofila e proteína verde fluorescente (eGFP). A dinâmica entre os estados excitados dos corantes naturais e da matriz híbrida foi estudada e caracterizada - foram identificadas as bandas de absorção da clorofila *a* e da eGFP, assim como a sua emissão característica no vermelho/infravermelho próximo (600-750 nm) e na região do visível (450-600 nm), respetivamente. As propriedades de emissão foram quantificadas através de medidas de rendimento quântico absoluto, registando-se um valor máximo para o híbrido com eGFP incorporada (0,33±0,03) duas vezes superior ao encontrado para as matrizes híbridas dopadas com clorofila (0,15±0,02). Foram também analisados os tempos de vida dos emissão dos estados excitados das várias amostras, tendo sido encontrados valores ∼5 ns para a clorofila e ∼2-3 ns para a eGFP, em solução ou quando incorporadas nas matrizes híbridas. Procedeu-se ainda a uma análise mais aprofundada no caso das amostras com eGFP, através da aplicação de um modelo bi-exponencial às curvas de decaimento, uma vez que o modelo eletrónico da mesma indica a presença de dois estados excitados distintos responsáveis pela absorção em torno dos 488 nm e emissão a 510 nm.

Devido às características fotoluminescentes interessantes das amostras à base de corantes naturais para aplicações em concentradores solares luminescentes, foram fabricados e caracterizados dois protótipos com geometria planar – um concentrador solar luminescente baseado num recipiente de vidro cheio com eGFP em solução aquosa, e um outro concentrador que consistia num monolito da matriz híbrida dopada com eGFP. Os dispositivos foram acoplados a uma célula fotovoltaica comercial de silício, revelando eficiências óticas de conversão máximas de $2,99 \pm 0,01\%$ e $3,70 \pm 0,06\%$, respetivamente, ilustrando o potencial desta abordagem para o desenvolvimento de sistemas energéticos sustentáveis e competitivos.

Abstract

The transition from the current energy matrix towards an environmentally friendly and affordable energy sources is a crucial challenge of the 21st century. Fully energetically sustainable architecture is a strategic focus in this effort, through the realisation of so-called net-zero energy buildings. This implies an increase in the use of renewable resources, such as the wind, tides and the sun. Hence, new technologies that integrate solar-harvesting devices into existing and newly constructed buildings are of growing relevance.

Luminescent solar concentrators consist of a transparent matrix doped or coated with active optical centres that absorb the incident solar radiation, which is re-emitted at a specific wavelength and transferred by total internal reflection to the edges, where photovoltaic cells are located. This configuration enables photo-voltaic devices to be embedded in building facades or windows, allowing them to be transformed into energy harvesting units.

Challenges for the luminescent species in luminescent solar concentrators include the use of sustainable, natural-based organic molecules. In this scope, semi-transparent amine-functionalized organic–inorganic hybrids (ureasils) incorporating two different natural-based organic dyes, chlorophyll and enhanced fluorescent protein (eGFP), were synthesised and processed as thin films and monoliths. The natural dyes' and organic-inorganic hybrid's excited state dynamics were studied and characterised – the absorption bands of chlorophyll *a* and eGFP were identified, as well as their characteristic emission in the red/NIR (600-750 nm) and visible (450-600 nm) spectral regions, respectively. The emission properties were further quantified through absolute emission quantum yield measurements, with the maximum values measured for the eGFP-doped di-ureasil hybrid (0.33 ± 0.03) being two times higher than the maximum value found for the chlorophyll-doped hybrid samples (0.15 ± 0.02). Fluorescent lifetime analysis was also performed resorting to two different techniques: time-correlated single photon counting and spectrally-resolved streak imaging, yielding fluorescent emission lifetimes of ~5 ns for chlorophyll and ~2-3 ns for enhanced green fluorescent protein, in solution and when incorporated into the hybrid hosts. Further analysis was carried out by fitting a two exponential decay model to the fluorescent decay curves of the for the green fluorescent protein samples, considering that two distinct electronic states are responsible for the absorption around 488 nm and the emission at 510 nm.

Based on the intriguing photoluminescent features of the dye-based samples, two prototypes of luminescent solar concentrators were fabricated and optically characterised. In particular, a liquid planar luminescent solar concentrator based on a glass container filled with eGFP dispersed in an aqueous solution and a eGFP-doped di-ureasil hybrid bulk planar luminescent solar concentrator. The devices were coupled to a silicon-based commercial PV device, revealing maximum optical conversion efficiencies of $2.99 \pm 0.01\%$ (liquid) and $3.70 \pm 0.06\%$ (bulk), illustrating the potential of this approach for the development of nature-based luminescent solar concentrators, meeting the requirements of reliable, sustainable and competitive energy systems.

Contents

1.   Introduction

Concerns regarding present energy systems are currently growing due to the increase in global demand, Figure 1.1(a), in parallel with the possible collapse of fossil fuel-based sources – worldwide energy consumption is projected to increase by more than 40% by 2040 [1] and the demand for fossil fuels is expected to exceed annual production [2, 3]. On December 12th, 2015, Parties to the United Nations Framework Convention on Climate Change reached a landmark accord to combat the climate crisis, agreeing in the intensification of actions and investments needed to strengthen the global response to this phenomena. Through greenhouse gas emissions mitigation, the goal of the Paris Agreement is to keep the global temperature rise in the 21st century below 2°C above pre-industrial levels, calling for efforts to limit this increase even further (1.5°C). However, future projections based on the environmental policies currently in place are far from the ideal – CO_2 emissions increased in 2017 after plateauing for three years, Figure 1.1(b) – attesting that much is still needed to be done to accomplish these goals. Thus, the development of new, sustainable and environmentally friendly energy sources is of great importance.

An important player in the transformation of the present energetic matrix is solar energy. The sun is an indigenous and inexhaustible resource that can be harnessed nearly everywhere in the world. Additionally, solar irradiation on Earth in just one year is one order of magnitude greater than all the estimated non-renewable energy resources, including fossil fuels and nuclear [2], and four orders of magnitude higher than the world's total annual primary energy consumption, Figure 1.1(c), showcasing the great potential of the Sun to help fulfil global needs.

One way to harness solar energy is through photovoltaic (PV) cells, that capture and convert solar photons into electricity. Although fossil fuels are projected to dominate the future energy production landscape, this technology shows great promise for evolution in the upcoming years. The continuous increase in performance of silicon-based photovoltaic (Si-PV) systems, together with the economic incentive programmes adopted by several countries, have rendered PV a low-cost, dominant technology for producing electrical energy from renewable sources [6, 7], considerably
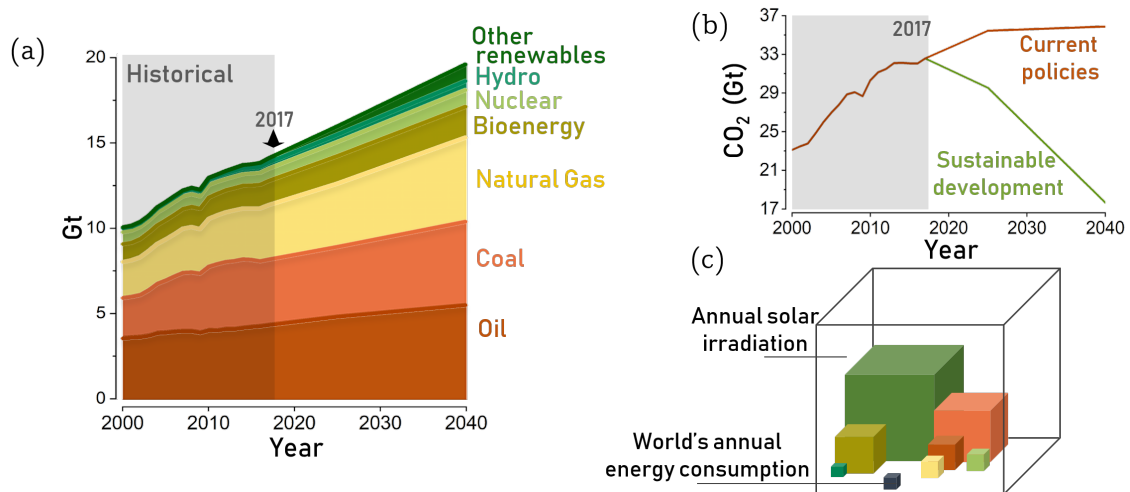
Figure 1.1: World's energy outlook. (a) Historical and future projections of global primary energy demand by energy source, in gigatonnes (Gt) of oil equivalent, based on the policies in place today. (b) Future projections of energy-related CO_2 emissions based on current policies versus the ones needed to fulfil the goals of the Paris Agreement (data source: ref. [4]). (c) World's energy consumption in comparison to the annual solar energy irradiated onto the surface of the Earth and the other resources in figure (a), identified by the same colour code. Fossil fuels are expressed with regard to their total reserves, while renewable energies to their yearly potential. Adapted from [5].

diminishing the gap between the cost of electricity generated by fossil fuels and renewable sources, and setting solar PV to be one the most deployed power generation technologies, with installed capacity projected to overtake wind, hydropower and coal before 2040 [4].

Despite the recent developments in PV systems, this technology still needs to evolve in order to efficiently compete with the traditional energy sources and achieve market acceptance. For individual houses and small buildings, microgeneration energy technologies such as rooftop photovoltaics are sufficient to meet electricity, heating and cooling demands. The situation is radically different, however, in highly urbanized environments, where architecture develops predominantly in terms of height, and the rooftop surfaces commonly used for the installation of Si-PV modules become increasingly insufficient to collect all the energy required for building operations [8].

Buildings are a strategic focus in the scope of a sustainable, carbon-free economy. In the European Union, around 40% of the energy consumption and 36% of CO_2 emissions are of attributed to this sector, making them "the single largest energy consumer in Europe" [9]. To boost the energetic performance of buildings, the EU has even established legislative framework, including the Energy Performance of Buildings Directive [10], with guidelines on all new-to-be-built buildings to be nearly zero-energy (NZEB) as of 31 December 2020, meaning the total annual energetic demand of each building needs to be equal to the amount of renewable energy created on site or nearby. Hence, the achievement of global energy and climate goals is linked to efforts to renovate and rethink how new to-be-built buildings are powered. To that end, the search for innovative PV systems that can be integrated into existing and newly constructed buildings, building-integrated PV (BIPV), without altering their aesthetic appearance or affecting the quality of life of their occupants, is of growing relevance.

Originally proposed in the 70s [11, 12], luminescent solar concentrators (LSCs) were developed to overcome the discrepancy between the full solar spectrum on Earth and the absorbance of the semiconductor in the PV cell [13]. The first prototypes proposed were planar devices, where sunlight penetrates an optical waveguide (usually plastic or glass) doped with luminescent centres (luminophores) that absorb the solar radiation, which is later re-emitted at a specific wavelength. As a result of the higher refractive index of the LSC surface compared to that of the surrounding air, the emitted radiation is guided in the LSC by total internal reflection towards the PV cells coupled at its edges, where it is converted into electricity. Considering that, in principle, the sunlight-exposed area of a LSC is much larger than the waveguide edges, LSCs can increase the flux of radiation incident onto the PV cells attached to the devices, boosting the produced photocurrent [14]. This ability to concentrate sunlight onto small areas allows these devices to reduce the size and related costs of the PV cells, as well as presenting very interesting alternatives for PV urban integration, Figure 1.2.
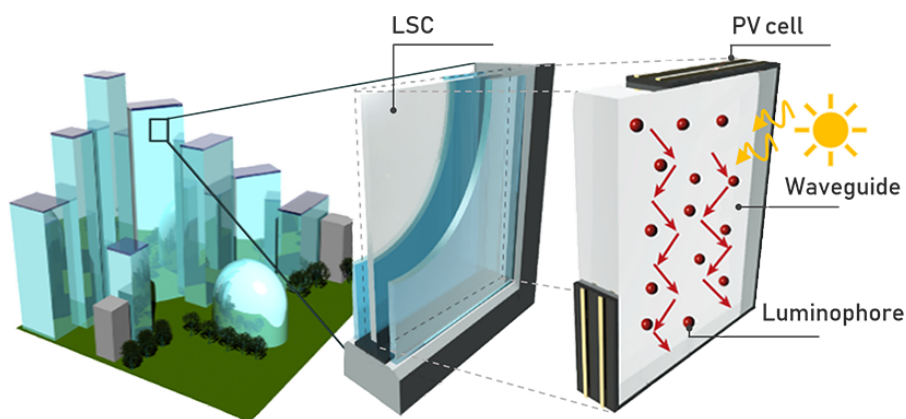
Figure 1.2: Luminescent solar concentrators for building-integrated photovoltaics. (a) Schematic representation of a PV window embedding a luminescent solar concentrator (LSC) replacing the inner glass panel. Adapted from [7, 8].

Previous studies found that LSC operation has analogous performance under direct or diffuse light incidence [15–17], which makes LSCs essentially unaffected by the efficiency losses caused by shadowing of the device that occur in PVs [7] and allows the use of the PV panels under

cloudy conditions, both significant advantages in the scope of BIPV. Moreover, when compared to standard concentrators based on passive optical elements such as lenses and mirrors, this technology presents several advantages, such as low weight, high theoretical concentration factors and no need for suntracking or cooling apparatuses [18]. These devices can be produced with tailored shape, colour, flexibility [13, 19–22], and transparency, with several semi-transparent or transparent devices reported in the literature [8, 23–25] , which gives the technology high design freedom. LCS could be embedded in facades, windows, walls, as well as rooftops, effectively converting the urban buildings into distributed energy generation units. Figures 1.3(a), 1.3(b) and (c) show examples of existing buildings with coloured facades, where this technology could be seamlessly implemented.

In the past decade, research has pushed forward the performance of LSCs, making them closer to commercial deployability [26]. In fact, LSC based on low-hazard quantum dots for PV windows are already available on the market [27]. Examples of real-world applicability of these devices are presented in Figures 1.3(d), 1.3(e) and 1.3(f). LSCs are also candidates to contribute to mobile energy, as they may be integrated in wearable fabrics and outdoor furniture [21]. Furthermore, as target delivered power values up to 10 W may be feasible with the actual figures of merit for LSCs, one additional application could be as charges to low-voltage devices (e.g. mobile phones, sensors, and wi-fi routers). The previously mentioned examples demonstrate that the transition of LSC-based solar energy harvesting units from laboratory prototypes to real-life applications has already started, having the potential to be continued in the following years.
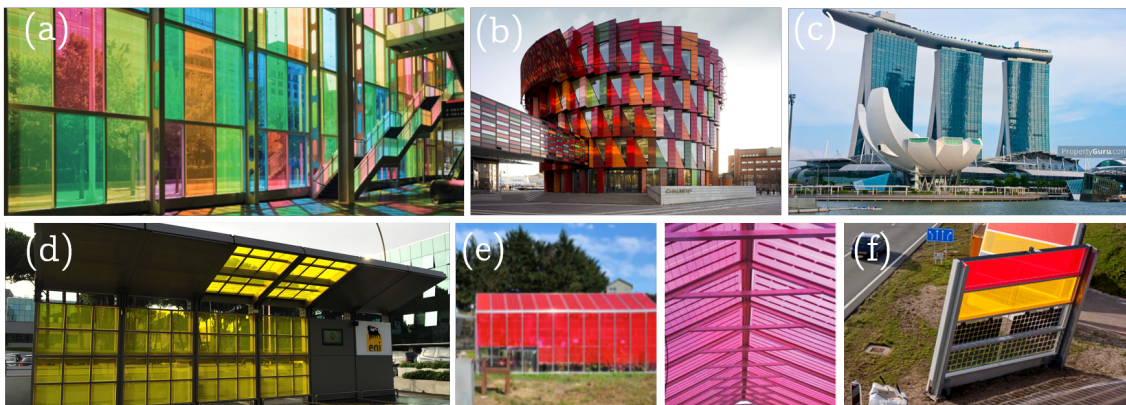
Figure 1.3: Architectural integration of LSCs into public spaces. Photos of colourful buildings around the world, (a) the Palais des Congrès in Montreal, Canada [28], (b) The Kuggen in Gothenburg [29], and (c) Marina Bay Sands building in Singapore [30]; and of real-life architectural integration of LSCs as (d) a bus stop installed in Rome, at the Eni's headquarters [31], (e) greenhouse coverage [32] and (f) sound barriers, installed alongside a highway in the Netherlands [33]).

1.1   Thesis Outline

The main objectives of this thesis are the fabrication and characterisation of LSCs using natural-based molecules as luminescent centres and organic-inorganic hybrids as host matrices. Chlorophyll was previously studied [21], showcasing promising results for LSC applications. The work developed in this thesis with the chlorophyll-based samples was therefore aimed at completing the previous work, further studying its optical properties and recombination dynamics in more detail, namely through spectrally-resolved streak camera measurements. The second part of this thesis was focused on enhanced green fluorescent protein (eGFP), by reason of its high photostability and high quantum yield [34] (roughly two times higher than that of chlorophyll a).

This thesis is divided in 7 chapters, as follows. In Chapter 1, the context of the thesis is described, as well as the main motivations and objectives of the developed work. Chapter 2 deals with the background and theory behind LSCs, starting by laying down the major concepts regarding luminescence spectroscopy and reviewing the working principle and performance quantification of

these devices. Chapter 3 describes the synthesis of the organic-inorganic hybrids and the natural-based dyes, chlorophyll and eGFP, as well as the experimental details of the optical characterisation performed on the samples. The latter is detailed in Chapter 4, through UV-Visible-NIR absorption, steady state photoluminescence and fluorescent lifetime analysis studies. In chapter 5, an introduction to Monte Carlo ray-tracing algorithms is outlined, as well as an overview of the *pv-trace* program used to perform the computational simulations. The LSC performance simulations executed throughout this thesis are also detailed in this chapter. The fabrication and characterisation of two planar LCS prototypes is described in chapter 6, where the followed experimental procedure is also detailed. Finally, in chapter 7 the general conclusions and future perspectives are discussed.

1.2 Framework

LSCs attracted a wide interest in the first years due to the possibility of replacing the expensive Si-based PV large panels. The decrease of the cost of this technology, together with the drop in oil prices in the early 1980s and the young knowledge of fluorescent systems froze the development of these devices, but the opposite trend of the energetic market in the last years and the growing of environmental concerns resulted in a rediscovering of this application, leading to a burst of LSC-related publications in the last few years [18, 35].

Several optically active centres were tested [14, 18, 35, 36], as well as the substrate or matrix in which the luminescent centres are integrated or deposited on, emphasizing the potential of organic-inorganic hybrid materials for this type of application [23, 26, 37]. The geometry of the LSC has also been the focus of some attention, as it determines the light concentration ability of the device [13, 38–41].

Luminophores

An effective luminophore must abide by several requirements, of which (1) broad spectral absorption, (2) high absorption efficiency over the whole absorption spectrum ($> 10^3$ M^{-1} cm^{-1}); (3) large Stokes shift (negligible overlap between the absorption and emission spectra); (4) high luminescent efficiency (absolute emission quantum yield > 0.5); (5) emission matching the emitted photons to the spectral response of the PV cell ($\sim$1.14 eV for silicon); and (6) solubility in the host matrix material are the main examples. Luminophores considered for LSC applications include quantum dots, rare earth ions, organic dyes and, more recently, metal halide clusters [42].

Quantum dots (QDs) are attractive candidates to serve as luminophores in LSCs due to the possibility of engineering their photophysical properties, through a careful selection of the device's materials and architecture. Recent efforts have focused on the use of bandgap and Stokes-shift engineering, providing a solution to reabsorption losses [35]. One drawback on the role of QDs as luminophores in LSC is the toxicity of the metals used (e.g., Cd, Pb), although new classes of QDs based on more friendly materials like silicon [7] have been reported.

Complexes of Lanthanide ions, Ln^{3+}, embedded in polymers or organic-inorganic hybrids are investigated as luminophores for usage in LSCs primarily because of their promise of high photostability and their large ligand-induced Stokes shift [22], high quantum yield, broad absorption spectrum, and well-defined narrow emission spectrum. Ln^{3+} attracted the attention of the scientific community from the very early days of LSC development – Neodymium was introduced, together with Rhodamine 6G, in the original LSC research of Levitt and Weber [11].

Organic dyes are π-conjugated organic molecules that offer many attractive features for LSCs including high absorption coefficients, high emission quantum yields and good photostability. The main limitations of the these molecules in LSCs applications are their small Stokes-shifts, which result in reabsorption losses, aggregation-induced quenching of the photoluminescence and narrow absorption windows [23]. Organic dyes are widely used as luminescent centres in LSC. In fact, the synthetic dye known commercially as Lumogen Red 305 is the most studied luminophore in LSCs due to its high photoluminescence quantum yield, $\sim$97% in poly(methylmethacrylate), PMMA [43].

The potential replacement of synthetic organic dyes by luminescent organic molecules extracted from renewable and natural materials could make LSCs cheaper and sustainable, while maintaining the inherent features such as synthetic versatility and high absorption coefficients/emission

quantum yields [13]. Notwithstanding the attractive properties of nature-based dye molecules for LSCs, the latter have been poorly explored [21]. When considering a sustainable route for designing this devices, two luminescent organic molecules, chlorophyll and fluorescent proteins, have recently been reported. The first has a key role in photosynthesis, being responsible for sunlight harvesting [44], with emission properties in the red/NIR spectral region. Frias *et al.* [21], processed chlorophyll-based planar LSCs, with chlorophyll molecules incorporated into amine-functionalized organic–inorganic hybrids. When coupled to a Si-based PV device, the chlorophyll-based LSCs revealed an optical conversion efficiency (η_{opt}, defined as the ration between the output power at the LSC edges, P_{out}, and the incident optical power, P_{in}) and power conversion efficiency (PCE, defined as the ratio between the PV device output electrical power, P_{out}^{el} and the incident optical power, P_{in}) values around 3.70% and 0.10%, respectively. Fluorescent proteins are characterised by their advantageous photoluminescence features including high quantum yield, narrow emission and photostability [34]. Green fluorescent protein (GFP), for example, has been widely employed as a fluorescent marker [45]. Recently, due to the rising interest in waste-free technologies and their eco-friendly nature and mass production capability, GFP has been applied in different areas (e.g. in lasers and light-emitting diodes [46, 47]). Furthermore, fluorescent proteins can be produced in genetically encoded organisms [48] and is edible and digestible in the mammalian stomach [49]. In a novel work, Sadeghi *et al.* [50] reports for the first time the use of a fluorescent protein, mScarlet, in a LSC prototype, which when coupled to Si PV cells yielded an η_{opt} of 2.58%. Both the previously detailed nature-inspired LSCs demonstrated a huge potential of for sustainable PV energy conversion, with η_{opt} values comparable with the state-of-the-art LSC efficiency levels.

Host matrices

The choice of the host material for the luminophores also has a strong effect on LSC efficiency [26, 51], since it has direct impact on (1) the processes of photon harvesting, as reflection and scattering events are matrix-dependent; (2) absorption/emission, since the emission quantum yield of the luminophore can be affected by its solubility in the host material; and (3) waveguiding/collection at the LSC perimeter, given that total internal reflection and parasitic absorption (absorption process which do not generate an electron/hole pair) in the host matrix are determined by its optical properties.

Host materials for LSC applications ought to be designed so as to provide a number of desirable features [52], including: suitable refractive index (> 1.5, allowing maximum trapping efficiency with minimized surface losses [23]); high transmittance in the visible and near-infrared range and high solubility for the embedded luminescent species. In addition, cheap and easy processability and high stability (namely thermo-oxidative stability or long-term durability in outdoor contexts for target applications) are also necessary. The waveguide choice has received significantly less attention than the luminophores, with cheap polymers such as PMMA or polycarbonate traditionally employed as inexpensive host materials in bulk LSCs or as easily processable thin-film LSCs [14]. The usage of PMMA as a host matrix is limited by the poor luminophore solubility, as well as by its limited photostability, especially under high energy UV radiation [23, 26]. Improving the stability of host polymeric matrices for LSCs has been a key focus for many research groups in the last few years [53–56]. Research of environmentally-friendly, biodegradable polymeric host matrices to potentially reduce the carbon footprint of LSCs, when compared to conventional oil-based systems, was also conducted, evidencing bio-based polymers as valuable renewable matrices for high-performance LSCs [57–60].

The stability question raised by organic polymer waveguides has led to the investigation of organic-inorganic hybrids. While pure glass waveguides have a high refractive index, their weight and fragility limits their useful application in building integrated photovoltaics. In contrast, organic-inorganic hybrids offer the best of both worlds, as they combine useful proprieties of both the organic and inorganic components of their structure – the flexibility and malleability of the former and the mechanic and thermal stability, when compared with purely organic polymeric materials, of the latter [61–66]. Despite the limited number of reports to date of hybrid materials in LSCs, their efficiency values are already comparable to those of pure organic LSCs [23]. The huge variety of organic precursors available introduces the possibility of tuning the hybrid's functional and mechanical properties, with the possibility of tuning the refractive index [67].

In the field of glassy hybrids, the use of luminescent bridged-silsesquioxane thin films doped with trivalent lanthanide ions for LSCs were introduced [68, 69]. More recently, the same groups reported a Eu^{3+}-doped silsesquioxane system based on an ethane tetracarboxamide-based organosilane [70], demonstrating the high versatility of these systems for the production of defect- and crack-free films with controlled nanostructure via the sol-gel chemistry. Another important class of sol-gel-based hybrid materials widely investigated as host matrices for LSCs is that of ureasil systems. Di- and tri-ureasil organic-inorganic hybrids are suitable for the development of sustainable technologies due to their environmentally friendly characteristics: the synthesis is performed at room temperature, the materials can be recycled [71] and allow the incorporation of organic optical active centres. Efforts on the use of tri- and di-ureasil compounds as host matrices in LSCs with different doping species in planar [21, 43, 72–74] and cylindrical [41, 75] LSCs have been reported.

Finally, liquid LSC dispersed in water have also been proposed. Advantages of this architecture include the sustainability of this approach (without waste nor significant negative impact toward the environment), that can be easily integrated with further steps of downstream processing by using, for example, conventional liquid-liquiq extraction or the alternative aqueous biphasic systems, which can be easily scaled-up to continuous flow [13].

1.3 Objectives and contributions

The work presented in this thesis was developed in two main institutions, University of Aveiro (UA) and International Iberian Nanotechnology Laboratory (INL), with the aim of studying and producing cost-effective LSCs with planar architectures based on natural based luminescent centres, in the scope of sustainable energy solutions with applications in BIPV.

Within this framework, two natural based dyes were optically characterised and studied, being later incorporated into organic-inorganic hybrids of the ureasil family, that exhibit suitable features to act as host matrices for eco-friendly and cost-effective LSCs. The photoluminescent properties of the doped hybrids were investigated preliminary. Monte Carlo ray-tracing simulations were performed resorting to the open source program *pvtrace*. Afterwards, two different prototypes of LSCs were developed – a planar LSCs based on a glass container filled with eGFP dispersed in an aqueous solution and a planar LSC with eGFP incorporated into a di-ureasil amine-functionalised organic–inorganic hybrid. The main contributions of this thesis can be summarized as follows:

i Synthesis and processing (thin films and monoliths) of di- and tri-ureasils incorporating chlorophyll and eGFP;

ii Monte Carlo simulations of two different planar LSC;

iii Optical characterisation of the materials by UV-Visible-NIR absorption spectroscopy, photoluminescent emission and excitation spectroscopy, absolute emission quantum yields and fluorescent lifetime analysis;

iv Time-resolved photoluminescent spectroscopy resorting to a streak camera setup;

v Production of two different planar LSC prototypes;

vi Performance quantification of the LSC, through optical conversion efficiency, external quantum efficiency and concentration factor calculations.

2. Background

The aim of this chapter is to understand the main physical phenomena occurring in a luminescent solar concentrator. The LSC performance relies on the possibility of fully exploiting the luminescent properties of the emitting centres and of light guidance through a transparent medium.

As such, a brief overview of molecular luminescent spectroscopy is conducted. Special attention is paid to absorption of UV-visible radiation and the different ways of de-excitation of an excited state, with emphasis on the time-scales relevant to the photophysical processes (neglecting molecular interactions in the excited state). Then, pertinent parameters that quantify the optical features of LSCs (extinction coefficient, emission quantum yield, brightness) are defined.

The working principles and performance quantification of LSCs are also reviewed, in the absence or presence of PV cells, addressing relevant concepts as the optical conversion efficiency and external quantum efficiency.

2.1   Luminescence spectroscopy

Luminescence is a general term that refers to radiation emission from an electronically excited state through any nonthermal process in the UV, visible or infrared spectral regions. Fluorescence and phosphorescence are particular cases of luminescence, depending upon the electronic configuration of the excited state and the emission pathway [66, 76].

When incident radiation is of lower energy than the energy gap between two electronic states, the photons are not absorbed and the molecule is said to be transparent to that radiation energy. For sufficiently higher photon energies, absorption may occur and the electrons in the lower energy state are promoted to the higher excited state. Afterwards, the deactivation process back to the ground-state can happen through a combination of radiative and non-radiative processes. These two phenomena are described in the following subsections.

2.1.1   Absorption of UV–Visible-NIR radiation

Molecular orbitals are assumed to be some combination of the atomic orbitals of the atoms involved. There are several types of molecular orbitals, categorised by molecular-orbital symmetry labels. For example, a σ orbital can be formed either from two s atomic orbitals, or from one s and one p atomic orbitals, or from two p atomic orbitals having a collinear axis of symmetry [76]. A π orbital is formed from two p atomic orbitals overlapping laterally. The combination between orbitals of neighbouring atoms can be bonding, antibonding (indicated by the superscript *), or non-bonding (n), depending upon whether the overlap integral is positive, negative or zero, respectively. The excitation of an organic molecule occurs when a photon of appropriate energy promotes an electron from a molecular bonding orbital (σ, π) to an anti-bonding orbital (σ^*, π^*). The energy of these transitions corresponds to the difference between the energy of the levels involved. The most relevant transitions in organic molecules are $n \rightarrow \pi*$ and $\pi \rightarrow \pi^*$ ($\sigma \rightarrow \pi^*$ and $\sigma \rightarrow \sigma*$ transitions are usually too energetic) [77]. The lowest energetic transition corresponds to that between the highest occupied molecular orbital (HOMO) and the lowest unoccupied molecular orbital (LUMO) in the ground state of the molecule.

When one of the two electrons of opposite spin in a ground state molecular orbital is promoted to a molecular orbital of higher energy, its spin is in principle unchanged so that the total spin quantum number ($S = \sum_i s_i$, $s_i = \pm 1/2$) remains equal to zero. As the multiplicities, $(2S + 1)$, of both the ground and excited states are equal to 1, both are called singlet states (usually denoted S_0 for the ground state, and S_1, S_2, ... , S_m for the 1st, 2nd and mth excited state). In contrast, a molecule in a singlet excited state may undergo conversion into a state where the promoted electron is no longer paired with the one in the ground state – has changed its spin. Since there are then two electrons with parallel spins, $S = 1$ and the multiplicity is 3. Such a state is called a triplet

state. According to Hund's Rule, for a given electronic configuration, the term with maximum multiplicity has the lowest energy. Therefore, the triplet state has a lower energy than that of the singlet state of the same configuration.

Absorption mainly occurs from the vibronic ground states of molecules, since, at room temperature, thermal energy is not sufficient to significantly populate the excited vibrational states. There are two important selection rules for absorption transitions [76], postulating

1. **spin-forbidden transitions**, which means that transitions between states of different multiplicities are not allowed and therefore $\Delta S = 0$; and

2. **symmetry-forbidden transitions** for centrosymmetric molecules, that is, transitions between electronic wavefunctions corresponding to two states with the same parity.

Nonetheless, weak interactions between wavefunctions of different multiplicities via spin–orbit coupling can happen, which breaks down the first selection rule and allows these transitions to some extent. Moreover, symmetry-forbidden transitions can nevertheless be observed due to molecular vibrations that can break perfect symmetry (vibronic coupling). For large molecules, the symmetry of the overall system can be associated with that of specific point groups using group theory but the discussion of this is beyond the scope of this thesis.

Finally, the extent to which radiation of a given wavelength, λ, is absorbed by a substance, absorbance $A(\lambda)$, is given by the Beer-Lambert law,

$$A(\lambda) = -\log \frac{I(\lambda)}{I_0(\lambda)} = \epsilon(\lambda)Cl, \tag{2.1}$$

where I_0 and I are the incident and transmitted intensities of the radiation with wavelength λ, $\epsilon(\lambda)$ represents the molar extinction coefficient, C is the concentration of absorbing molecules, and l is the optical path length.

2.1.2 Radiative and non-radiative transitions between electronic states

A representation of the main processes involved upon the absorption of energy of an electron in the ground state molecular orbital and subsequent deactivation pathways of the formed excited states is usually illustrated by a Jablonski diagram, Figure 2.1.

In these diagrams, the electronic states are arranged vertically by energy and grouped horizontally in terms of their multiplicity. The singlet ground, first, and second electronic states are depicted by S_0, S_1, and S_2, respectively. At each of these electronic energy levels the electron can exist in a number of vibrational energy levels, depicted by 0, 1, 2, etc. The vertical arrows correspond to absorption from the 0 (lowest) vibrational energy level of S_0 since this is the most populated level at room temperature. Absorption of a photon can bring an electron to one of the vibrational levels of S_1, S_2, ..., etc. It is important to note that absorption is faster (10^{-15} s) with respect to all other processes, so an approximation that the electronic transition occurs within a stationary nuclear framework (Franck–Condon principle) is made [76].

Molecules can dissipate their excitation energy upon radiation of a photon (radiative processes). Photon emission from excited singlet states to the vibrational states of other singlet states is called fluorescence, occurring in a time range of 10^{-9} to 10^{-7} s [66, 78]. Generally, fluorescence emission occurs from S_1 to the vibrational states of the ground singlet S_0. Emission of a photon from the triplet excited T_1 vibrational sates of S_0 is denominated phosphorescence. This process is much slower than fluorescence ($10^{-3} - 10^2$ s), as it involves two states of distinct multiplicity (formally forbidden transitions).

The non-radiative processes through which the electron can relax to the ground state are (i) internal conversion, (ii) intersystem crossing and (iii) delayed fluorescence. In the first, an electron close to a ground state vibrational energy level relaxes to the ground state via transitions between vibrational energy levels, giving off the excess energy to other molecules as heat (vibrational energy). The time scale of the internal conversation and vibrational relaxation processes is between 10^{-14} to 10^{-11} s. Intersystem crossing, possible due to spin–orbit coupling, is the process where an electron transition from an upper singlet excited state to a lower energy level triplet state.
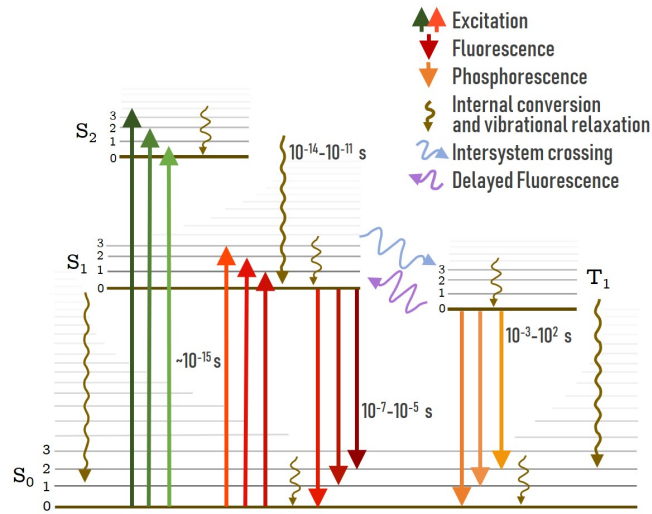
Figure 2.1: Jablonski diagram summarizing the typical radiative and nonradiative transitions within a electronically excited molecule. The typical time scales of the processes involved are indicated. Adapted from refs. [66, 76]

Finally, delayed fluorescence is the process where the electron, after a fast intersystem crossing to the triplet state, is thermally popped back into the singlet state.

Due to the non-radiative transitions, fluorescence and phosphorescence will occur at lower energy (longer wavelengths) than that of the absorbed photons. The energetic difference between the maximum of the emission and absorption spectra ascribed to the same electronic transition is known as Stokes shift.

2.1.3   Fluorescence parameters

Three parameters generally used to quantify fluorescence are the extinction coefficient (ϵ), fluorescence quantum yield (Φ), and brightness (B).

The extinction coefficient, related to the absorbance of a material by the Beer-Lambert law (Eq. 2.1), is an indicator of the impedance a given substance offers to the passage of electromagnetic radiation. The fluorescence quantum yield compares the efficiency of fluorescence emission relative to all other pathways of relaxation and is expressed as the dimensionless ratio of the number of photons emitted to the total number of photons absorbed by a material. In other words, once a photon has been absorbed, the photon's probability of being emitted through fluorescence is related to the quantum yield. However, since this parameter only translates the percentage of photons emitted by a material in relation with the ones absorbed, when comparing different materials, higher Φ does not immediately translate to the strongest emission intensity.

To better quantify the brightness of the fluorescence,

$$B = \Phi \times \epsilon, \tag{2.2}$$

the quantum yield needs to be weighted by the material's ability to absorb radiation to enter the excited state ϵ.

2.2   Luminescent solar concentrators

2.2.1   Principles of operation

Luminescent solar concentrators are devices designed to convert and concentrate sunlight for use in photovoltaics, usually made of glass or plastic substrates, acting as waveguides, containing

luminescent species (e.g. organic dyes, inorganic phosphors, quantum dots) generally embedded in the host matrix or part of a coating layer, Figure 2.2.
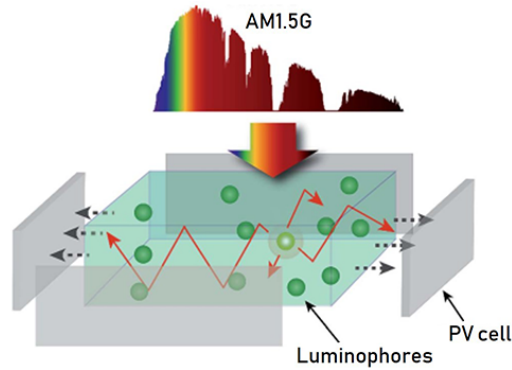

Figure 2.2: Schematic representation of the working principle of a LSC. Adapted from ref. [21].

Incident radiation is absorbed by the electrons, which are excited to a higher energy level. The absorbed photons are then re-emitted via radiative decay upon relaxation to the ground state, with lower energy than the one absorbed due to non-radiative losses in the material. A fraction of the downshifted radiation is confined within the host matrix as a result of the difference in refractive indexes between the LSC material and the surrounding medium and total internal reflection guides the photons within the waveguide modes to the narrow edges of the concentrator, where they are collected by small-area solar cells for photon-to-electron conversion through photovoltaic effect.

The amount of confined radiation is given by

$$\eta_{\text{trap}} = \left(1 - \frac{1}{n_p^2}\right)^{1/2}, \tag{2.3}$$

where n_p is the refractive index of the medium. For example, for a typical $n_p = 1.5$ nearly 80% of incident radiation is trapped inside the LSC.

2.2.2   Loss mechanisms

Several loss mechanisms may be present in LSCs, which reduce the amount of radiation reaching the PV cells and the overall efficiency of the device [14]. For this thesis, the proposed ureasil-based LSCs are in a planar architecture and therefore this type of device configuration will be considered as a reference when discussing loss mechanisms. The main loss mechanism in planar LSCs (p-LSC) are represented in Figure 2.3.
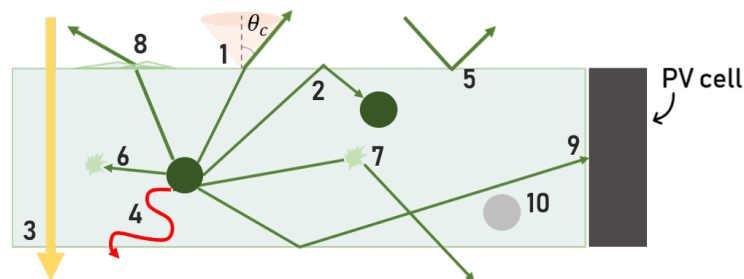
Figure 2.3: Schematic representation of the main loss mechanisms in a LSC, where 1) represents light emitted outside capture cone; 2) re-absorption of emitted light by another luminophore; 3) input light is not absorbed by the luminophore; 4) internal quantum efficiency of the luminophore is not unity; 5) reflection from the waveguide surface; 6) absorption of emitted light by the waveguide; 7) internal waveguide scattering; 8) surface scattering; 9) solar cell losses and 10) luminophore degradation. Adapted from ref. [14].

The portion of the emitted light that is trapped inside the waveguide is determined by the refractive index of the host material, Eq. 2.3. According to Snell's law, total internal reflection dictates that the emitted light is only trapped inside the waveguide if the angle of incidence is greater than the critical angle θ_c,

$$\theta_c = \sin^{-1}\left(\frac{1}{n_p}\right). \tag{2.4}$$

If the incident angle is smaller than θ_c, the light leaves the material through the escape cone and is lost. Therefore, one loss associated with LSC is the light emitted by the luminophore under an angle which is refracted out of the waveguide through the escape cone, rather than being reflected internally, Figure 2.3 (1).

Most LSCs also suffer major losses through reabsorption of the emitted photons by other luminescent centres as a result of the overlap between their emission and absorption bands, i.e., small Stokes shift values (2). Luminescent molecules have also limited spectral absorption bands, which leads to incomplete incident light absorption (3). In addition, if the optically active centre has a non-unity quantum yield, the absorbed photon may instead be lost as heat and consequently emission does not occur (4). A small part of the input light is lost through reflections from the surface of the waveguide, due to Fresnel reflections (5). The emitted light may also be scattered or absorbed by the waveguide material, (6) and (7), and lost and some surface scattering may occur (8).

The PV cell at the waveguide edge has a non-uniform spectral response, with a fraction of incident photons being lost due to the finite conversion efficiency of the PV cell (9). Additionally, high energy UV photons, when absorbed, can either provoke direct photodegradation of the molecules, or degradation of other molecular species within the vicinity of the luminescent centres, that subsequently react with them, diminishing the total emission of the LSC (10).

2.2.3 Performance quantification

The LSC performance quantification is an important issue to be addressed. The main parameters adopted and used in this thesis for the performance quantification of the fabricated LSCs, using theoretical expressions and expressions using electrical parameters measured in the coupled PV device, is detailed below.

The efficiency of a LCS is directly related with the ratio of photons collected at the edges of the LSC in relation to the number of incident solar photons, quantified through the optical conversion efficiency [13, 21, 41, 73, 79, 80],

$$\eta_{\mathrm{opt}} = \frac{P_{\mathrm{out}}}{P_{\mathrm{in}}}, \tag{2.5}$$

where P_{out} is the output power at the LSC edges and P_{in} the incident optical power.

The η_{opt} can be approximated through an expression, first proposed by Reisfeld *et al.* in 1982 [81], that weights all the losses in the LSC described in the previous subsection,

$$\eta_{\mathrm{opt}} = (1 - R) \cdot \eta_{\mathrm{abs}} \cdot \eta_{\mathrm{SA}} \cdot \eta_{\mathrm{yield}} \cdot \eta_{\mathrm{Stokes}} \cdot \eta_{\mathrm{trap}} \cdot \eta_{\mathrm{mat}}. \tag{2.6}$$

In this expression,

- 1-R is the portion of incident power that is transmitted into the LSC. $R = (\frac{n_1 - n_2}{n_1 + n_2})^2$ is the Fresnel reflection coefficient for perpendicular incidence, where n_1 and n_2 represent the refractive index of the optically active layer and the surrounding medium at the incident wavelength, respectively.

- $\eta_{\mathrm{abs}} = 1 - 10^{-A}$ is the ratio of photons absorbed by the emitting layer to the number of photons falling on it, in which A represents the absorbance value at the incident wavelength (Eq. 2.1);

- η_{SA} is the self-absorption efficiency, arising from possible reabsorption by the luminescent centres;

- η_{yield} is the emission quantum yield of the optically active centre at the emission wavelength

- $\eta_{\text{Stokes}} = \dfrac{\lambda_p}{\lambda_i}$ is the Stokes efficiency calculated by the energetic ratio between the average energy of the emitted photons (the emission peak position, λ_p, in energy units) and the incident energy;

- η_{trap} is the trapping efficiency, Eq. 2.3;

- η_{mat} takes into account the transport losses due to the waveguide matrix absorption and scattering.

When characterising an LSC with PV cells attached, η_{opt} is quantified by the definition given in ref. [82],

$$\eta_{\text{opt}} = \frac{P_{\text{out}}}{P_{\text{in}}} = \frac{I_{\text{SC}}^{\text{L}} V_0^{\text{L}}}{I_{\text{SC}} V_0} \frac{A_{\text{e}}}{A_{\text{s}}} \frac{\eta_{\text{solar}}}{\eta_{\text{PV}}}, \tag{2.7}$$

which is often used and will be adopted in this thesis. I_{SC}^{L} and V_0^{L} correspond to the short-circuit current and the open-circuit voltage when the PV device is coupled to the LSC, while I_{SC} and V_0 are the correspondent current and voltage of the PV device when exposed directly to solar radiation. A_{s} and A_{e} represent the exposed and total edge area, η_{solar} is the efficiency of the PV device relatively to the total solar spectrum and η_{PV} is the efficiency of the PV device at the LSC emission wavelengths.

The overall performance of a LSC is further quantified by the concentration factor (F) that is a product of the geometrical gain factor (G) and the optical conversion efficiency (η_{opt}),

$$F = G \times \eta_{\text{opt}}, \tag{2.8}$$

where $G = \frac{A_s}{A_e}$. A_s is the exposed area of the PV to illumination, while A_e is the total edge area.

An LSC with a high concentration factor allows for a substantial reduction in solar cell size. The higher the photon concentration of an LSC, the more cost-effective the LSC will be in theory.

The performance of a LSC when coupled to a PV cell may also be quantified in terms of external quantum efficiency, EQE [13, 21, 41, 73, 83, 84],

$$\text{EQE}\,(\lambda) = \frac{\#\ electrons}{\#\ photons} = \frac{I_{SC}\ E_v}{P_{\text{in}}\ e} = \frac{I_{SC}\ hc}{P_{\text{in}}\ e\lambda}, \tag{2.9}$$

e being the charge of the electron, h Planck's constant, c the speed of light and λ the wavelength. EQE measurement is an indicator of how well the LSC device coupled to the PV cell converts incident photons of a specific wavelength to electricity, quantifying the ratio between the number of charge carriers collected by the device, $\frac{I_{\text{SC}}}{e}$, to the number of incident photons of a given wavelength, $P_{\text{in}}/\frac{hc}{\lambda}$.

Moreover, in order to quantify the LSC's ability to absorb the sunlight available for PV conversion, the overlap integral between its absorption spectra and the solar irradiation on Earth can be calculated,

$$O = \int_{\lambda_1}^{\lambda_2} N_{\text{AM1.5G}}(\lambda) \times \left(1 - 10^{-A(\lambda)}\right) d\lambda, \tag{2.10}$$

where λ_1 and λ_2 are the limits of the spectral overlap between the LSC's absorption spectrum and the AM1.5G spectrum, $N_{\text{AM1.5G}}$ is the photon flux of AM1.5G and A is the absorbance of the LSC.

3. Materials and methods

Chlorophyll and eGFP were selected featuring applications as optical active centres for sustainable LSCs due to their light harvesting ability and high absolute emission quantum yield in the visible/NIR spectral ranges. To enable the easy and controlled processing of planar LSCs, chlorophyll and eGFP were incorporated into amine-functionalized organic-inorganic hybrids with the added advantages of avoiding non-luminescent dye-clusters or dye-aggregates [73] formation, and potentially enhancing their absolute emission quantum yield and photostability [85].

A brief overview of the organic molecules used as natural-based dyes and the hybrid hosts materials is given in this chapter, followed by the sample preparation description (chlorophyll and eGFP in solution and hybrid samples) and the processing of the chlorophyll- and eGFP-doped organic-inorganic hybrids as monoliths and thin films. Lastly, the experimental techniques and devices used in the optical characterisation of the chlorophyll and eGFP samples and hybrid compounds are detailed.

3.1 Chlorophyll, eGFP and ureasil hybrid compounds

Chlorophylls serve an important role in the process of photosynthesis and several different types of chlorophylls exist naturally [86]. These molecules consist of a chlorin ring, whose four nitrogen atoms surround a central magnesium atom, with several attached side chains and a hydrocarbon tail. The different side chains characterize each type of chlorophyll molecule, the only difference between the variations of interest in the scope of this thesis, chlorophyll a and chlorophyll b, being an aldehyde (CHO) group in the latter, instead of a methyl (CH_3) group [87], in the position marked with the letter R in Figure 3.1(a).

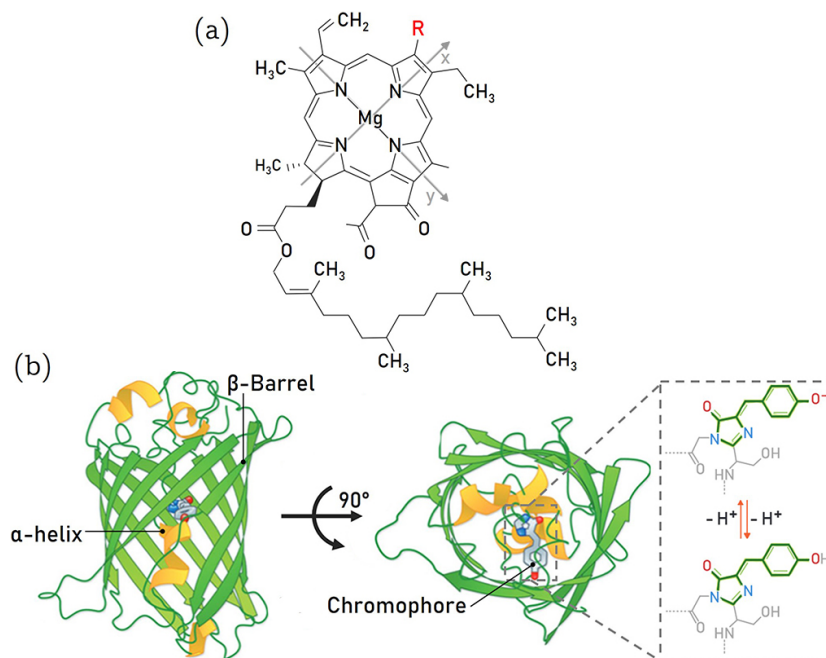Figure 3.1: Molecular structure of the natural dyes. (a) Schematic representation of chlorophyll a, R=CH_3 and chlorophyll b, R=CHO. The diagonal arrows indicate the directions of the two polarization axes, x and y, of chlorophyll molecules; (b) Ribbon representation of eGFP, with a top view to better visualize the chromophore's position and highlight its deprotonated and protonated forms. Adapted from [88].

Genetic manipulation of the amino acid residues implied in the chromophore formation creates green fluorescent protein mutants with improved photostability and modified spectral properties, of which eGFP, with F64L and S65T mutations [89], is an example. The crystal structure of eGFP, Figure 3.1(b), displays the traditional β-barrel structure of GFP with an alpha helix containing the covalently bonded chromophore running through the core of the protein. The phenol and imidazolinone rings in the chromophore form a conjugated system of π-electrons responsible for the excitation and emission in GFP-like proteins [90]. Moreover, the chromophore can exist in two different stable and interconvertible forms [91] – a deprotonated and a protonated form, Figure 3.1(c) – with different fluorescence behaviour.

The materials used as host matrices were di-ureasil, d-U(600), and tri-ureasil, t-U(440), t-U(3000) and t-U(5000), organic-inorganic hybrids, whose non-hydrolysed precursor's molecular structure can be seen in Figure 3.2. These matrices consist of a siliceous inorganic skeleton grafted, through urea crosslinkages, to both ends of poly(ethylene oxide) chains. The U is related to the urea group and d and t to the di and tri prefixes, that indicate the number of covalent bonds between the polymer chain and the siliceous skeleton – di specifies that both ends of the polymer chain are covalently bonded to the siliceous-based domains, while tri stipulates a branched tripodal structure. Finally, 600, 440, 3000, and 5000 correspond to the average molecular weight of the oligopolyoxyethylene chains, also being an indirect indicator of their length.
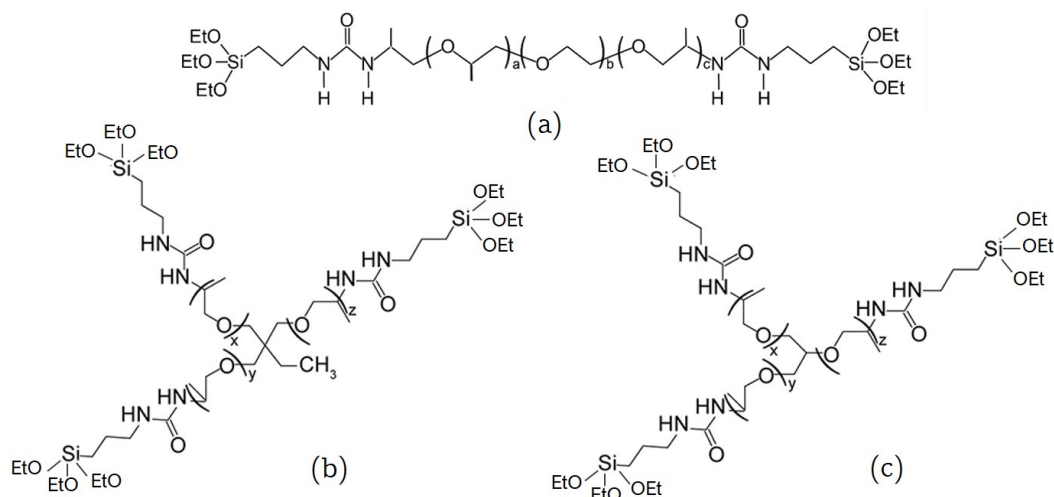

Figure 3.2: Molecular structure of the non-hydrolysed organic-inorganic precursors. Schematic representation of (a) d-UPTES(600), $a + c = 2.5$ and $b = 8.5$; (b) t-UPTES(440), $x + y + z = 5$-6; and (c) t-UPTES(3000), if $x + y + z = 50$, or t-UPTES(5000), if $x + y + z = 85$.

3.2 Sample preparation

3.2.1 Natural-based dyes: chlorophyll and enhanced green fluorescent protein

The extraction and purification of chlorophyll a were performed in collaboration with Dr Edison Pecoraro and Professor Sidney Ribeiro from the Institute of Chemistry of São Paulo State University (UNESP), Brazil. Chlorophyll was obtained from *Spirulina maxima* via solvent extraction and purified by column chromatography [21], yielding dark green chlorophyll crystals with 95% purity (predominantly chlorophyll a, with traces of chlorophyll b and other pigments) and a molar mass of 893.51 g mol^{-1}. Two solutions with different concentrations of chlorophyll were prepared, termed chl-17 and chl-18, Table 3.1. A mass of 0.0045 g of the extracted chlorophyll was dissolved in 2 mL of ethanol (99.8%), resulting in a concentration of 3×10^{18} molecules/cm^3. From this solution, an amount of 0.2×10^{-3} L was dissolved in 1.8×10^{-3} L of ethanol to prepare

a solution with 3×10^{17} molecules/cm^3. Afterwards, the two solutions were kept under magnetic stirring for 15 minutes at room temperature.

Enhanced green fluorescent protein (eGFP) extraction from *Escherichia coli* (E. *coli*) BL21 cells was performed in collaboration with Professor Sónia Ventura and Professor João Coutinho from CICECO - Aveiro Institute of Materials and the Chemistry Department of University of Aveiro, following the procedure reported in references [92, 93]. Three distinct eGFP aqueous solutions were prepared at different eGFP concentration, 8×10^{15}, 2×10^{16} and 3×10^{16} molecules/cm^3, labelled GFP-15, GFP-A2 and GFP-A1 respectively.

Figures 3.3(a) and 3.3(b) show photographs of the chl-17 and chl-18 solutions under white light and UV radiation (365 nm), respectively, while Figures 3.3(c) and 3.3(d) show photographs of the three eGFP solutions under the same conditions.
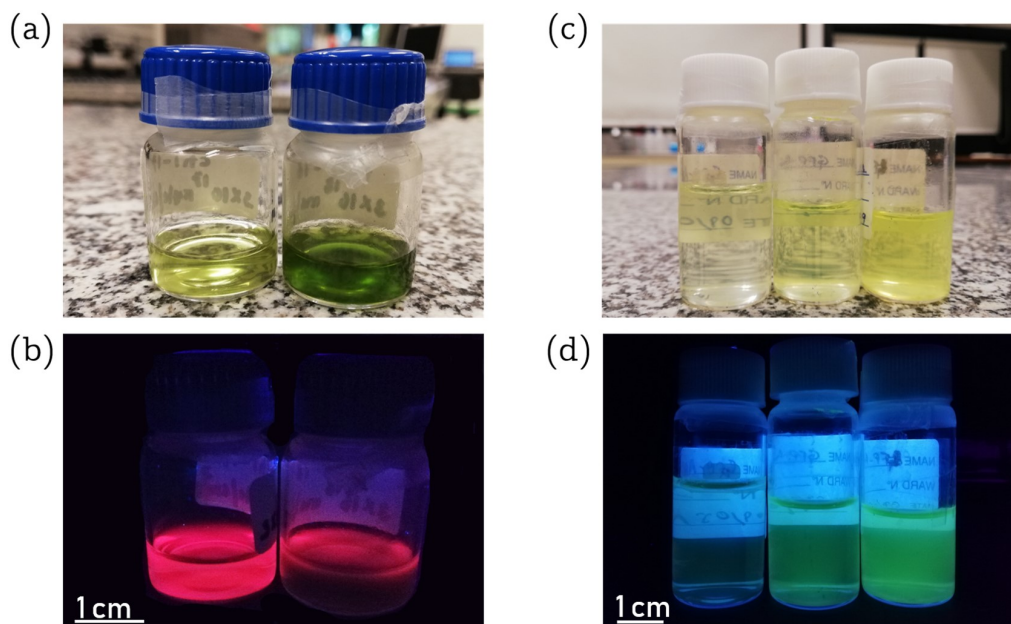

Figure 3.3: Photographs of the chlorophyll and eGFP solutions under (a)(b) white light and (c)(d) UV radiation (365 nm), presented, from left to right, from the lowest to the highest concentration – chl-17 (left) and chl-18 (right) in (a)(b) and GFP-15 (left), GFP-16(A2) and GFP-16(A1) (right) in (b)(d). The samples are labelled in Table 3.1.

Table 3.1 summarises the organic molecule-based solutions used as natural-based dyes in the organic-inorganic complexes, as well as each attributed label.

Table 3.1: List, designation and concentration of the chlorophyll- and eGFP-based solutions.

Label	Molecule	Solvent	Concentration (molecules/cm^3)
chl-17	chlorophyll	ethanol	3×10^{17}
chl-18			3×10^{18}
GFP-15	eGFP	water	8×10^{15}
GFP-16(A2)			2×10^{16}
GFP-16(A1)			3×10^{16}

3.2.2   Chlorophyll- and eGFP-doped organic-inorganic hybrids

The incorporation of the natural dyes was performed by sol-gel method in collaboration with Dr. Lianshe Fu, Principal Researcher at CICECO - Aveiro Institute of Materials and at the Physics

Department of the University of Aveiro. The sol-gel method is characterised by low temperature ($< 100°C$) processing and shaping, sample homogeneity and high-purity, and availability of the precursors. This technique is based on the formation of a colloidal suspension (sol), later submitted to a gelation process that forms a three-dimensional network (gel) [94, 95]. The synthesis of organic-inorganic hybrids by the sol-gel process is advantageous, as it allows the mixing organic and inorganic components at molecular scale in mild synthesis conditions, with accessible, low-cost precursors. Additionally, organic-inorganic hybrids can be processed either as a transparent monolith (with adaptable shape) or as a transparent, uniform thin-film with controlled thickness.

The processing of the organic-inorganic hybrid thin films and monoliths was carried out with the assistance of Dr Sandra Correia, Researcher at CICECO - Aveiro Institute of Materials and at the Physics Department of the University of Aveiro. Jeffamine® ED-60, Jeffamine® T-3000, Jeffamine® T-5000 and Jeffamine® T-403, purchased from Huntsman Company, ethanol (EtOH, 99.8%, Fluka Riedel-de Haën and Fisher Scientific), 3-isocyanatopropyl triethoxysilane (ICPTES, 95%, Aldrich), tetrahydrofuran (THF, 99.9%, Sigma-Aldrich) and hydrochloric acid (HCl, 37%, Sigma-Aldrich) were used as received for all synthesis detailed in this thesis. Chlorophyll was incorporated into the di-ureasil, d-U(600), and tri-ureasil, t-U(440), t-U(3000) and t-U(5000), organic-inorganic hybrid monoliths and thin films, while the eGFP was only incorporated into a d-U(600) host matrix.

Chlorophyll hybrid systems

The urea cross-linked non-hydrolysed precursors for the chlorophyll-doped samples were synthesised following the procedure described in [21]. The four precursors were synthesised by reacting Jeffamine® ED-600, T-3000, T-5000 and T-403 with ICPTES (1:2 molar ratio for ED-600 and 1:3 for T-3000, T-5000 and T-403), in THF (2:1 v/v THF/Jeffamine®), at 82°C under reflux and magnetic stirring for 18 hours. The solvent THF was evaporated under rotary evaporation, yielding the d-UPTES(600), t-UPTES(3000), t-UPTES(5000) and t-UPTES(440) hybrid precursors, Figure 3.2.

Following the synthesis of the di-uresil and tri-uresil organic-inorganic precursor suspension, four chl-17 solutions were prepared (following the previously mentioned procedure) and each was added to 3 g of the viscous suspension of a different precursor. After, the four suspensions were kept under magnetic stirring at room temperature for 30 minutes. The as-prepared suspensions were then submitted to a sol-gel transition, adding 4×10^{-4} L of HCl (1.2 M) as a catalyst. A few drops of the suspensions were deposited on glass substrates (NORMAX, $7.6 \times 2.6 \times 0.1$ cm^3) by a one-step spin-coating process (SPIN 150-NPP, APT) at 500 rpm for 30 seconds, under ambient conditions. The resulting thin films (2 for each hybrid precursor, 8 in total) were also heat-treated at 45°C to remove residual solvents. The remaining volumes were cast into plastic cuvettes ($1.0 \times 1.0 \times 4.0$ cm^3), and heat-treated at 45°C, yielding greenish- transparent monoliths. The monoliths and thin films containing d-U(600) and t-U(3000), hereafter referred to as dU600-chl and tU3000-chl, were kept under heat treatment for 5 days. The hybrid materials with t-U(5000) and t-U(440) as precursors, henceforth referred to as tU5000-chl and tU440-chl, were kept under heat treatment for 10 days.

Di-ureasil hybrid doped with eGFP

For the eGFP-based organic-inorganic hybrid, 1×10^{-3} L (1.67 mmol) of Jeffamine® ED-600 and 0.5×10^{-3} L of THF were mixed and stirred at room temperature. Then 0.90×10^{-3} L (3.42 mmol) of ICPTES was added dropwise under stirring with 1:2 molar ratio of ED-600:ICPTES. The sol was stirred for further 2 hours at room temperature, evaporating the THF and resulting in the non-hydrolyzed hybrid precursor d-UPTES(600). After, 0.5×10^{-3} L of the GFP-16(A1) solution was added to the d-UPTES(600) precursor. The resulting mixture was stirred at room temperature for 15 minutes and cast into a plastic holder. The gelation process occurred at room temperature within two days, resulting in a transparent monolith hereafter referred to as dU(600)-GFP.

Table 3.2 summarises the different organic-inorganic complexes synthesised and detailed in this subsection, as well as each attributed label.

Table 3.2: List and designation of the organic-inorganic hybrids doped with chlorophyll and eGFP. The processing method for each hybrid, thin film (F) and/or monolith (M), and the number (#) of samples is also detailed.

Label	Natural based-dye	Hybrid host	Processing	# of samples
dU(600)-chl		d-U(600)	M & F	1/2
tU(440)-chl		t-U(440)	M & F	1/2
tU(5000)-chl	chlorophyll	t-U(3000)	M & F	1/2
tU(3000)-chl		t-U(5000)	M & F	1/2
dU(600)-GFP	eGFP	d-U(600)	M	1

3.3 Experimental

The optical characterisation of the previously detailed samples was performed through multiple experimental techniques, namely UV/visible/NIR spectroscopy, steady-state photoluminescence and photoluminescence excitation spectroscopy, absolute emission quantum yield measurements and fluorescence lifetime analysis. The latter was investigated through time-correlated single photon counting (TCSPC) and streak camera studies.

The research infrastructures used for the experiments described in the optical characterisation of the different samples were the following:

i at University of Aveiro

- UV-Visible-NIR absorption spectrometer (Lambda 950 dual-beam, Perkin-Elmer).

- Steady-state fluorescence spectrofluorimeter (Fluorolog3®, Horiba Scientific) equipped with a TRIAX 320 monochromator (1200 g/mm) and coupled to a photomultiplier (R928, Hamamatsu). Excitation and emission slit bandpass of $0.3-1.5$ nm and $0.3-1$ nm, respectively. Low-temperature measurements were carried out resorting to a helium closed-cycle cryostat (APD Cryogenics-HC2) equipped with a vacuum system (5×10^{-9} bar) and a temperature controller.

- A C9920-02 system (Hamamatsu), coupled to a monochromator for wavelength discrimination, an integrating sphere as the sample chamber and a multichannel analyser for signal detection, was used for absolute emission quantum yields measurements. The method is accurate to within 10%.

- TCSPC-based fluorescence lifetime spectrofluorimeter (Horiba Scientific) coupled to a TBX-04 photomultiplier tube module (950 V) and a 200×10^{-9} s time-to-amplitude converter with a delay of 70×10^{-9} s. The excitation source was a pulsed diode (NanoLED-390, Horiba/Jobin-Yvon, peak at 388 nm, 1.2×10^{-9} s pulse duration, 1 MHz repetition rate, and 150×10^{-9} s synchronization delay).

ii at INL - International Iberian Nanotechnology Laboratory:

- Steady-state fluorescence spectrofluorimeter (FluoroMax-4® Horiba Scientific), equipped with a monochromator (1200 g/mm) and coupled to a photomultiplier (R928P Hamamatsu). The excitation source was a 150 W xenon arc lamp. The measurements were performed with 1 nm and 5 nm excitation and emission slit bandpass.

- Streak imaging system (C90001, Hamamatsu), equipped with synchroscan unit, composed of a slow sweep unit (M10913), a Czerny–Turner spectrograph (Acton SP2300, Princeton Instruments, gratings with 50g/mm and 150g/mm), a $\sim$ 80 ps pulsed diode laser (M10306-27, Hamamatsu), with central wavelength of 379 nm, a $\sim$ 69 ps pulsed diode (PLP10, Hamamatsu) with central wavelength of 467 nm, a delay unit (C1097-05, Hamamatsu) and a 2D charged-coupled-device (CCD) camera (Orca-R2, Hamamatsu), controlled by the HPA-TA software (Hamamatsu).

Streak camera experimental setup

Figure 3.4(a) shows a schematic representation of the streak camera setup. The two excitation sources operate in 20 MHz pulse repetition rate and a in a 90° excitation-detection setup configuration. Two lenses are placed after the sample, where the sample's emission is collected and collimated (first lens), and focussed onto the entrance slit of the spectrograph (second lens). 390 nm and 472 nm long-pass filters were used according to the excitation source and placed after the second lens. Time resolution is obtained via a synced streak-camera mounted at the exit port of the spectrograph. Combined spectral and time resolved data is recorded by a 2D charged-coupled-device detector mounted at the output port of the coupled spectrometer-streak-camera unit. The device control and acquisition software control the detection unit (streak camera with delay unit, CCD camera, and spectrograph).
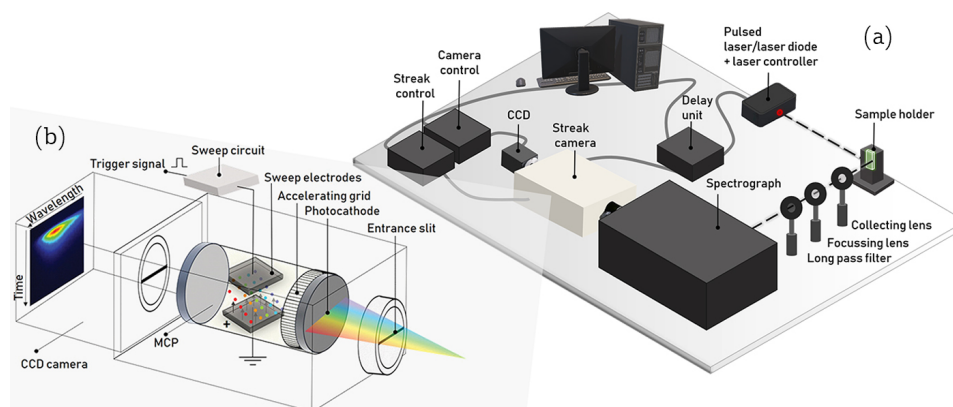

Figure 3.4: Streak camera systems for simultaneous spectral and time-resolved fluorescent studies. Schematic representation of the (a) experimental setup used for the streak camera measurements and (b) principle of operation of the streak camera.

Streak camera operating principle

Figure 3.4(b) illustrates the operation principle of a streak camera. First, the light pulse to be measured is horizontally dispersed by the spectrograph, separating the different wavelengths. Then, the pulse passes through the entrance slit of the streak camera and is formed by the device optics into a slit image on the photocathode of the streak tube, where the incident photons are converted to electrons via the photoelectric effect. Leaving the photocathode, the electrons are accelerated longitudinally within the streak camera by an accelerating grid, pass through a pair of deflection plates and are multiplied in a micro-channel plate (MCP), being then bombarded against the CCD camera, where they are converted again into light. As the electrons pass through the deflection plates, high voltage is applied to the electrodes at a timing synchronized to the incident light, initiating a high-speed sweep from top to bottom. During this sweep, the electrons, which arrive at slightly different times, are deflected in slightly different angles in the vertical direction, and enter the micro-channel plate (MCP). On the CCD camera, the phosphor image corresponding to the optical pulse which was the earliest to arrive is placed in the uppermost position, with the other images being arranged in sequential order from top to bottom. Consequently, the vertical direction on the screen serves as the time axis. The position in the horizontal direction of the phosphor image corresponds to the horizontal location of the incident light, defined by its wavelength. Also, the brightness of the various phosphor images is proportional to the intensity of the respective incident optical pulses.

Experimental setups with a streak camera coupled to a spectrograph can therefore be used to measure at the same time both fluorescence emission spectra and fluorescence decay curves. The first are generated by summarizing the intensities along the vertical (time) axis and plotting the resulting intensities versus the horizontal (wavelength) axis, while the latter are extracted by summing up the fluorescence intensities in the wavelength bands of interest and then plotting the resulting intensities versus the time axis.

4.   Optical characterisation

In this chapter, the optical features of chlorophyll and eGFP, either in solution or incorporated into organic-inorganic hybrids, are discussed through the experimental results acquired from UV-Vis-NIR absorption spectroscopy, steady-state photoluminescence and photoluminescence excitation spectroscopy, absolute emission quantum yield measurements and fluorescence lifetime analysis (TCSPC and streak camera studies). First, the optical characterization for the chlorophyll-based compounds is described, followed by the description of the experimental studies performed on the eGFP compounds.

4.1   Spectral analysis of Chl compounds

4.1.1   UV-Visible-NIR absorption spectroscopy

The linear absorption spectrum of chlorophyll a arises from $\pi \rightarrow \pi^*$ electronic transitions that derive from electron promotions involving the two HOMOs and two LUMOs in terms of the four-orbital model applied by Gouterman [96]. This model, although very simple, reproduces all the major features of this system. The electrons within the delocalized π-system have the ability to jump up from the lowest occupied molecular orbital (ground state), S_0, to two higher unoccupied molecular electron orbitals (excited states), S_1 and S_2, referred to as Q and Soret bands, respectively, as shown in Figure 4.1. The energy gap between the S_0 and S_1 states is bridged by photons in the red spectral region (600–700 nm), whereas the energy gap between the S_0 and S_2 states is higher and for this reason requires a more energetic blue photon (400–500 nm) to be crossed [97–101]. To be noted that electronic transitions of chlorophylls are reported to occur along the x-axis and the y-axis of the molecule (see Figure 3.1(a)). As such, the two absorption bands are split into two, with one band of each pair polarized along the y-axis (S_y, S_y) and the x-axis (S_x, Q_x), the latter occurring at slightly smaller wavelengths [102]. Upon excitation, the electron in the S_2 state undergoes internal conversion to the first singlet excited state S_1. Excitation of the molecule with a red photon can lead to the promotion of an electron to the S_1 state directly. The electrons in the S_1 state can return to the ground state by emission of the energy as a photon of light (fluorescence) or through internal conversion as heat.

As shown in Figure 4.2(a), the absorption spectra of the chl-18 and chl-17 solutions reveal two main components at 415 nm and 665 nm, assigned to the monomer form of chlorophyll a [21, 99, 103], and two shoulders around 465 nm and 648 nm, due to the contribution of chlorophyll b monomers, resulting from the $S_0 \rightarrow S_2$ and $S_0 \rightarrow S_1$ transitions of chlorophyll excited states.
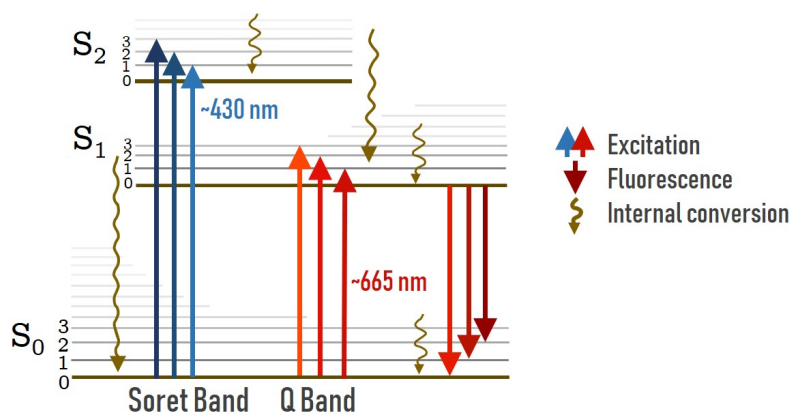

Figure 4.1: Jablonski diagram summarizing the two electronic transitions of chlorophyll a.

However, the larger relative intensity of chlorophyll a, when compared with that of chlorophyll b, indicates a higher concentration of chlorophyll a species. To better discern the chlorophyll a and chlorophyll b contributions in the absorbance spectrum of the chl-17 and chl-18 ethanolic solutions, the latter were overlapped with those reported in ref. [99] for diluted ethanolic solutions containing only chlorophyll a and chlorophyll b molecules.

In Figure 4.2(b), the dU(600)-chl-F, tU(440)-chl-F, tU(3000)-chl-F and tU(3000)-chl-F thin films show major changes in their absorption spectra in comparison with those of the chlorophyll solutions. Due to the low number of optical active centres, the absorbance of chlorophyll a is too low to be detected. Nonetheless, magnifying (×180) the region of interest of the chlorophyll excited states (inset of Figure 4.2(b)), one can detect a peak at 380 nm characteristic of chlorophyll a absorption. The absorbance around 480 nm is most likely due to the presence of carotenoids as contaminants [21]. The absorption bands in the UV (260-350 nM) are ascribed to the hybrid host matrices [104]. Figure 4.2(b) displays the spectra of four thin films, as no relevant differences between the two films processed for each hybrid host was found.
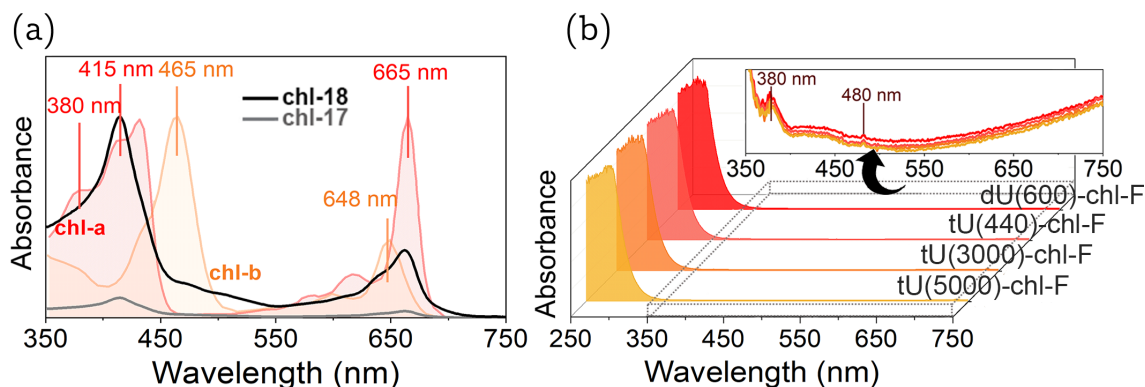

Figure 4.2: Comparison between the absorption spectra of the chlorophyll ethanolic solutions with those of the chlorophyll-doped hybrid thin films. Absorption spectra of (a) the chl-18 and chl-17 solutions, overlaid with the spectra of chlorophyll a and chlorophyll b from ref. [99]; and (b) the dU(600)-chl-F, tU(440)-chl-F, tU(3000)-chl-F and tU(5000)-chl-F hybrid thin films. The inset shows a magnification (×180) of the overlapped spectra in the 350-750 nm region.

4.1.2 Steady-state photoluminescence

The emission of the chl-17 and chl-18 solutions, shown respectively in Figure 4.3(a) and Figures 4.3(b), exhibit the characteristic emission peaks of chlorophyll a and of chlorophyll b [21, 105, 106]. The main peak at 675 nm and the lower intensity peak at ∼720 nm are ascribed to the monomeric and dimeric forms of chlorophyll a, respectively. The emission peak around 650 nm, characteristic of chlorophyll b, is also detected for both solutions.

As mentioned, excitation in the UV-blue region (Soret band) leads to $S_0 \rightarrow S_2$ transitions. However, no radiative emission in the blue region is recorded in the de-excitation process that follows, as excitation in the Soret band is quickly followed by internal (non-radiative) conversion into the S_1 excited state [101, 107, 108]. When comparing the absorption (see Figure 4.2(a)) and emission of chlorophyll a (peak at 675 nm) of the chl-17 and chl-18 solutions, the Stokes-shift is around 158 cm^{-1} (7 nm) and 421 cm^{-1} (19 nm), respectively. The chlorophyll b and dimeric chlorophyll a emission peaks display higher intensity in comparison with the monomeric chlorophyll a emission peak for the latter solution, due to its higher concentration.

Given that the chlorophyll extraction from *Spirulina maxima* resulted in a powder of chlorophyll a with 95% purity, the presence of chlorophyll b and other pigments in the solution was expected. In fact, excitation with long-wavelength UV radiation results in emission in the blue-green spectral region (shoulder centred at 450 nm) as well, as we can see in the black and grey coloured spectra in Figures 4.3(a) and 4.3(b). A total of four characteristic fluorescence bands can be differentiated in plants [109]: the blue fluorescence near 450 nm, the green fluorescence ∼520 nm, the red fluorescence ∼690 nm and the far-red fluorescence band ∼730 nm. Blue-green fluorescence in
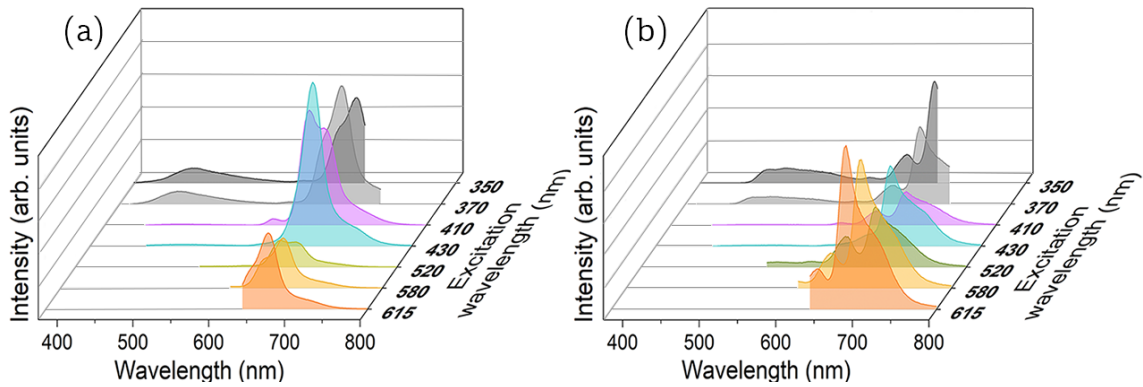
Figure 4.3: Room temperature emission spectra of chlorophyll based solutions with different concentrations: (a) chl-17 and (b) chl-18.

plants is due to a mixed signal emitted by various plant phenolics, such as hydroxycinnamic acids bound to the cell walls. These compounds are also present in *Spirulina maxima* [110] and explain the shoulder centred at 450 nm seen when exciting the solutions at 350 nm and 370 nm.

The room temperature emission spectra of the hybrids samples dU(600)-chl, tU(3000)-chl, tU(5000)-chl and tU(440)-chl, shown in Figures 4.4(a), 4.4(b),4.4(c) and 4.4(d), are dominated by a blue-green emission, attributed to electron–hole recombination of the urea groups and within oxygen defects in the siliceous skeleton of the hybrid hosts [104, 111, 112], and chlorophyll *a* fluorescence in the red spectral region. The emission spectra of the four hybrid hosts are formed of a large broad band (350-600 nm), with peak position red-shifting as the excitation wavelength increases. This behaviour was previously observed for the ureasil organic-inorganic hybrids, being related disordered-related processes generally associated with transitions occurring within localized
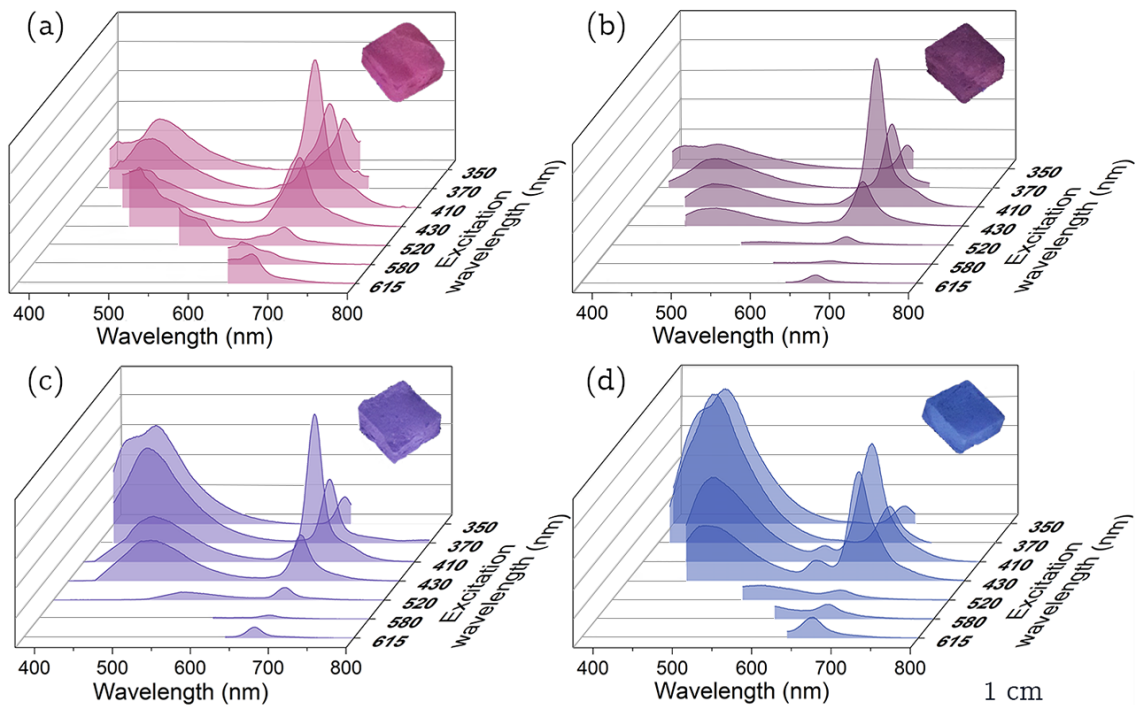

Figure 4.4: Room temperature emission spectra of the four chlorophyll-doped organic-inorganic hybrid samples: (a) dU(600)-chl, (b) tU(3000)-chl, (c) tU(5000)-chl and (d) tU(440)-chl. The inset photographs refer to the monolith samples under UV radiation (365 nm). The scale refers to the monoliths' dimensions.

states in non-crystalline structures [113, 114].

Focusing on the chlorophyll *a* characteristic emission, the main component at 675 nm and the shoulder at ∼720 nm, ascribed to its monomeric and dimeric contributions [21]. The peak attributed to chlorophyll *b* emission (650 nm) is also observed. Another emission peak around 605 nm is detected when exciting at 410 and 430 nm, most noticeable in the tU(440)-chl emission (Figure 4.4(d)). This peak is also present in the emission spectra of the chl-17 solution (4.3(a)) with the same excitation wavelengths. The emission spectra of tU440-chl and tU5000-chl have a higher relative intensity of the hybrid host emission, in relation that of chlorophyll. On the contrary, dU600-chl has the lowest relative intensity of the hybrid host emission. This suggest that the latter has a more efficient energy-transfer process between the host and the chlorophyll molecules of all four organic-inorganic hybrids.

The chlorophyll-based organic-inorganic hybrids monoliths were also exposed to UV radiation and photographed, as shown in the insets of Figures 4.4. The dU600-chl emission is clearly visible to the naked eye, in the red spectral region. tU440-chl exhibits a blue hue, consequence of the blue coloured visible light also present in the spectrum of the UV lamp. tU3000-chl and tU5000-chl acquire a purplish colour, a combination of both the blue light emitted by the lamp and the red emission of the sample itself. Nonetheless, tU30000-chl has a redder hue so the chlorophyll relative emission is expected to be higher for this sample than in the case of tU5000-chl. This is in agreement with the photoluminescence emission spectra recorded when exciting each sample at a similar excitation wavelength (370 nm), where dU(600)-chl has the higher chlorophyll relative emission, followed by tU(3000)-chl.

The ethanolic solutions of chlorophyll and the chlorophyll-doped hybrids were further studied by photoluminescence excitation spectroscopy. The room temperature excitation spectra of the chl-17 solution, shown in Figure 4.5(a), reveal the main bands in the blue and red region of the visible spectrum related to chlorophyll *a* excited states (see Figure 4.2(a)). The same behaviour was found for the chl-18 solution (not shown). The four chlorophyll-doped organic-inorganic hybrids were monitored within the chlorophyll maximum emission peak at 675 nm (red line) and within the hybrid emission band at 470 nm (blue line), Figures 4.5(b)-(e).

In resemblance to what was reported for the chl-17 solution, all hybrids when monitored at 675 nm reveal the characteristic excitation bands of chlorophyll *a*, notwithstanding a slight blue-shift (∼ 15 nm), when compared to the chlorophyll extract in solution excitation. This behaviour was
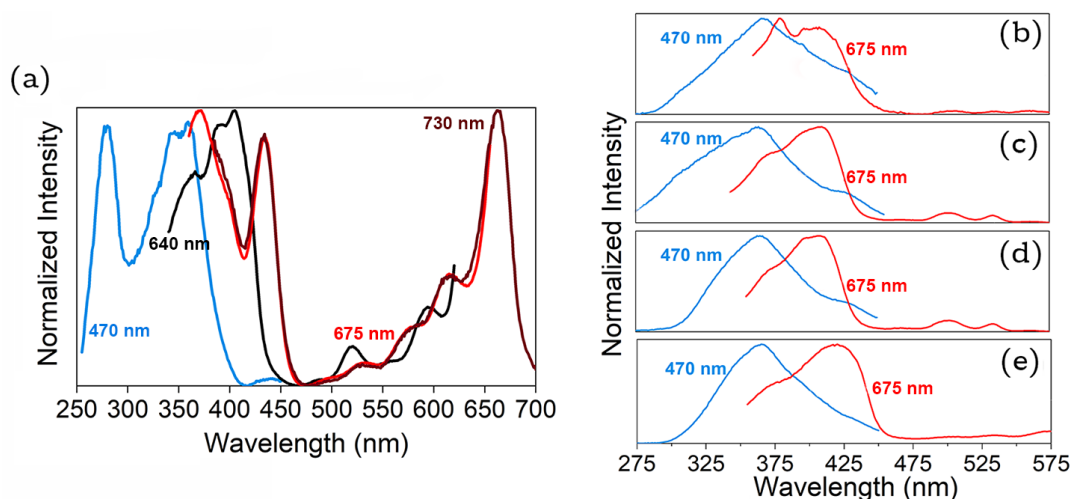

Figure 4.5: Comparison between the room temperature excitation spectra of the chlorophyll ethanolic solution with those of the doped organic-inorganic hybrids. Excitation spectra of the (a) chl-17 solution, monitored at 470 nm, 640 nm, 675 and 730 nm; and of the (b) dU(600)-chl, (c) tU(3000)-chl, (d) tU(5000)-chl and (e) tU(440)-chl chlorophyll-doped hybrid samples, monitored at 675 nm and 470 nm. Both the solution and the organic-inorganic hybrids reveal the main bands ascribed to chlorophyll *a* excited states. All hybrids reveal the characteristic excitation bands of chlorophyll *a* and the hybrid excited states, that overlap in the UV (250–400 nm).

previously reported in ref. [21] and ascribed to the electrostatic interaction between the hybrid hosts and the chlorophyll molecules through ATR/FT-IR spectroscopy studies. Moreover, when the excitation spectrum is monitored within the hybrid emission band, the hybrid excited states appear as expected for all four samples, showing excitation maxima peaking at 362 nm for dU600-chl, at ∼368 nm for tU3000-chl and at 365 nm for both tU5000-chl and tU440-chl. Finally, it is relevant to point out that the excitation spectrum monitored within the host emission broad band overlaps with that monitored within the chlorophyll a band in the UV spectral region, in good agreement with the hypothesis of energy transfer between the hybrid excited states and the chlorophyll molecules.

The emission properties of the samples were further studied through the measurement of the absolute emission quantum yield, Φ, as a function of the excitation wavelength (360–580 nm). Observing Table 4.1, the quantum yield is higher when the excitation wavelength is resonant with the Soret absorption band of chlorophyll a (370, 410 and 430 nm) and maximum (0.15 ± 0.02) for the dU600–chl and tU(440)-chl samples. These results suggest that lower polymer molecular weight favours the optical properties of chlorophyll. A detailed analysis of this behaviour, however, is beyond the scope of this thesis.

Table 4.1: Absolute emission quantum yield (Φ) as a function of the excitation wavelength measured for the chlorophyll-doped hybrids. The relative yield error is $\frac{\Delta\Phi}{\Phi} = 0.1$ (10%).

	Φ_{350nm}	Φ_{370nm}	Φ_{410nm}	Φ_{430nm}	Φ_{520nm}	Φ_{580nm}
dU(600)-chl	0.088	0.128	0.150	0.126	0.102	0.103
tU(3000)-chl	0.063	0.096	0.128	0.091	0.069	0.045
tU(5000)-chl	0.056	0.082	0.137	0.126	0.039	0.069
tU(440)-chl	0.049	0.066	0.142	0.146	0.050	0.101

4.1.3 Fluorescence lifetime analysis

Fluorescent behaviour over time was monitored for the chl-17 solution at different emission wavelengths, within regions of interest of the chl-17 solution emission spectra (see Figure 4.3(a)) - plant phenolics (470 nm), chlorophyll b (640 nm), and of chlorophyll a monomers (675 nm). The TCSP-based fluorescent emission decay curves measured for these different regions are presented in Figures 4.6(a), 4.6(b) and 4.6(c), respectively. In all cases, the experimental curves are well described by single exponential functions. The lifetime values, Table 4.2, resulting from the data best fit to a single exponential function, obtained when monitoring the chlorophyll b (640 nm) and chlorophyll a (675 nm) bands are analogous to those previously reported for chlorophyll a and b in ethanolic solutions [115]. Plant's blue-green fluorescence decay was studied previously [116] and five kinetic components were resolved, with lifetimes ranging from 20-50 ps to a very slow decay occurring between 7.3–11.1 ns, justifying the higher fluorescence lifetime found for plant phenolics (470 nm).

Table 4.2: Emission lifetime values (τ) of the chlorophyll chl-17 solution, excited at 390 nm and monitored at distinct emission wavelengths (λ_{em}).

λ_{em} **(nm)**	**470**	**640**	**675**
$(\tau \pm 0.11) \times 10^{-9}$ **s**	7.82	5.30	5.53

Time-resolved fluorescence spectra were recorded with the streak-camera setup previously described. Figure 4.7(a) shows the time-resolved fluorescence emission data of the chl-17 solution recorded with the streak camera, under excitation of the 379 nm picoseconds laser. The intensity is colour-coded from dark blue (low intensity) to red (high intensity). A grating of 50 grooves/mm was used in the spectrograph, with spectral resolution of 4.2 nm and ability to cover 280 nm in spectral range. On the bottom, Figure 4.7(b), and on the right side of the streak image, Figure
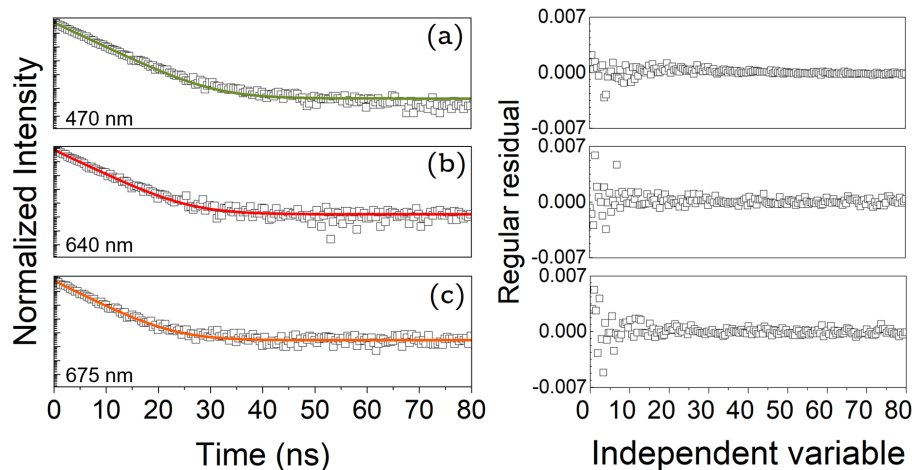
Figure 4.6: Fluorescence lifetime emission decay curves of the chl-17 solution, excited at 390 nm and monitored at (a) 470 nm, (b) 640 nm, and (c) 675 nm at room temperature. The solid lines represent the best fit to the data ($R^2 > 0.99$) and the plots are presented with a logarithmic y-axis. The respective residual plots are shown on the right, aside each decay curve.

4.7(c), are presented the fluorescence emission spectrum and decay curve, integrated over the full time and wavelength ranges of the image.

Qualitatively, one can see in the streak image the emission band between 600-760 nm characteristic of chlorophyll, with again the main peak at 665 nm and the shoulder ~720 nm attributed to chlorophyll a monomers and dimers, respectively, and the shoulder around 648 nm ascribed to chlorophyll b. Additionally, the intensity of the chlorophyll a monomers is much higher (red colour) in relation to the other two bands, in agreement with the emission spectra of Figure 4.3. Furthermore, the fluorescence emission at 665 nm is longer, ~15 ns (starting at 5 to 20 ns), than the emission at 645 and ~720 nm, that lasts around 10 ns (5 to 15 ns).

Fluorescence decays curves were integrated over the regions of interest of the chl-17 solution emission spectra (with the exception of plant phenolics, that emit outside the range of the streak image). Figure 4.8(a) shows the decay curve integrated over the region of chlorophyll b (630-650 nm), while Figure 4.8(b) displays the result of the integration over monomeric chlorophyll a
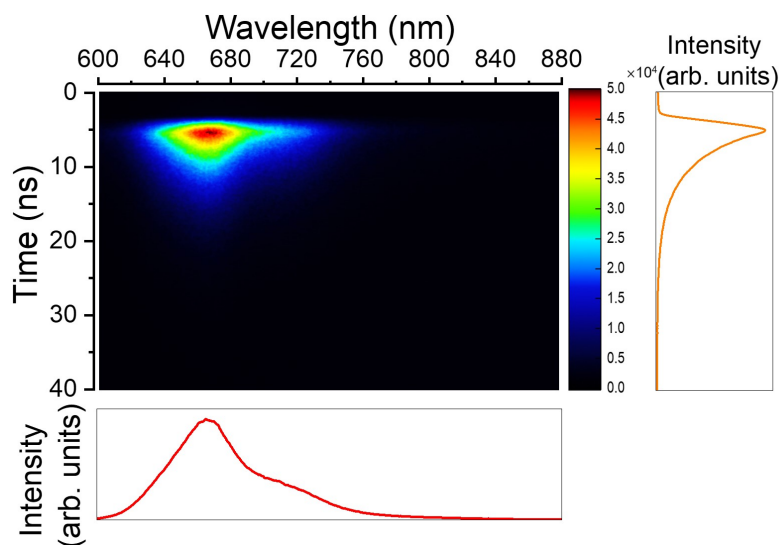

Figure 4.7: Spectrally-resolved streak-camera image of the chl-17 chlorophyll ethanolic solution. (a) Streak image with the integrated (b) emission spectra and (c) fluorescence decay curve.

emission (650-690 nm). The data were extracted from the streak image and integrated over the wavelength intervals resorting to a MATLAB® script, previously developed by Ricardo Abrão, PhD student in the Ultrafast Bio- and Nanophotonics group at INL. In both cases, the experimental curves are well described by single exponential functions and are presented in this order, alongside the regular residual of the fittings performed.
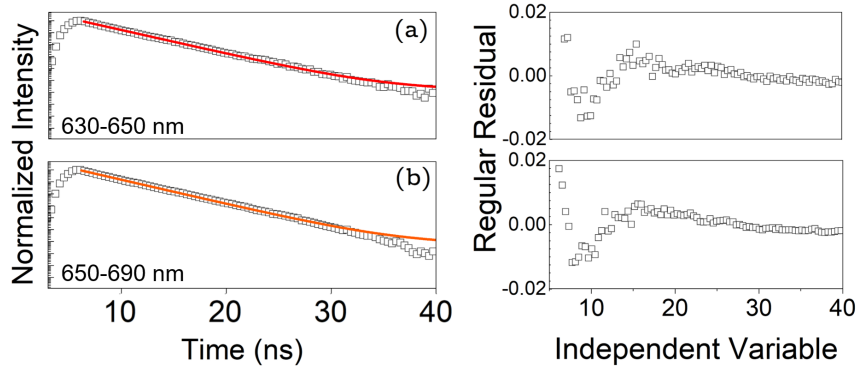

Figure 4.8: Analysis of the fluorescent decay curves on the wavelength ranges of chlorophyl b and a. Streak based fluorescence decay curves integrated over the region of (a) chlorophyll b emission and (b) monomeric chlorophyll a emission, alongside the regular residual of the fittings performed. The solid lines represent the best fit to the data ($R^2 > 0.99$) and the plots are presented with a logarithmic y-axis.

The calculated lifetimes, τ, for each wavelength range are presented in Table 4.3, with τ values obtained when monitoring the chlorophyll b and chlorophyll a emission bands analogous to those found through TCSPC (Table 4.2).

Table 4.3: Emission lifetime values (τ) of the chlorophyll chl-17 solution, extracted from the streak image of Figure 4.7(a) and excited at 379 nm. The decay curves were obtained by integration over different regions of the emission.

λ_{em} **(nm)**	**630-650**	**650-690**
$(\tau \pm 0.01) \times 10^{-9}$ s	5.03	4.92

Time-resolved photoluminescent images were recorded with the streak camera setup for the dU(600)-chl, tU(3000)-chl, tU(5000)-chl and tU(440)-chl monoliths, Figures 4.9, in the same conditions used for the chlorophyll solution. The intensity is again colour-coded from dark blue (low intensity) to red (high intensity). The emission bands of both the hybrid hosts (440-560 nm) and chlorophyll (600-720 nm) are visible in the four images. Nonetheless, the range limit, inherent of the experimental setup, didn't allow part of the hybrid emission (before 440 nm) and the tail of the chlorophyll band (above 720 nm) to be captured, even though the grid used was the one that permitted the broadest wavelength interval. The SNR is much lower for the tU(440)-chl hybrid (Figure 4.9(d)) due to the lower intensity of its emission.

In terms of hybrid-to-chlorophyll relative intensity, dU(600)-chl (Figure 4.9(a)) and tU(440)-chl have higher relative hybrid host emission, whereas tU(3000)-chl (Figure 4.9(b)) and tU(5000)-chl (Figure 4.9(c)) exhibit the contrary behaviour. tU(3000)-chl and tU(440)-chl have the highest and lowest chlorophyll relative emission of the four samples, respectively. This trend is the same as previously reported for the photoluminescent emission studies of these samples, with the exception of the dU(600)-chl hybrid sample, that previously showed the highest chlorophyll relative emission. One possible explanation for the difference between the spectrofluorimeter and streak measurements could be due to the samples used – in the latter, the sample was much smaller and more jagged. In terms of temporal duration, the chlorophyll emission lasts longer ($\sim$20 ns) than that of the hybrid hosts ($\sim$10 ns) in the four samples.

Fluorescent decay curves were integrated for each image over the wavelength range of the
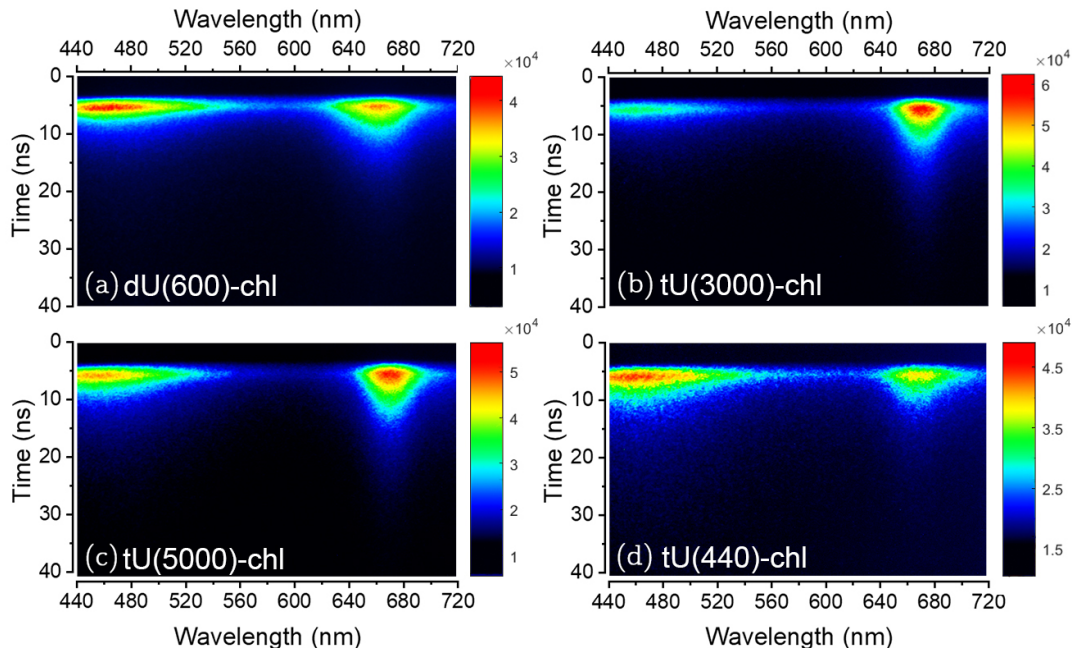
Figure 4.9: Comparison between the streak images of the different chlorophyll-doped organic-inorganic hybrids. Streak images with spectral and time-resolved fluorescence information of: (a) dU(600)-chl, (b) tU(300)-chl, (c) tU(5000)-chl and (d) tU(440)-chl.

hybrid host (440-500 nm) and chlorophyll (640-720 nm) emission. The experimental decay curves, Figure 4.10, were fitted by single exponential functions. When integrated over the chlorophyll emission band, the experimental curves are well described by single exponential functions. However, fitting the hybrid emission decay curves with single exponential function resulted in poor fits ($R^2 < 0.99$), revealing a non-exponential behaviour previously reported in the literature [74, 112, 117]. As such, an average lifetime value,

$$< \tau > = \frac{\int_{t_1}^{t_2} I(t)t \; dt}{\int_{t_1}^{t_2} I(t) \; dt} \; , \tag{4.1}$$

was calculated, where $t_1=0$ and t_2 corresponds to the time value where the luminescence intensity reaches the background.

The lifetime values, Table 4.4, obtained when monitoring the chlorophyll band are in agreement to those previously found for chlorophyll in solution (Tables 4.2 and 4.3) and for the chlorophyll-doped organic-inorganic hybrids of ref. [21]. The average lifetime values calculated for the hybrids host emission are also similar to the values previously found in the group, reported in the same reference. The average lifetimes calculated for the hybrids' emission band are lower than those previously reported for the isolated hybrids d-U(600) (~2–15×10^{-9} s) [117] and t-U(5000) ($30.2\pm0.2\times10^{-9}$ s) [112]. This decrease in the lifetime of the hybrid host excited states suggests hybrid-to-chlorophyll energy transfer [21, 118].
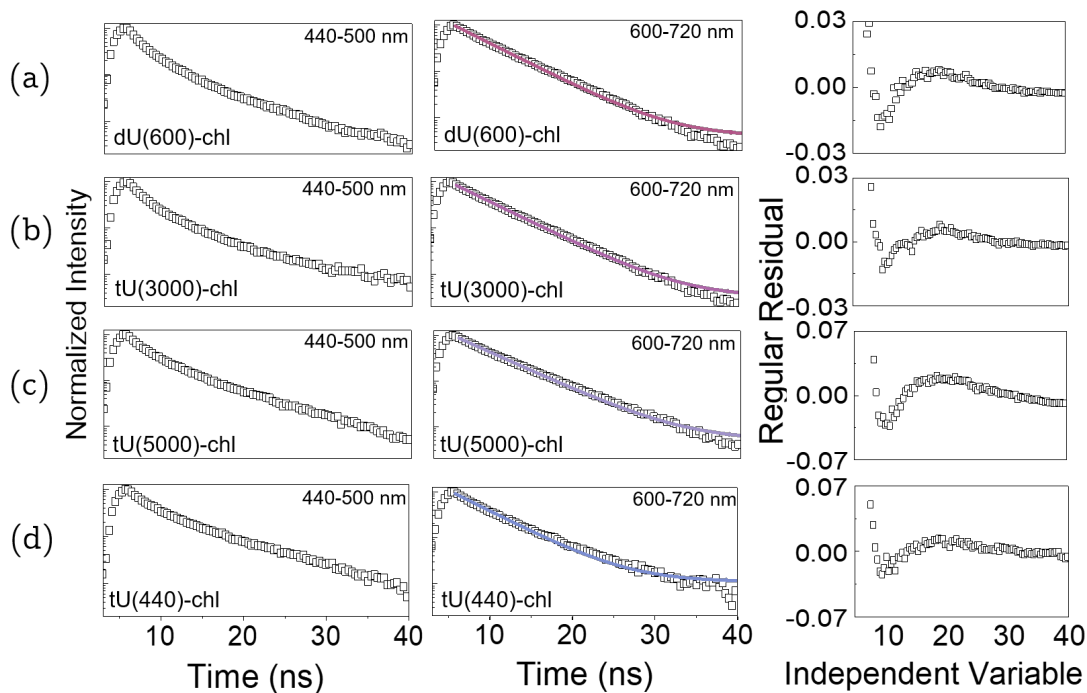
Figure 4.10: Streak based fluorescent decay curves of the different chlorophyll-doped organic-inorganic hybrids: (a) dU(600)-chl, (b) tU(300)-chl, (c) tU(5000)-chl and (d) tU(440)-chl hybrid samples. The first plot on the left corresponds to the fluorescent decay curve integrated over the hybrid host emission band (440-500 nm), followed by the decay curve integrated over the chlorophyll emission (600-720) and the correspondent regular residual of the single exponential function fitted to the data (solid lines, $R^2 > 0.99$). Fluorescence decays were plotted using a logarithmic y-axis.

Table 4.4: Emission lifetime values (τ, ns) of the chlorophyll-doped organic-inorganic hybrids, excited at 379 nm. The fitted decay curves integrated over the emission wavelength ranges of the hybrid host (400-500 nm) and the incorporated chlorophyll molecules (600-720 nm) for each hybrid sample.

λ_{em} (nm)	dU(600)-chl	tU(3000)-chl	tU(5000)-chl	tU(440)-chl
440-500	10.06 ± 0.01	11.15 ± 0.01	10.97 ± 0.01	12.13 ± 0.01
600-720	4.81 ± 0.01	4.92 ± 0.01	5.30 ± 0.02	4.75 ± 0.02

4.2 Spectral analysis of eGFP compounds

4.2.1 UV-Visible-NIR absorption spectroscopy

Tsien and co-workers [34, 91] associated for the first time the two absorption peaks at 398 nm and 475 nm of wild-type green fluorescent protein with the presence of the chromophore in two forms: a neutral (protonated) A form and an anionic (deprotonated) B form, assigning the 395 nm ($S_0^A \rightarrow S_1^A$) and 475 nm ($S_0^B \rightarrow S_1^B$) transitions to $\pi \rightarrow \pi^*$ HOMO-LUMO transitions [119]. Later on, Boxer and co-workers [120] proposed a model for GFP electronic excited states based on three forms of the chromophore and implying excited-state proton transfer (ESPT), a model widely corroborated in the literature [89, 121–123]. The proposed mechanism for the strong green fluorescence of the wild-type GFP, when excited with blue light, is the final result of a fast ESPT taking place. Excitation to the neutral singlet excited state, S_1^A, initiates a fast excited state proton transfer to form an intermediate singlet state, S_1^I, which is the deprotonated chromophore

in the geometry of the neutral ground state. The primary fate of I* is decay back to the S_0^I ground state, from which A is repopulated by reverse proton transfer. Occasionally, during the excited state lifetime of I*, a reorganisation in the protein matrix occurs, which traps the molecule in the S_1^B form.

The presence of the A, B, and I excited states in the case of the eGFP is clearly indicated in the literature [121, 124]. The neutral A is reported to be responsible for the absorption at $\sim$400 nm and emission at 450 nm, whereas the two anionic forms I and B are responsible for the absorption peaking at 488 nm (two overlapping bands at $\sim$470 and $\sim$490 nm, respectively) and the green emission at 510 nm. When excited to the S_1^A state, a fast (10 ps) excited state proton transfer takes occurs in the chromophore, forming the intermediate singlet state S_1^I. The reversible photoconversion taking place in the wild-type GFP between the A, I, and B forms is absent in eGFP, attributed to a larger barrier in the ground state between the protonated A and deprotonated B and I forms compared to that of the natural protein [124]. The Jablonski diagram summarizing the electronic transitions and deactivation pathways of eGFP is presented in Figure 4.11.
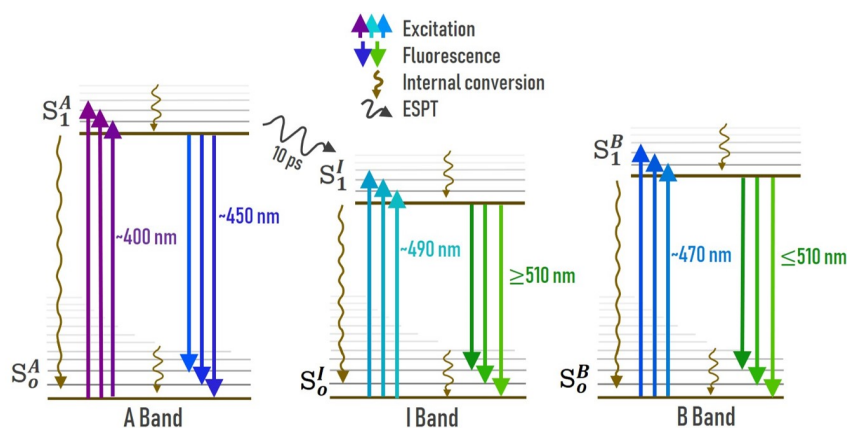

Figure 4.11: Jablonski diagram summarizing the electronic transitions of eGFP.

The absorption spectra of the eGFP-based solutions and the dU(600)-GFP monolith are shown in Figures 4.12(a) and 4.12(b), respectively. The broad shoulder centred at 488 nm (B and I bands) is clearly visible for all samples. The A band is overlapped with water absorption [125], but a small shoulder at $\sim$ 400 nm is detected for both the three solutions and the organic-inorganic hybrid.
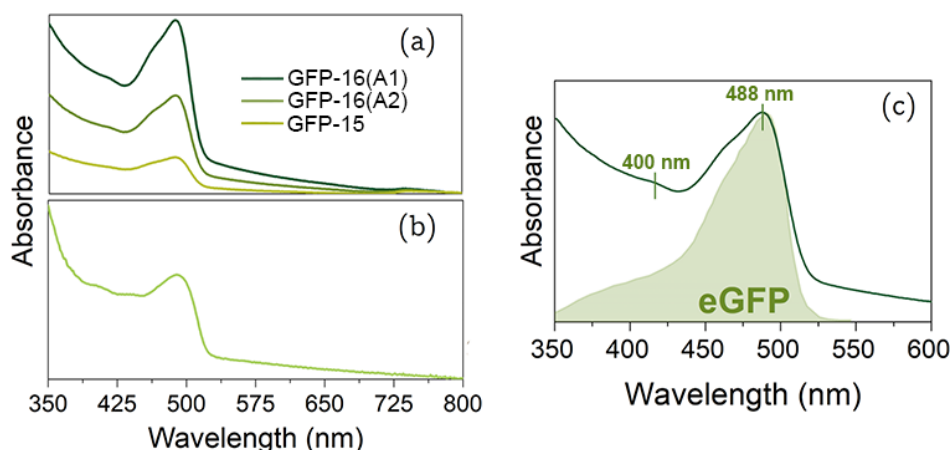

Figure 4.12: Absorption spectra of the eGFP compounds: (a) GFP-16(A1), GFP-16(A2) and GFP-15 solutions and (b) dU(600)-GFP hybrid sample. The A ($\sim$ 415 nm) and B (488 nm) bands of eGFP absorption are visible for all samples. Figure (c) shows the absorption spectra of the more concentrated solution GFP-16(A1) superimposed over the eGFP absorption spectra of ref. [89].

4.2.2 Steady-state photoluminescence

The excitation photoluminescent spectra of the the eGFP aqueous solutions, Figure 4.13, reveal the A (400 nm) and B and I bands (overlapped and peaking at 488 nm) related to GFP excited states. The emission spectra, plotted in the same figure, are dominated by the eGFP characteristic emission peak around 510 nm, with a shoulder at 543 nm. Proteins contain three intrinsically optically active amino-acid residues that contribute to their UV fluorescence: tryptophan, tyrosine and phenylalanine. The first is the dominant source of intrinsic protein fluorescence, with excitation at wavelengths around 280 nm and emission peaking from 300-400 nm [126–128]. The low-intensity emission band centred at 383 nm detected when exciting the solution at ∼287 nm is therefore ascribed to Trp fluorescence.

A supplementary weak emission at 450 nm is due to excitation in the absorption band of the protonated form, whereas the shoulder at ∼287 nm is related to the aromatic region of the protein [124]. The difference between the absorption and emission band maxima, i.e., the Stokes-shift, reported for this solution is ~ 884 cm^{-1} (22 nm), slightly higher than the ones found for the chlorophyll ethanolic solutions. Nonetheless, both eGFP and chlorophyll exhibit small Stokes-shifts, $\sim 640 - 2530$ cm^{-1}, (10-45 nm) due to the rigidity of the chromophore environment, that excludes non-fluorescent relaxation to a ground state [129].
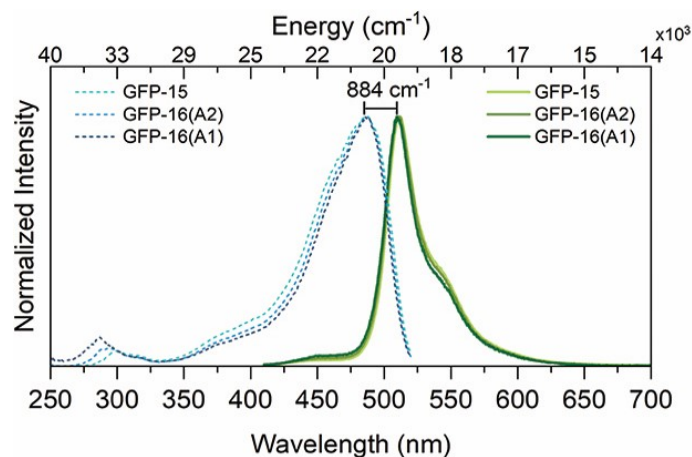

Figure 4.13: Room temperature excitation (dash line) and emission spectra (solid lines) of eGFP aqueous solutions, GFP-15, GFP-16(A2) and GFP-16(A1), monitored at 543 nm and excited at 390 nm.

The photoluminescence of the dU(600)-GFP organic-inorganic hybrid was also studied. Emission and excitation spectra were recorded at room temperature and low temperature (13 K), to analyse the excited states and energy transfer dynamics of GFP and the hybrid host – the room temperature excitation and emission spectra are shown in Figures 4.14(a) and 4.14(b), respectively and Figures 4.14(c) and 4.14(d) display the excitation and emission spectra recorded at 13K.

At room temperature, the excitation spectra are dominated by the eGFP excited states and those of the d-U(600) hybrid host. Monitoring at 512 and 550 nm, within eGFP emission, one can see its characteristic excited states (A, B and I bands, see Figure 4.12). When monitoring the dU(600)-GFP hybrid between 330 and 450 nm, the excitation spectra are dominated by the hybrid excited states that appear in two broad bands, between 250 to 315 nm and 315 to 400 nm. As the detection wavelength increases, the host-related excitation shifts to lower energies (higher wavelengths) [130]. In the same way, the room temperature emission spectra are dominated by the d-U(600) emission, between 315 to ∼600 nm, and the emission of eGFP. The latter appears at 513 nm (with a shoulder centred at 548 nm) when exciting the hybrid at 340 nm, rising in relative intensity as the excitation wavelength rises and approaches its excitation maxima. The eGFP emission peak is slightly red-shifted and broader (∼40 nm versus the ∼31 nm recorder for the solution) when compared with the emission spectra of the solution. The emission broadening observed after the incorporation of eGFP into the hybrid hosts is probably related to changes in the local structure of the protein due to the rigidity of the host [21].
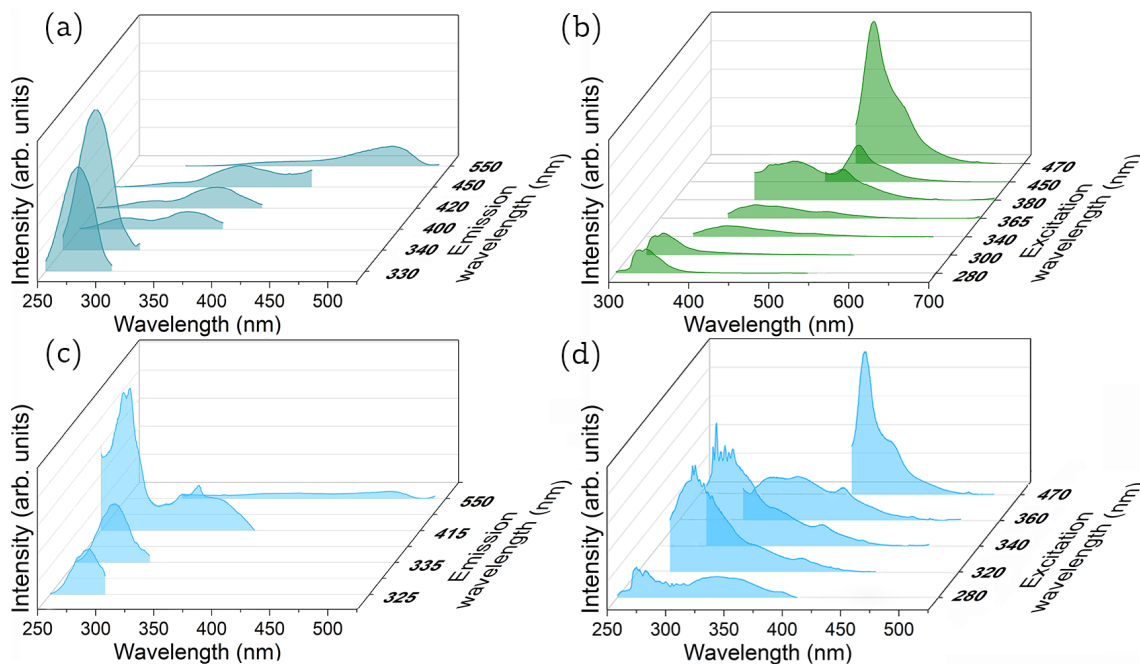
Figure 4.14: Emission and excitation spectra of the dU(600)-GFP organic-inorganic hybrid at room temperature, (a) and (b), and measured at 13K, (c) and (d).

Similar to what was reported for the chlorophyll-based hybrids, the emission spectra of the d-U(600) host is strongly dependent on the excitation wavelength used – the peak position shifts to the red as the excitation wavelength increases and the broad band full width at half-maximum (fwhm) increases. Moreover, the excitation spectrum monitored within the host emission broad band also overlaps with that monitored within the chlorophyll a band in the UV spectral region (from 325 to 400 nm), pointing to energy transfer between the hybrid excited states and eGFP.

The low-temperature excitation and emission spectra (Figures 4.14(a) 4.14(b)) show an increase in the relative intensity (in relation to that of chlorophyll) of the hybrid emission when compared to the spectra at room temperature, due to the decrease of nonradiative thermal activated channels. The characteristic eGFP emission peak is detected for all the selected excitation wavelengths and is blue-shifted in comparison to that of the hybrid at room temperature solution, peaking at 505 nm with a shoulder at 538 nm. The emission fwhm was found to be temperature-dependent: at room temperature the peak is broader ($\sim$40 nm) than the one at 13K ($\sim$26 nm). eGFP emission is reported to blue shift and become narrower at lower temperatures due to the temperature dependence of the I excited state [121, 131]. The excitation peak around 488 nm is also narrower at 13K than at room temperature, supporting the hypothesis that the shift and narrowing of eGFP emission is due to depopulation of the I excited state.

The emission properties of the eGFP solutions and of the dU(600)-GFP hybrid were further studied through measurements of the absolute emission quantum yield as a function of the excitation wavelength. On the case of the eGFP-based solutions, Table 4.5, the quantum yield is higher when the excitation wavelength is resonant with the B and I bands of GFP absorption (488 nm) and maximum (0.52$\pm$0.05) for the GFP-16(A2) solution.

The dU(600)-GFP hybrid emission quantum yield was measured in detail along the eGFP excitation profile (360-500 nm), as shown in Table 4.6. The quantum yield values near the excitation maxima of GFP (470-500 nm). It is important to point out that the values for these wavelengths are very similar and in each others margin of error, so although Φ is highest (0.33$\pm$0.03) at 490 nm, it is in practice the same between 470-500 nm. The emission quantum yield reported for the hybrid sample at the excitation maxima of eGFP is lower than that reported for the solution, suggesting a quenching of the GFP emission after its incorporation into the host matrix. No significant spectral changes in the absorption spectra were reported for the different GFP solutions, i.e. for different GFP concentrations, although the absolute absorbance value increased for higher

concentrations (Figure 4.12(a)).

Table 4.5: Absolute emission quantum yield (Φ) as a function of the excitation wavelength measured for the eGFP-doped solutions. The relative yield error is $\frac{\Delta\Phi}{\Phi} = 0.1$ (10%).

	Φ_{370nm}	Φ_{488nm}
GFP-15	0.067	0.494
GFP-16(A2)	0.109	0.519
GFP-16(A1)	0.123	0.505

Table 4.6: Absolute emission quantum yield (Φ) as a function of the excitation wavelength measured for the eGFP-doped organic-inorganic hybrid. The relative yield error is $\frac{\Delta\Phi}{\Phi} = 0.1$ (10%).

	Φ_{360nm}	Φ_{370nm}	$\Phi_{380-390nm}$	Φ_{400nm}	Φ_{410nm}	Φ_{420nm}	Φ_{430nm}
	0.057	0.060	0.064	0.079	0.080	0.088	0.111
dU(600)-GFP	Φ_{440nm}	Φ_{450nm}	Φ_{460nm}	Φ_{470nm}	Φ_{480nm}	Φ_{490nm}	Φ_{500nm}
	0.140	0.183	0.219	0.309	0.311	0.332	0.314

The absorbance dependence on the concentration was further studied for the eGFP samples through molar extinction coefficient calculations, Table 4.7), at the absorption maxima (488 nm), revealing analogous values within 9.3-10.3 $\times 10^3$ M^{-1} cm^{-1}. These are in the same order of magnitude as previously reported in the literature (55-57 $\times 10^3$ M^{-1} cm^{-1}) [34, 132, 133]. Likewise, ϵ was calculated at the eGFP absorption maxima (488 nm) for the eGFP-doped monolith. The molecular density of eGFP in the hybrid host was calculated based on the premises that all the solvent (added or produced over the sol–gel condensation) evaporated after the processing and the density of the resulting hybrid monolith was ∼1.0 g cm^{-3}, approximating the molecular eGFP concentration in the monolith to that of the incorporated solution, 3×10^{16} per cm^3.

The molar extinction coefficient can be related with the absolute emission quantum yield, Table 4.5, through the brightness parameter, Eq. 2.2. The emission quantum yield values reported for the solutions are in agreement with the literature [34, 133]. The B values were calculated as function of the eGFP concentration (Table 4.7). Comparing the results for the eGFP solutions, at higher eGFP concentration, GFP-16(A2) and GFP-16(A1), B decreases, although not significantly, due to a decrease in the ϵ parameter (Φ values were very similar for the three solutions). To further study and confirm this trend, a broader range of concentrations needed to be tested.

The B values calculated for the eGFP solutions are akin to those previously reported for different green fluorescent proteins mutants [134] and other organic dyes [21, 135], albeit lower than those reported for R-phycoerythrin [13].

Table 4.7: Calculated molar extinction coefficient (ϵ) and brightness (B) at 488 nm for the three eGFP solutions and the eGFP-doped organic-inorganic hybrid.

	$\epsilon(\times 10^3)$ **M^{-1}cm^{-1}**	$B(\times 10^3)$ **M^{-1}cm^{-1}**
GFP-15	10.4	5.1
GFP-16(A2)	9.3	4.8
GFP-16(A1)	9.8	5.0
dU(600)-GFP	1.6	0.5

4.2.3   Fluorescence lifetime analysis

The time-resolved study of the photoluminescence properties of the eGFP-based samples followed the same sequence as the one described for the chlorophyll-based solutions and monoliths. The decay of eGFP fluorescent over time in the eGFP solutions was studied, exciting in the A band (390 nm) and monitoring at the emission maxima of eGFP (510 nm). The decay curve of GFP-16(A1), Figure 4.15, was fitted by a single exponential function ($R^2 > 0.99$), yielding $\tau = 3.40 \pm 0.11$ ns. The fluorescent decay curves of the GFP-15 and GFP-16(A2) solutions also exhibit single exponential behaviour ($R^2 > 0.99$), with associated emission lifetimes of 3.41 ± 0.11 ns and 3.33 ± 0.11 ns, respectively. These values are in agreement with those reported in the literature, $\tau \sim$2-3 ns [136, 137].
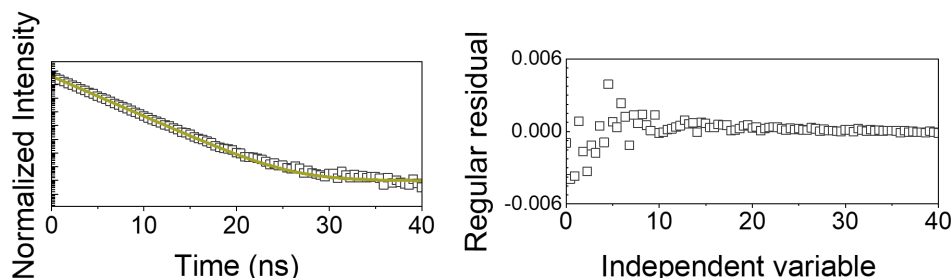

Figure 4.15: Fluorescent decay curve of eGFP in an aqueous solution: GFP-16(A1), excited at 390 nm and monitored at 510 nm, using a logarithmic y-axis. The plot on the right shows the correspondent regular residual of the single exponential function fitted to the data ($R^2 > 0.99$).

Streak camera images were recorded for the eGFP solutions the eGFP-doped organic-inorganic hybrid. The images recorded for the different samples were very similar – the emission maxima at 510 nm was quite evident in all images recorded, as was the shoulder at $\sim$540 nm, both characteristic of eGFP emission. For that reason, only two of the recorded streak images are shown in this thesis, one of the GFP-16(A1) solution – chosen to be representative of the other two since it was the one incorporated in the hybrid host – and the other of the dU(600)-GFP hybrid monolith, Figures 4.16(a) and 4.16(b). The streak images are presented together with the fluorescence emission spectra integrated over 40 ns, Figures 4.16(c) and 4.16(d), and are again colour-coded from dark blue (low intensity) to red (high intensity). Five images were recorded for each sample
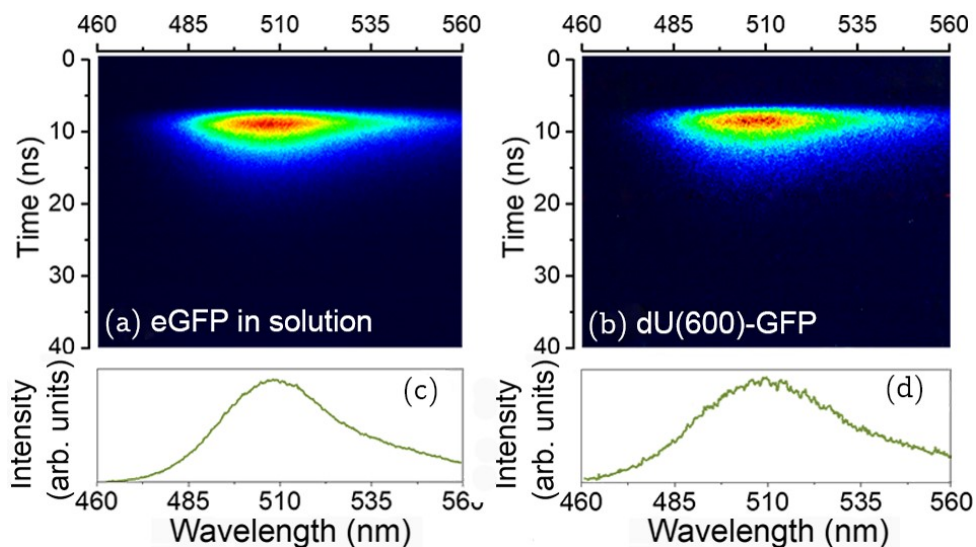

Figure 4.16: Comparison between the streak image of the eGFP in solution and that of the hybrid sample: (a) GFP-16(A1) solution and (b) dU(600)-GFP monolith. The respective integrated fluorescence emission spectra, (c) and (d), are shown on the bottom.

under the same conditions: the 467 nm picosecond pulsed diode was the excitation source and a 150 g/mm grating was used in the spectrograph, covering a 100 nm spectral range, resulting in an improvement of the spectral resolution (1.4 nm) in comparison to the chlorophyll streak studies.

Qualitatively, one can see that the emission is more intense around 510 nm (red area) for both the solution and organic-inorganic hybrid. The SNR is much lower in the streak image recorded for dU(600)-GFP due to the lower intensity of eGFP emission, justified by the decrease in the number of eGFP optical active centres. The emission band is, however, very similar in the two samples in terms of spectral range and temporal duration (<15 ns).

Fluorescent decay curves were integrated over the full wavelength range (460-560 nm) of each image and fitted with single exponential functions resorting to the fluorescence lifetime data fitting software (TA-FIT) of the control and readout unit of the streak camera. The fluorescent lifetimes of each sample and respective associated error were calculated through a mean of the lifetimes obtained for the 5 images (the error corresponds to the maximum deviation to the mean). The decay curve and fittings performed for the streak images of Figure 4.16 are presented in Figure 4.17, as a representative example.
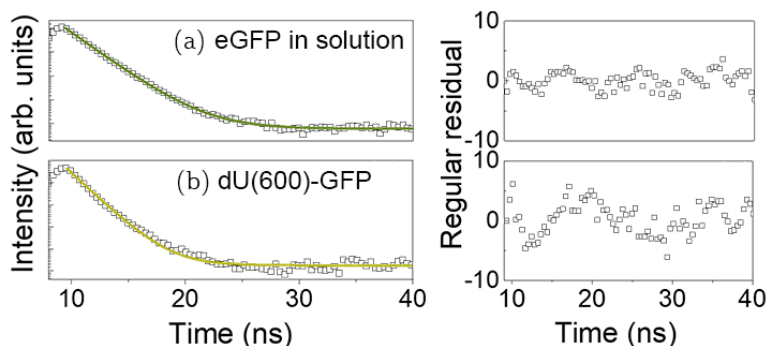

Figure 4.17: Streak-based fluorescent decay curves of eGFP in solution and incorporated into the hybrid host: (a) GFP-16(A1) solution and (b) dU(600)-GFP hybrid sample, plotted with a logarithmic y-axis. The correspondent regular residual of the single exponential function fitted to the data ($R^2 > 0.99$) are aside each plot.

The lifetime values obtained with the streak camera for the eGFP solutions and organic-inorganic hybrid with single exponential functions are lower than the ones measured with a spectrofluorimeter, Table 4.8. In the latter, the excitation was made within the A band, therefore favouring the ESPT to the I state, which has a longer lifetime than that reported for the B band. Further studies of the decay curves measured with the streak camera were carried out by applying a two exponential decay model to the decay curves, due to simultaneous excitation of the two distinct fluorescent states B and I, responsible for the radiative deactivation of eGFP at ~510 nm. The lifetimes resulting from the data best fit ($R^2 > 0.99$) for the three solutions and the hybrid sample were $\tau_1 \sim 1.5 - 1.9$ ns and $\tau_2 \sim 2.97 - 3.08$ ns, Table 4.8, in agreement with the reported in the literature for the B and I excited states, respectively [124, 136].

Table 4.8: Emission lifetime values (τ), calculated from the best fit to the decay curves measured for the eGFP solutions and eGFP-doped organic-inorganic hybrid with the spectrofluorimeter and streak camera.

	Spectrofluorimeter	Streak camera	
	τ (ns)	$\bar{\tau}$ (ns)	τ_1/τ_2 (ns)
GFP-15	3.41 ± 0.11	2.89 ± 0.01	$1.9 \pm 0.1/3.08 \pm 0.05$
GFP-16(A2)	3.33 ± 0.11	2.92 ± 0.02	$1.8 \pm 0.3/3.02 \pm 0.03$
GFP-16(A1)	3.40 ± 0.11	2.94 ± 0.02	$1.5 \pm 0.3/2.97 \pm 0.04$
dU(600)-GFP	-	2.06 ± 0.02	$1.6 \pm 0.1/3.2 \pm 0.3$

5. Monte-Carlo ray-tracing simulations

Although LSCs devices have been the target of extensive research, their optical efficiency is still very low, preventing their large scale commercialization. Maximizing the performance of the LSCs is therefore a priority in the field, and simulations can be of great assistance in this task, helping with design optimisation – simulating the behaviour of light in materials with specific properties offers a flexible tool for the design of LSC with various photoluminescent characteristics, proportions and layouts, without actually producing the different prototypes, which saves time and reduces costs.

Monte Carlo algorithms are stochastic in nature and often used in situations when no deterministic algorithm can be found and/or the problem variables have coupled degrees of freedom. In a typical Monte Carlo algorithm, random draws following given distributions define a chain of local events characterizing the global event and leading to a final state. The accuracy of this solution depends on how well the problem is modelled and how many draws are made [138]. Many events that occur in an LSC are inherently probabilistic, and thus can be well described by Monte Carlo simulations. Based on splitting the incident radiation in a finite number of beams, the algorithm traces each ray that enters the LSC matrix, returning information on whether the photons were trapped inside the LSC, absorbed by the luminophores, lost in the matrix, or collected at the edges [139]. This chapter serves an introduction to Monte-Carlo ray-tracing simulations, with an overview of the program used in the computational simulations performed during the course of this thesis, which are subsequently detailed and discussed.

5.1 PVtrace program

5.1.1 General overview

The Monte-Carlo ray-tracing simulations undertaken during the course of this thesis were performed resorting to an open source ray-tracing program, *pvtrace*. Written in the Python programming language by Dr Daniel Farrell [140], the program uses geometric optics and Monte Carlo simulations to model photon interactions with an LSC.

A great variety of objects with different geometries, incident light sources, absorption and emission spectra, emission quantum yields and refractive indices can be modelled with pvtrace. The interaction of photons with a specific LSC can be simulated by writing a script which tells pvtrace to model the LSC's shape (e.g. cuboid or cylindrical), its dimensions and material, specifying the LSC's absorption and emission spectral data, its emission quantum yield and refractive index. Likewise, the incident light source can be simulated by entering the desired light source's spectrum, position, whether it is a planar or a point source, and the number of emitted (thrown) photons. Additional coding allows for the simulations to be shown in a 3D visualizer program and instructs the script to save the data generated in the simulations. After the program traces all the thrown photons, an output file is generated summarising their fate – the end point location of the photons is returned through the percentage of photons that left through the LSC's edges and from the front and back surfaces, along with the percentage of lost photons. This is done for "luminescence photons" (those absorbed and re-emitted by the luminophores) and "solar photons" (those which are unabsorbed). The η_{opt} of the LSC can be calculated from the outputs of the simulation, corresponding to the ratio between the number of photons exiting the device from the edge(s) where the PV cell is(are) placed, to the number of incident photons.

During the course of this thesis, the developer of *pvtrace* was contacted through the GitHub platform, which was followed by an exchange of several messages in the scope of improving the then available version of the program, as some architectural flaws were detected (the 3D visualisation module initially didn't run and programming coatings object for objects with non-rectangular geometries was not possible). pvtrace was later updated to *pvtrace 2.0*, but all the simulations performed were done with the older version (*pvtrace 1.4*).

5.1.2 Algorithm

The algorithm behind *pvtrace* ray-tracing follows the subsequent described logic, summarised with a flowchart in Figure 5.1. First, the light source's emission spectrum is transformed into a probability distribution function that can be sampled by uniformly distributed random numbers to reproduce the original data. Then, an incident photon is generated with the sampled wavelength, at a certain position and with a certain direction, determined by the nature of the light source (e.g. punctual or planar) and attributed by random numbers.

At an interface with an object, the Fresnel reflection probability is calculated based on the defined refractive indices and angle of incidence. This is compared to a random number to determine whether the photon is reflected or refracted. If the photon is reflected and has no more objects with which to intersect, the photon is stopped, the information regarding its journey is registered and the algorithm re-starts. If refraction occurs, Snell's law is applied and the photon direction is updated. Next, the following interface intersection point is found and the path length between these two intersection points is calculated. The absorption path length is also calculated resorting to the Beer-Lambert law, dependent on the photon's wavelength and the object's absorption coefficient at that wavelength. The two path lengths are compared to determine whether the photon is absorbed or not. In case absorption does not occur, the photon can either hit another interface or not – if the latter happens, the photon leaves the LSC through the escape cone; if the photon hits the following interface, the algorithms re-starts. On the other hand, when the photon is absorbed it is either re-emitted at a probabilistically determined red-shifted wavelength or lost non-radiately. A photon not re-emitted is lost through non-radiative relaxation due to a non-unity emission quantum yield and is permanently lost from the simulation. The direction of the re-emission is modelled to be entirely random for isotropic emission and re-emitted photons then follow the same interface calculations.
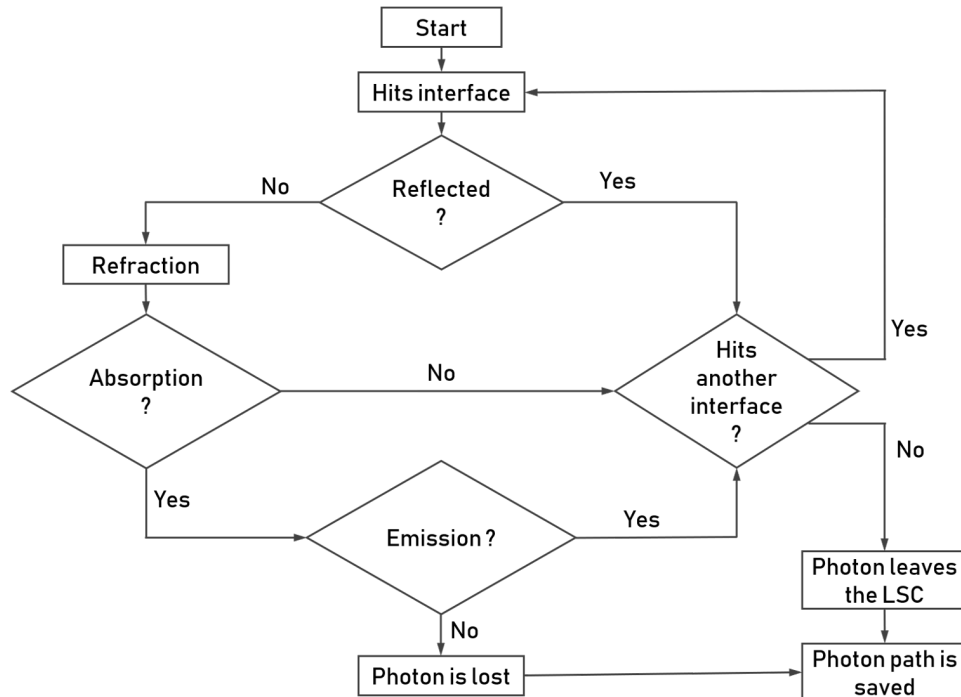

Figure 5.1: Flowchart presenting the basic outline of the pvtrace algorithm.

5.2 p-LSC simulations

To assess the potential of eGFP as a luminophore in LSC applications, ray-tracing simulations of eGFP-based LSCs were performed with the pvtrace program. Two different planar prototypes were proposed and tested based on previous works [13, 21]: a p-LCS based on a glass container filled with eGFP dispersed in an aqueous solution and a second p-LSCs with eGFP incorporated into a di-ureasil amine-functionalised organic–inorganic hybrid. Figures 5.2(a) and 5.2(b) show the 3D visualiser of the pvtrace program, after the simulations of the liquid and bulk p-LSCs, respectively, were completed.
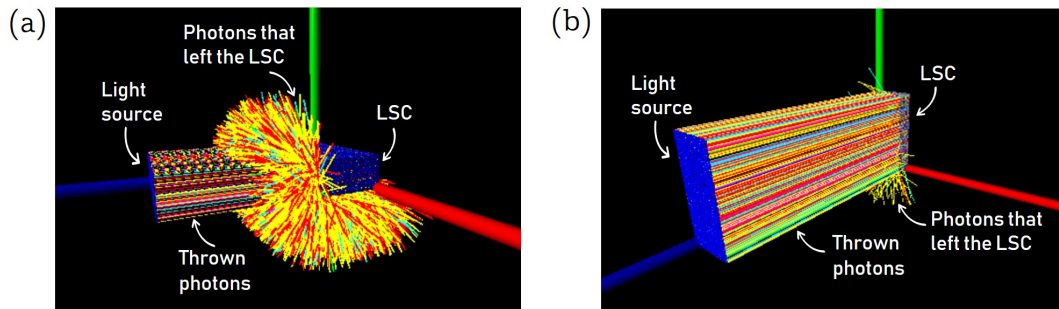

Figure 5.2: 3D visualizer of the pvtrace program. Screenshot of the (a) liquid eGFP-based and (b) bulk eGFP-doped p-LSCS simulations after completion.

In both cases, a planar light source emitting 10^5 photons, sampled from the Air-Mass 1.5G (AM1.5G) solar spectrum (emitted by the solar simulator used in the forthcoming experimental performance quantification of the LSCs), shown in Figure 5.3, was defined as one of the input parameters of the Monte Carlo ray-tracing simulations.
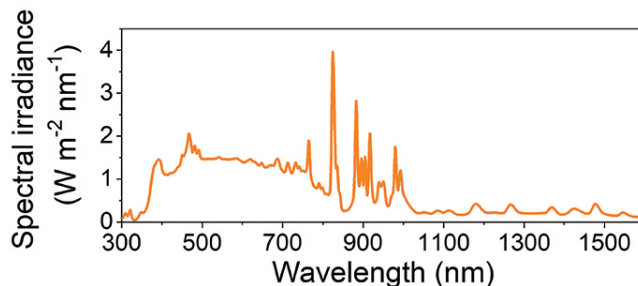

Figure 5.3: AM1.5G solar irradiance spectrum used as an input parameter in the Monte Carlo ray-tracing simulations.

The absorption and emission spectra of the liquid p-LSC were given as input parameters in the simulations correspond to those of the GFP-16(A1) solution, see Figures 4.12(a) and 4.13(b), respectively. The absorption spectrum of the dU(600)-GFP sample in Figure 4.12(c) and the emission spectra excited at 470 nm of Figure 4.14(b) were used as input parameters in the bulk p-LSC simulation. The absolute emission quantum yield values entered were the ones measured experimentally for these samples when exciting them at the eGFP excitation maxima ($\sim$488 nm) – 0.505 for the liquid p-LSC, see Table 4.5 and 0.332 for the bulk p-LSC, see Table 4.6). Furthermore, a refractive index of 1.33 was considered in the case of the liquid p-LSC, since it consists of an aqueous solution [141], while in the case of the bulk device an $n = 1.5$ was assumed [21].

In the case of the liquid p-LSC, several simulations were performed, considering the same parallelepiped LSC ($l\times2\times1$ cm^3) with different heights l, resulting in liquid LSC with solution volumes ranging from 1 to 8 $\times10^{-6}$ m^3. The dimensions used in the simulation of the bulk device correspond to those of the dU(600)-GFP sample, $0.9 \times 0.4 \times 1.9 \times 10^{-6}$ m^3. Both p-LSC were simulated considering a single PV cell attached to the bottom of the device, with reflective tape (reflectance of 100%) on the remaining edges and back surfaces.
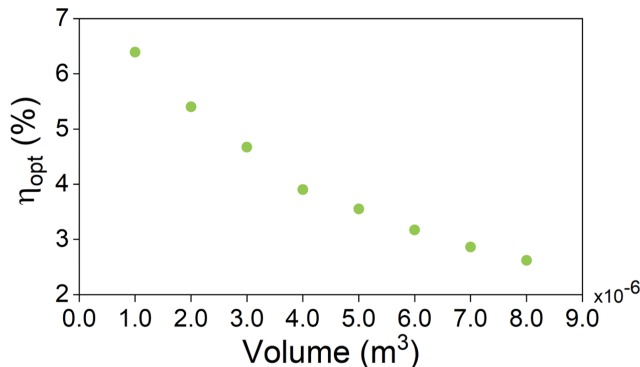
Figure 5.4: η_{opt} values calculated for a liquid planar, eGFP-based LSC.

Figure 5.4 shows the simulated η_{opt} values when modelling the liquid LSC with different solution volumes. For consecutive higher volumes, the optical efficiency of the devices decreases, starting at 6.4% with 1×10^{-6} m^3 of solution and reaching 2.62% for 8×10^{-6} m^3 of the GFP-16(A1) solution. Although there is an increase in the number of optical active centres, with smaller solutions volumes the path lengths to reach the PV cell are, on average, much smaller. Hence, the probability of losing a photon through non-radiative emission before it reaches the PV cell at the bottom of the device is smaller. This is confirmed by the increase in the percentage of lost photons (due to the non-unity quantum yield of the solution and photon re-absorption) with increasing solution volume (from 24.5% to 27,5%). For all volumes, only luminescent photons reached the PV cell – solar photons all exited the LSC through the front of the device, together with 5-6% of the luminescent photons (scape cone).

When modelling the bulk LSC, 0.18% of the incident photons left the LSC through the bottom edge of the LSC, where the PV cell would be attached, which results in an η_{opt} of 0.18%. Once again, only luminescent photons were collected in the PV cell, with solar photons all exciting the LSC through the front surface (97.7%). The percentage of lost photons was 1.9%, highlighting the main problem with organic molecules acting as luminophores in LSC – re-absorption caused by small Stokes-shift values decreases the efficiency of the device.

Several aspects are important to point out regarding the simulations just described: interference effects are neglected in this algorithm, which also assumes the emitted rays cannot split when reaching an interface, imposing that they either be transmitted or reflected, as predicted by Fresnel laws. The refractive index of the LSC is assumed to be constant and independent of photon wavelength, while scattering and wave interference events are not taken into consideration. Moreover, the fluorescence quantum yield of the fluorescent material is assumed to be constant, regardless of the incident photon energy. Reflection at the waveguide edges and LSC/PV coupling losses are completely ignored (the PV cell attached to the bottom of the LSC is assumed to be perfectly coupled). The refractive index of the fluorescent particles embedded inside the host matrices assumed to be the same as the host matrix. The luminescent particles are assumed to be dispersed homogeneously throughout the LSC system; thus, the absorption spectrum is constant throughout the LSC system. Host matrix modification of the absorption and emission spectrum of the fluorescent material is ignored. Additionally, the reflectance of the reflective tape that covers the edges of the devices is considered to be 100%, which is not reproducible experimentally. All of these factors have to be taken into account when comparing the output values of the simulations to experimentally measured values and are aspects to be improved in the simulations – the more we approximate the algorithm's input variables to experimental conditions, the more similar the simulations will be to the experimental results.

6. Luminescent solar concentrators prototypes

Towards organic-based sustainable LSCs devices, two different planar prototypes were proposed and tested – p-LCS based on a glass container filled with eGFP dispersed in an aqueous solution (eGFP solutions, Table 3.1) and a second p-LSCs with eGFP incorporated into a di-ureasil amine-functionalized organic–inorganic hybrid (dU(600)-GFP, Table 3.2). The performance quantification of the previously mentioned eGFP-based LSCs is described in this chapter.

6.1 Experimental

The experimental optical conversion efficiency, η_{opt} (Eq. 2.7), and external quantum efficiency, EQE (Eq. 2.9), values were determined with the experimental setups schematized in Figures 6.1(a) and 6.1(b). To separate the solar radiation into the different wavelengths for EQE measurements, the solar simulator was coupled to a monochromator (Triax 180, Horiba Scientific).
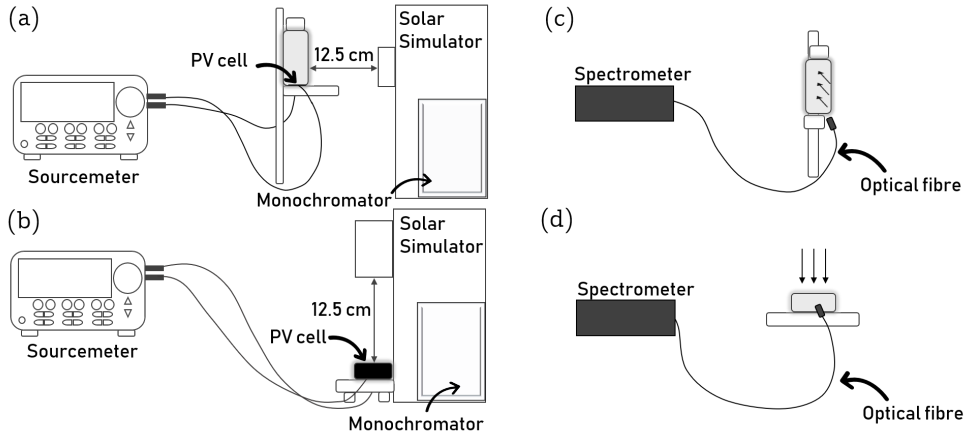

Figure 6.1: Schematic representation of the experimental setup used for η_{opt} and EQE calculations for the (a) eGFP-based liquid and (b) eGFP-doped di-ureasil bulk p-LSCs (without and with the monochromator). Schematic representation of the experimental setup used for edge emission spectra measurements for the (c) liquid and (d) bulk LSCs, respectively. The direction of the incident light emitted by the solar simulator (placed as in (a) and (b)) is indicated by the arrows.

The LSC devices were irradiated with AM1.5G illumination, using a 150 W xenon arc lamp, class A solar simulator (Model 10500, Abet Technologies), Figure 5.3. The incident power received by the LSCs per unit area, $1000\ \mathrm{Wm^{-2}}$, was calibrated by adjusting the distance between the solar source and the LSCs (12.5 cm). The output optical power at the edge of the LSCs was estimated resorting to a c-Si PV cell (KXOB22-01X8L, IXYS), with maximum EQE $\sim$80%. I_{SC}^{L} and V_{0}^{L} values were measured using a sourcemeter device (2400 SourceMeter SMU Instruments, Keithley). Reflective tape (reflectance $\sim$70-80% between 350 and 800 nm), was used on all the edges and in the back of the LSCs. As the PV device was coupled to a LSC, input power P_{in} values were measured using the previously mentioned sourcemeter and a c-Si calibrated photodiode (FDS1010, Thorlabs) through an approximation,

$$P_{\mathrm{in}} = \frac{A_e}{A_s}\frac{R_{PD}R_L}{V_{PD}}\frac{A_{PD}}{A_{PV}}, \tag{6.1}$$

yielding

$$EQE = \frac{I_{SC}}{e} \frac{hc}{\lambda} \frac{A_e}{A_s} \frac{R_{PD}R_L}{V_{PD}} \frac{A_{PD}}{A_{PV}}. \tag{6.2}$$

In this expression, A_s and A_e represent the exposed and total edge area of the LSC, R_{PD}, V_{PD} , R_L and A_{PD} the responsivity, the output voltage, the coupled load resistor (10 kΩ) and the active area of the reference calibrated photodiode, respectively, and A_{PV} corresponds to the area of the PV device.

Edge emission spectra measurements were performed for both planar LSCs, again resorting to the same experimental setups. The cuvette/bulk monolith were placed without the PV cell in the same positions, under solar simulator illumination, and an optical fibre with an inner diameter of 450 μm (QR450-7-XSR, Ocean Optics), coupled to a portable spectrometer (Compact Fibre Spectrometer CCS100, Thorlabs), was placed on the edges of the LSCs, Figure 6.1(b).

6.2 Optical characterisation

Liquid eGFP-based p-LSC

In the scope of this thesis, one type of LSCs fabricated were planar LCS based on a glass cuvette filled with the three eGFP solutions whose optical characterisation was previously detailed. The cuvette was filled to the brim, 8×10^{-6} m^3, with one solution at a time and studied for LSC applications. Figure 6.2(a) shows the liquid planar LSC filled with the GFP-16(A1) solution under AM1.5G illumination. The LSC emission, visible to the naked eyes and green coloured Figure 6.2(b), is ascribed to the eGFP transitions (Figure 4.13) and is guided, through total internal reflection, to the edges of the device. The PV cell is attached to the bottom of the cuvette and the remaining edges of the LSC, along with the backside, are covered with reflective tape. The dimensions of the LSC and attached PV cell are detailed in Figure 6.2(c).

(a)   (b)   (c)
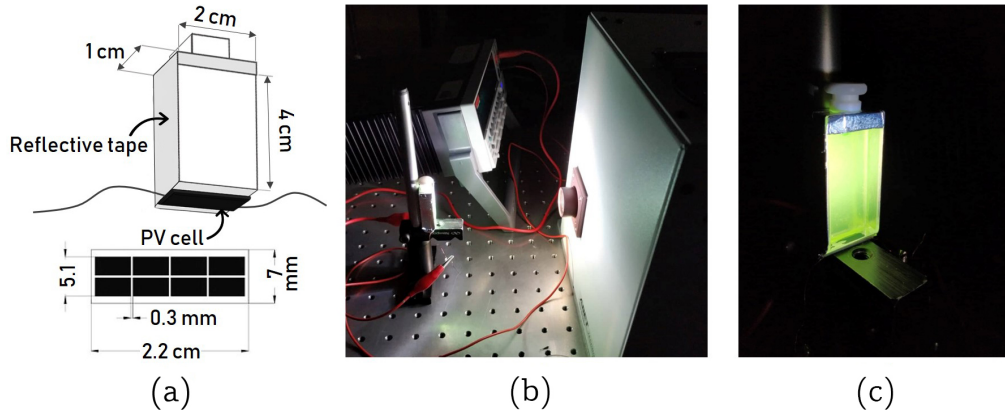
Figure 6.2: Photographs of (a) the liquid p-LSC attached to a Si PV cell under AM1.5G illumination and of (b) the green emission of the LSC under said illumination; (c) schematic representation of the same p-LSC, specifying in finer detail its dimensions and the ones of the attached PV cell.

The LSCs' performance was quantified through η_{opt}, F and EQE calculations, presented in Table 6.1.

Table 6.1: Performance quantification of the liquid p-LSC prototypes tested through η_{opt}, G, F and EQE calculations. EQE values referrer to the maximum values measured at 490 nm.

	Sample	$\eta_{\text{opt}}(\%)$	G	F	EQE (%)
	GFP-15	2.07 ± 0.02		0.083 ± 0.001	2.9
Liquid p-LSC	**GFP-16(A2)**	2.48 ± 0.04	4	0.099 ± 0.002	3.5
	GFP-15(A1)	2.99 ± 0.01		0.120 ± 0.001	3.8

Three measurements were made for each liquid LSC, so the average value is reported. The EQE values correspond to the maximum reached, for 490 nm. The larger EQE variation was between 450-520 nm for the three p-LSCs, implying that the EQE values are well correlated with the B and I absorption bands of eGFP.

The dependence of the LSC performance with the number of eGFP optical centres was also investigated. To do so, the glass cuvette was filled progressively with 1 to 8 $\times 10^{-6}$ m^3 of each solution and η_{opt} and EQE values were calculated in each step. When changing the volume of the solutions, η_{opt} values follow the same trend for the more concentrated solutions, GFP-16(A1) and GFP-16(A2), Figure 6.3, starting at the same value, continuously rising with the volume increase and reaching maximum values of 3.27 ± 0.07 and 2.83 ± 0.03 at 7 and 6 $\times 10^{-6}$ m^3 of solution, respectively. GFP-16(A1), the more concentrated solution of the two, has a steeper rise. The more diluted solution, GFP-15, reaches η_{opt} maximum values with less solution volume, 2.78 ± 0.09 at 5 $\times 10^{-6}$ m^3 [1]. Maximum η_{opt} values were found for the most concentrated solution.
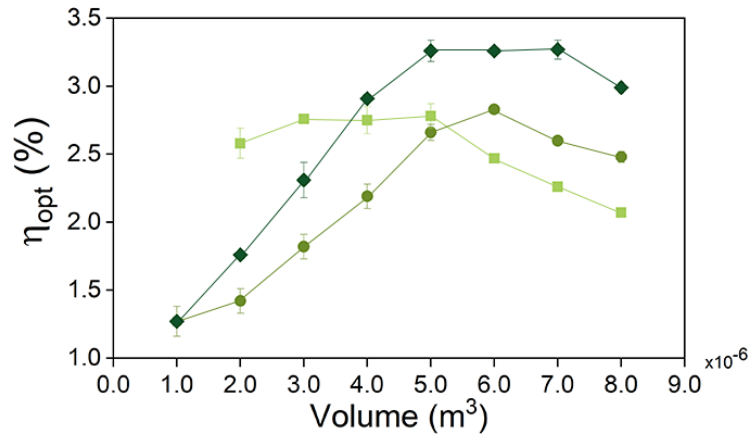

Figure 6.3: η_{opt} values calculated for each liquid p-LSC as the glass cuvette was progressively filled with the three eGFP solutions: GFP-15 (square, light green), GFP-16(A2) (circle, green), and GFP-16(A1) (diamond, dark green). The lines serve as visual guides.

The experimental results were reported are different those obtained in the Monte Carlo ray-tracing simulations (Figure 5.4), where the η_{opt} decreased with single exponential behaviour with increasing volume. In the simulations, the LSC/PV coupling losses were neglected, the refractive index and fluorescence quantum yield of the LSC were assumed to be constant and independent of photon wavelength and the a 100% reflectance was assumed for the reflective tape, which could be responsible for the discrepancy between the simulations and the experimental results. Moreover, only photons emitted by eGFP reached the PV cell in the simulations, probably due to the approximations behind the ray-tracing algorithm (no interference or scattering effects were considered). This was not verified experimentally – EQE values (calculated following the same procedure) for the GFP-15, GFP-16(A2) and GFP-16(A1)-based liquid p-LSCs, Figures 6.4(a), 6.4(b) and 6.4(c), indicate that solar photons indeed reached the PV cell.

The maximum EQE values were found within eGFP excitation band (shoulder between 450 and 520 nm), for all solution volumes. As EQE measurements are an indicator of the number of incident photons of a specific wavelength arriving at the PV cell, an increase in EQE when illuminating the LSC with eGFP absorption wavelengths indicates that the light arriving at the PV cell has the strongest contribution from eGFP-converted photons. The shoulder in the EQE in the eGFP absorption region is more pronounced with increasing volume, which is justified by the increase in the number of eGFP optically active centres, which directly influences the number of eGFP-converted photons that reach the PV cell. However, all three LSCs displayed a continuous decrease in absolute % with increasing volume. When increasing the volume, the optical path is increased, henceforward increasing the influence of phenomena as scattering and reabsorption, resulting in an overall lower number of photons arriving at the PV cell and a decrease in EQE

---

[1]The I_{sc}^L measured for 1 μm^3 of this solution was abnormally high and out of trend, resulting in a η_{opt} value much higher (4.52 ± 0.13) than the rest, and therefore disconsidered.
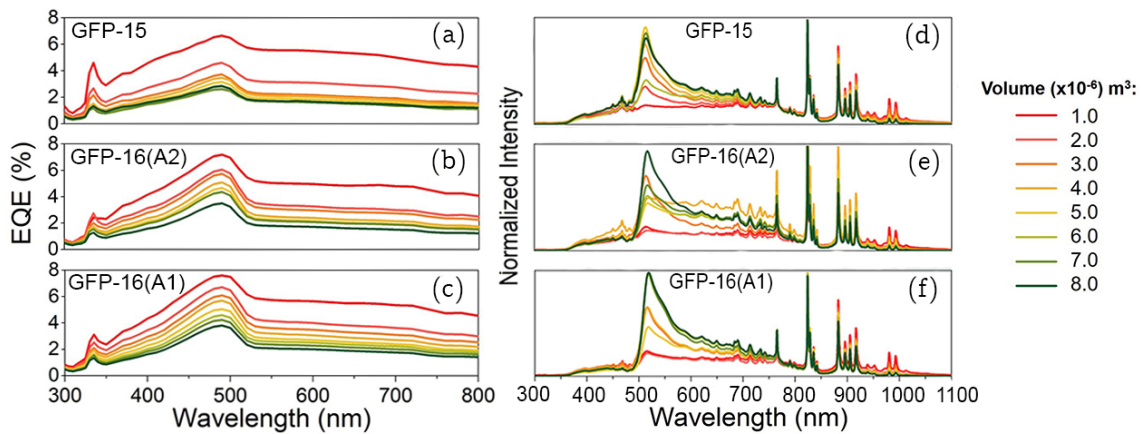
Figure 6.4: EQE values calculated and emission spectra recorded at the edge of the LSC for each liquid p-LSC as the glass cuvette was progressively filled with the three eGFP solutions: (a)(d) GFP-15, (b)(e) GFP-16(A2) and (c)(f) GFP-16(A1).

and η_{opt} values. Emission spectra at the edge of the cuvette, where the PV cell is placed, were also measured for the three liquid LSC, Figure 6.4(d), 6.4(e) and 6.4(f). All three showcased a peak at 515 nm, ascribed to eGFP emission, that grows in intensity in comparison to that of the solar spectrum with increasing solution volume, due to the increase in the number of eGFP luminophores. The highest eGFP relative emission was recorded for the GFP-16(A1) solution LSC, Figure 6.4(c), justified by the higher number of optical active centres (higher concentration, more molecules in the same volume).

The overlap integral O, Eq. 2.10, between the eGFP solutions absorption spectra and the solar irradiation on Earth was also calculated, presented in Figure 6.5. The O values increase with higher eGFP concentration. The maximum calculated O value, 3.4×10^{20} photons s^{-1} m-2, indicates that the GFP-16(A1) aqueous solution has the potential to absorb ~8% of the solar photon flux on the Earth (4.3×10^{21} photons s^{-1} m-2) [73].
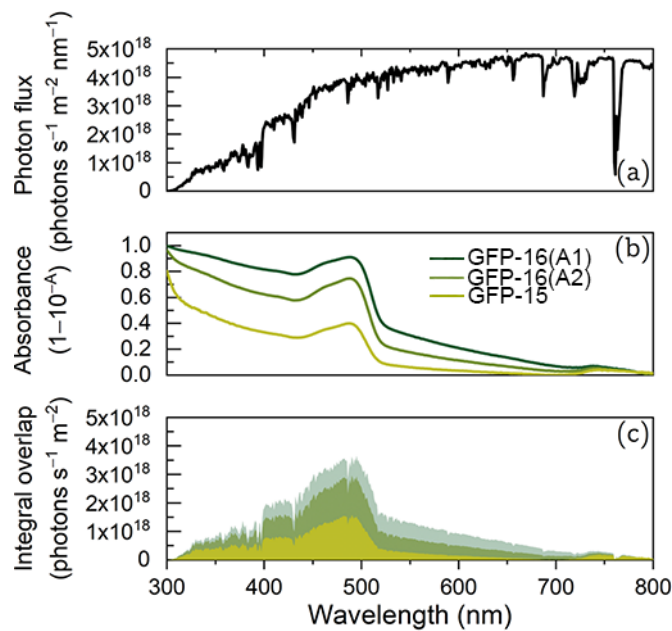

Figure 6.5: LSCs' potential to absorb the solar photon flux on the Earth. (a) Solar photon flux on Earth at AM1.5G; (b) absolute absorbance of the GFP-16(A1), GFP-16(A2) and GFP-15 solutions; and (c) integral overlap between the solar photon flux and the absolute absorbance.

Bulk eGFP-doped di-ureasil p-LSC

The second prototyped tested and was a eGFP-doped bulk planar LSC, consisting of dU(600)-GFP monolithcharacterised sample, attached to a PV cell in one of its edges. Figure 6.6(a) shows the planar LSC under the solar simulator, where the green emission in the visible spectral region of the latter ascribed to eGFP transitions is clearly noticeable. The dimensions of the LSC are detailed in Figure 6.6(b). As the monolith had smaller dimensions than the PV cell used (same as the one of Figure 6.2(c)), a mask was applied on the area of the cell not covered by the LSC.

(a)   (b)
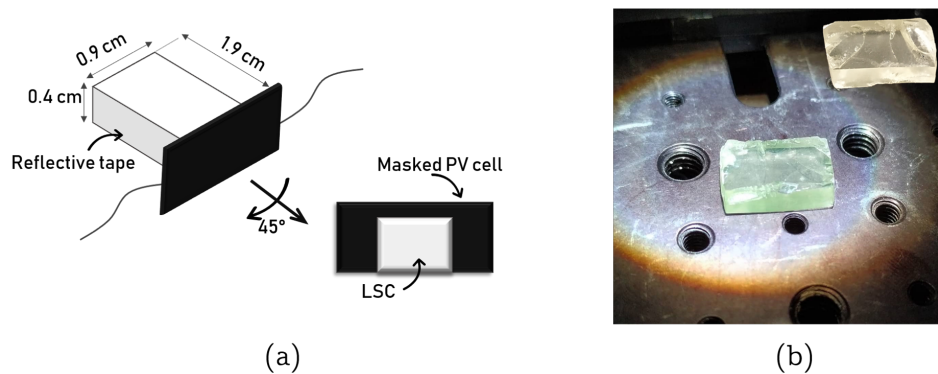
Figure 6.6: (a) Schematic representation of the same p-LSC, specifying its dimensions and coupling to the PV cell. (b) Photograph of the bulk eGFP-doped di-ureasil LSC under the solar simulator. The inset shows the transparent LSC under white light, for easier comparison.

The LSC's performance was likewise quantified through η_{opt}, F and EQE calculations, yielding a η_{opt} of $3.7 \pm 0.1\%$ and $F = 0.170 \pm 0.002$ with the reflective tape on all the edges and in the back of the LSC and $\eta_{\text{opt}} = 3.4 \pm 0.1\%$ and $F = 0.160 \pm 0.007$ without the reflective tape. Three measurements were performed, so that the average value is reported and the device as geometrical gain factor $G = 5$. EQE values were calculated between 300-800 nm, Figure 6.7(a). Unlike the liquid LSC, the shoulder between 450 and 520 nm ascribed to eGFP absorption is not detected for
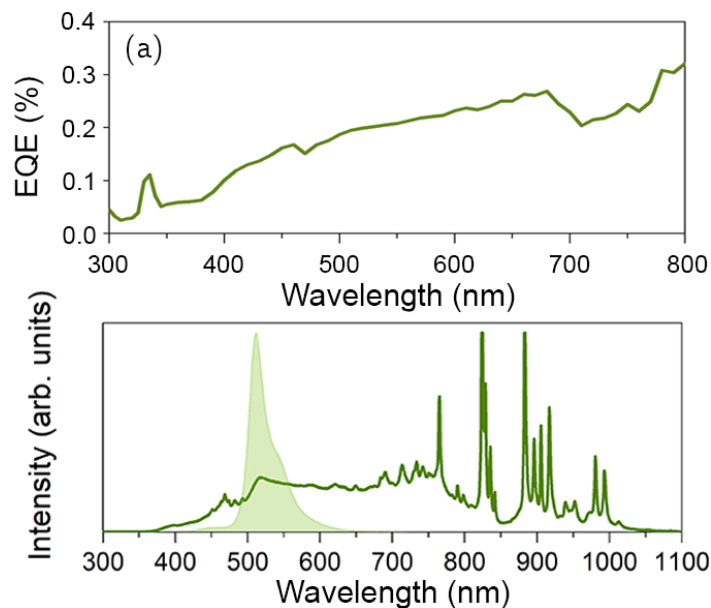

Figure 6.7: (a) Calculated EQE curve for the eGFP-doped bulk LSC; and (b) emission spectra recorded at the edge of the LSC, where the PV cell was attached. The latter was overlapped with the emission spectrum of the GFP-16(A1) solution (excited at 390 nm), to better visualise the peak ascribed to eGFP emission.

the bulk prototype, which means the number of photons reaching the PV cell didn't increase in a noticeable way when exciting the sample at eGFP absorption wavelengths.

However, the emission spectrum at the edge of the monolith where the PV cell is placed, Figure 6.7(b), showcased the emission peak at 515 nm attributed to eGFP emission. Although the EQE curve didn't showcase any eGFP related absorption, this emission peak indicates that the incident solar radiation is absorbed by the eGFP molecules incorporated in the organic-inorganic hybrid and then re-emitted, even though the number of solar photons reaching the cell is higher. This explains the big difference between the simulated and calculated η_{opt} values for this prototype – as no solar photons were collected in the PV cell in the simulations, the resulting η_{opt} was much lower than the experimental value.

The overlap integral O was also calculated for the bulk LSC, as shown in Figure 6.7, yielding 9.77×10^{19} photons s^{-1} m^{-2}. The O value is smaller than that of the GFP-16(A1) aqueous solution, that shares the same eGFP concentration, $\sim 2\%$.
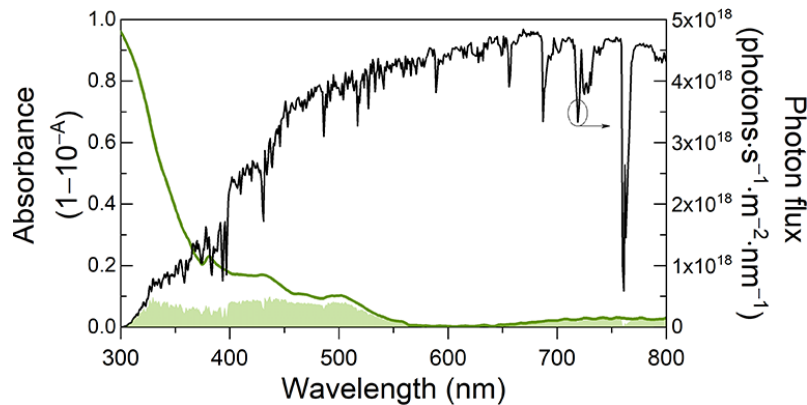

Figure 6.8: Overlap integral between the absorption spectra of the bulk LSC and the solar irradiation on Earth. Absolute absorbance of the eGFP-doped d-U(600) organic-inorganic hybrid tested as LSC and AM1.5G photon flux (right y axis). The shadowed area represents the overlap integral O.

To compare the η_{opt} values here reported with those in the literature, care must be taken in what concerns the LSC geometry and the use of external devices to enhance LSC performance, as all these aspects directly contribute to η_{opt}, as well as how η_{opt} itself is defined and calculated.

Considering LSCs based on natural organic dyes, the η_{opt} values of the liquid p-LSCs here described are lower ($\sim 2.99 - 2.07\%$) than those recently reported for a p-LSC based on R-phycoerythrin with the same architecture, $\eta_{opt} = 5.6 \pm 0.2\%$ [13]. In comparison with other p-LSCs with synthetic dyes or QDs in organic solvents (see Table 2 of ref. [13]), the η_{opt} values calculated in the present work are within the state of the art values in literature. Additionally, a liquid LSC containing a red fluorescent protein dispersed in water was recently reported [50], as mentioned, with $\eta_{opt} \sim 2.58\%$. The η_{opt} definition adopted, however, was different than that given in Eq. 2.7 and adopted in this thesis.

The bulk, eGFP-doped, di-ureasil organic hybrid sample has a higher η_{opt} value, $3.7 \pm 0.1\%$, that the liquid p-LSCs, with $\eta_{opt} = 3.4 \pm 0.1\%$ without the reflective tape. The latter can be directly compared to that recently reported for a di-ureasil p-LSC doped with chlorophyll, $\eta_{opt} \sim 3.70\%$ [21].

These results highlight the potential of the eGFP-based hybrids for LSCs applications, demonstrating the aptness of nature-inspired LSCs for sustainable PV energy conversion.

7. General conclusions

This thesis has presented a study of a range of aspects concerning LSCs and the relevant optical features of the optical active layers. In particular, the principle of operation, loss mechanisms and performance quantification of these devices; the optical study of two different natural based-dyes and sol-gel derived organic–inorganic hybrids, proposed as luminophores and respective host matrices in LSCs; Monte Carlo ray-tracing simulations; and the design, construction and performance quantification of two planar LSCs. The important findings are summarised below.

Towards the design of efficient LSCs, the natural dyes' and organic-inorganic's excited states dynamics were studied and characterised. The Soret and Q absorption bands of chlorophyll a, implied by Gouterman's four-orbital model, were identified for both the chlorophyll in solution and the doped monoliths, as well as its characteristic emission in the red spectral region (665 nm). Analogous data were collected for the eGFP-based samples, where the A, I and B excited states were identified, as well as the eGFP characteristic green emission ($\sim$510 nm). The hybrid host intrinsic emission in the blue/green spectral region was also identified for both the chlorophyll- and eGFP-doped hybrids. The emission properties were further quantified through absolute emission quantum yield measurements – higher quantum yield values were found for the chlorophyll-doped hybrids when the excitation wavelength was resonant with the Soret band (maximum values of 0.15 ± 0.02); in the case of the eGFP-based samples, higher quantum yield values were found when monitoring within the protein's excitation maxima (488 nm). The values were also higher for the eGFP in aqueous solutions ($\sim$0.5) than for the dU(600) sample (0.33 ± 0.03), suggesting a quenching of eGFP emission after its incorporation into the hybrid host. Moreover, fluorescent lifetime analysis was also performed for all samples resorting to two different techniques: time-correlated single photon counting (TCSPC) and spectrally-resolved streak imaging. For chlorophyll, fluorescent lifetimes of $\sim$ 5 ns and $\sim$10-12 ns were measured when monitoring chlorophyll a and the hybrid host emission at room temperature, respectively. For the eGFP-based samples, different fluorescent lifetimes were found when exciting the eGFP solutions within the A absorption band (390 nm) and monitoring at 510 nm (TCSPC studies) – 3.33-3.41 ns – and within the overlapped I and B bans (467 nm), monitoring in the whole range of eGFP emission (streak camera measurements) – 2.89-2.94 ns. A further analysis of the decay curves measured with the streak camera was carried out by applying a two exponential decay model, since the electronic model of eGFP indicates the presence of two distinct fluorescent electronic states, resulting in $\tau_1 \sim 3$ ns and $\tau_2 \sim 2$ ns, in good agreement with the literature.

The synergy between the intrinsic characteristics of sol-gel derived organic–inorganic hybrids, combined with the easy incorporation and processing of the luminescent species, confirmed the real potential of hybrid materials for LSC applications. As such, Monte Carlo ray-tracing simulations were performed, as these studies are an important tool in the assessment of the LSC's performance and in design optimisation. The open source program pvtrace was used to simulate planar LSC. To further use this free software for modelling real devices, future research should be directed to the modification of the code to enable a more real approximation to the experimental conditions (e.g. wavelength dependent refractive index and fluorescent quantum yield).

Lastly, LSC prototypes with eGFP as a luminophore were developed, consequence of the favourable characteristics of this protein towards LSC technologies – eco-friendly nature, high absorption coefficient and emission quantum yield – not yet explored in the literature. The first planar LSCs prototype was based on a glass container filled with eGFP dispersed in aqueous solutions in three different concentrations, resulting in η_{opt} values between 1.27 and 3.27%, with solution volumes ranging from 1 to 8 $\times 10^{-6} \mathrm{m}^3$. Then, a second planar LSC, whose optically active layer was based in a d-U(600) hybrid doped with eGFP, showed an η_{opt} value 3.7%. Both attest for the promising use of eGFP as a luminophore in LSCs, resulting in η_{opt} values within the state of the art values reported in the literature for other planar LSCs and luminescent centres. Furthermore, the eGFP-doped organic hybrid sample had higher η_{opt} the liquid LSC consisting of eGFP in solution, highlighting the potential of these materials as host matrices in LSC applications.

Future perspectives

Although LSC have the potential to reduce the costs of harvesting solar energy, improvements on their efficiency must be made to achieve widespread commercialization. One way to improve the described LSCs' performance could be through architecture alterations. The cylindrical geometry has a large potential, compared with that of planar LSC [13, 38–41], as the ratio between the absorption and collection areas is greater, yielding higher concentration factors F. Another advantage of the cylindrical geometry is that it allows for easier coupling with optical fibres, possibly allowing easier urban integration of PV technology. Moreover, the photostability of the reported LSCs also needs to be assessed, to confirm their applicability in LSCs, although previous studies already demonstrated the ability of the organic–inorganic hybrid hosts to efficiently incorporate and stabilize organic dyes and lanthanide-based organic complexes for LSC applications [21, 75].

In more general therms, some future research themes deserving of particular attention are:

i Luminophores. After several decades of research, there is still no material reported that combines all the requirements for an effective luminophore – organic dyes have small spectral absorption width and low Stokes shift values, while quantum dots have low quantum yields, and rare earth materials present both low absorption coefficients and low quantum yields.

ii LSC host matrix. Research on alternative matrix materials for LSCs has been addressed only in recent years and to a lesser extent than the luminescent species, and therefore performance enhancement of these devices can be achieved by developing suitably tailored host materials. Recent efforts in the field of LSCs include the development of multifunctional systems in which the matrix material not only acts as host environment for the luminophore, but also displays added functionalities, e.g. higher outdoor durability [142] and thermo-responsive properties [143].

iii New device architectures. The most commonly studied architecture is a planar luminescent waveguide, with the PV cells attached at the plate edges. Recently, alternative architectures have been investigated towards further improvements on the conversion efficiency of these devices, with the possibility of increasing functionality or facilitating PV integration [23]. Examples of new architectures proposed recently are the above-mentioned cylindrical geometry and liquid LSCs [50].

iv Environmental and sustainability concerns. To avoid substituting current harmful energy production technologies with new, albeit less harmful, ones that nonetheless have negative impacts on the environment (e.g. using non-renewable or non-recyclable resources), these also need to be regarded in the scope of the forthcoming research, to avoid future sustainability or waste management issues.

Bibliography

(1) *Energy and Climate Change - World Energy Outlook Special Report*; International Energy Agency, 2015.

(2) World Energy Council *World Energy Resources: 2013 Survey*; 2013.

(3) Miller, R. G.; Sorrell, S. R. *Philos. Trans. R. Soc. A-Math. Phys. Eng. Sci.* **2013**, *372*.

(4) *World Energy Outlook 2018*; International Energy Agency, 2018, pp 38–46.

(5) Krauter, S. C. W., *Solar Electric Power Generation*; Springer Berlin Heidelberg: 2006.

(6) Fraunhofer Institute for Solar Energy and Systems (ISE) *Photovoltaics Report*; 2019.

(7) Meinardi, F.; Ehrenberg, S.; Dhamo, L.; Carulli, F.; Mauri, M.; Bruni, F.; Simonutti, R.; Kortshagen, U.; Brovelli, S. *Nat. Photonics* **2017**, *11*, 177–185.

(8) Meinardi, F.; Bruni, F.; Brovelli, S. *Nat. Rev. Mater.* **2017**, *2*.

(9) European Comission. `https://ec.europa.eu/energy/en/topics/energy-efficiency/energy-performance-of-buildings` (accessed 06/2019).

(10) *Off. J. Eur. Union* **2010**, *18*, 13–35.

(11) Weber, W. H.; Lambe, J. *Appl. Opt.* **1976**, *15*, 2299–300.

(12) Goetzberger, A.; Greube, W. *Appl. Phys. A-Mater. Sci. Process.* **1977**, *14*, 123–139.

(13) Frias, A. R.; Correia, S. F. H.; Martins, M.; Ventura, S. P. M.; Pecoraro, E.; Ribeiro, S. J. L.; André, P. S.; Ferreira, R. A. S.; Coutinho, J. A. P.; Carlos, L. D. *Adv. Sustain. Syst.* **2019**, *3*, 1800134.

(14) Debije, M. G.; Verbunt, P. P. C. *Adv. Energy Mater.* **2012**, *2*, 12–35.

(15) Goetzberger, A.; Wittwer, V. *Sol. Cells* **1981**, *4*, 3–23.

(16) Lifante, G.; Cusso, F.; Meseguer, F.; Jaque, F. *Appl. Opt.* **1983**, *22*, 3966.

(17) Needell, D. R.; Ilic, O.; Bukowsky, C. R.; Nett, Z.; Xu, L.; He, J.; Bauser, H.; Lee, B. G.; Geisz, J. F.; Nuzzo, R. G.; Alivisatos, A. P.; Atwater, H. A. *IEEE J. Photovolt.* **2018**, *8*, 1560–1567.

(18) Pucci, A. *Isr. J. Chem.* **2018**, *58*, 837–844.

(19) Meinardi, F.; McDaniel, H.; Carulli, F.; Colombo, A.; Velizhanin, K. A.; Makarov, N. S.; Simonutti, R.; Klimov, V. I.; Brovelli, S. *Nat. Nanotechnol.* **2015**, *10*, 878–885.

(20) Zhao, Y.; Meek, G. A.; Levine, B. G.; Lunt, R. R. *Adv. Opt. Mater.* **2014**, *2*, 606–611.

(21) Frias, A. R.; Pecoraro, E.; Correia, S. F. H.; Minas, L. M. G.; Bastos, A. R.; García-Revilla, S.; Balda, R.; Ribeiro, S. J. L.; André, P. S.; Carlos, L. D.; Ferreira, R. A. S. *J. Mater. Chem.A* **2018**, *6*, 8712–8723.

(22) Debije, M. G. *Adv. Funct. Mater.* **2010**, *20*, 1498–1502.

(23) McKenna, B.; Evans, R. C. *Adv. Mater.* **2017**, *29*, 1606491.

(24) Bergren, M. R.; Makarov, N. S.; Ramasamy, K.; Jackson, A.; Guglielmetti, R.; McDaniel, H. *ACS Energy Lett.* **2018**, *3*, 520–525.

(25) Vasiliev, M.; Alameh, K.; Badshah, M.; Kim, S.-M.; Nur-E-Alam, M. *Photonics* **2018**, *5*, 25.

(26) Griffini, G. *Front. Mater.* **2019**, *6*.

(27) UbiQD, Inc. `https://ubiqd.com/` (accessed 06/2019).

(28) The Palais des congres de Montreal. `https://www.alamy.com/stock-photo/palais-congr%C3%A8s-montreal.html` (accessed 06/2019).

(29) The Kuggen. `https://www.archdaily.com` (accessed 06/2019).

(30)   Marina Bay Sands. `www.marinabaysands.com` (accessed 06/2019).

(31)   Bus shelter was installed in Rome, at the Eni's building. `https://energycue.it/en/luminescent-solar-concentrator-lsc/9655/` (accessed 06/2009).

(32)   Corrado, C.; Leow, S. W.; Osborn, M.; Carbone, I.; Hellier, K.; Short, M.; Alers, G.; Carter, S. A. *J. Renewable Sustainable Energy* **2016**, *8*, 043502.

(33)   Kanellis, M.; de Jong, M. M.; Slooff, L.; Debije, M. G. *Renew. Energy* **2017**, *103*, 647–652.

(34)   Tsien, R. Y. *Annu. Rev. Biochem.* **1998**, *67*, 509–544.

(35)   Mazzaro, R.; Vomiero, A. *Adv. Energy Mater.* **2018**, *8*, 1801903.

(36)   Moraitis, P.; Schropp, R.; van Sark, W. *Opt. Mater.* **2018**, *84*, 636–645.

(37)   Correia, S. F. H.; de Zea Bermudez, V.; Ribeiro, S. J. L.; André, P. S.; Ferreira, R. A. S.; Carlos, L. D. *J. Mater. Chem. A* **2014**, *2*, 5580–5596.

(38)   McIntosh, K.; Yamada, N.; Richards, B. *Appl. Phys. B* **2007**, *88*, 285–290.

(39)   Edelenbosch, O. Y.; Fisher, M.; Patrignani, L.; van Sark, W. G. J. H. M.; Chatten, A. J. *Opt. Express* **2013**, *21*, A503.

(40)   Videira, J. J. H.; Bilotti, E.; Chatten, A. J. *Opt. Express* **2016**, *24*, A1188.

(41)   Correia, S. F. H.; Lima, P. P.; Pecoraro, E.; Ribeiro, S. J. L.; André, P. S.; Ferreira, R. A. S.; Carlos, L. D. *Prog. Photovoltaics Res. Appl.* **2016**, *24*, 1178–1193.

(42)   Zhao, Y.; Lunt, R. R. *Adv. Energy Mater.* **2013**, *3*, 1143–1148.

(43)   Kaniyoor, A.; McKenna, B.; Comby, S.; Evans, R. C. *Adv. Opt. Mater.* **2015**, *4*, 444–456.

(44)   Demmig-Adams, B.; Adams, W. W. *Nature* **2000**, *403*, 371–373.

(45)   Nienhaus, G. U. *Angew. Chem.-Int. Edit.* **2008**, *47*, 8992–8994.

(46)   Weber, M. D.; Niklaus, L.; Pröschel, M.; Coto, P. B.; Sonnewald, U.; Costa, R. D. *Adv. Mater.* **2015**, *27*, 5493–5498.

(47)   Dogru, I. B.; Min, K.; Umar, M.; Jalali, H. B.; Begar, E.; Conkar, D.; Karalar, E. N. F.; Kim, S.; Nizamoglu, S. *Appl. Phys. Lett.* **2017**, *111*, 231103.

(48)   Chalfie, M.; Tu, Y.; Euskirchen, G.; Ward, W.; Prasher, D. *Science* **1994**, *263*, 802–805.

(49)   Richards, H. A.; Han, C.-T.; Hopkins, R. G.; Failla, M. L.; Ward, W. W.; Stewart, C. N. *J. Nutr.* **2003**, *133*, 1909–1912.

(50)   Sadeghi, S.; Melikov, R.; Jalali, H. B.; Karatum, O.; Srivastava, S. B.; Conkar, D.; Firat-Karalar, E. N.; Nizamoglu, S. *ACS Appl. Mater. Interfaces* **2019**, *11*, 8710–8716.

(51)   Kastelijn, M. J.; Bastiaansen, C. W.; Debije, M. G. *Opt. Mater.* **2009**, *31*, 1720–1722.

(52)   Zettl, M.; Mayer, O.; Klampaftis, E.; Richards, B. S. *Energy Technol.* **2017**, *5*, 1037–1044.

(53)   Griffini, G.; Levi, M.; Turri, S. *Sol. Energy Mater. Sol. Cells* **2013**, *118*, 36–42.

(54)   Lim, Y. S.; Lo, C. K.; Teh, G. B. *Renew. Energy* **2012**, *45*, 156–162.

(55)   Maggioni, G.; Campagnaro, A.; Carturan, S.; Quaranta, A. *Sol. Energy Mater. Sol. Cells* **2013**, *108*, 27–37.

(56)   Tonezzer, M.; Maggioni, G.; Campagnaro, A.; Carturan, S.; Quaranta, A.; della Pirriera, M.; Tauste, D. G. *Prog. Photovoltaics Res. Appl.* **2014**, *23*, 1037–1044.

(57)   Fattori, V.; Melucci, M.; Ferrante, L.; Zambianchi, M.; Manet, I.; Oberhauser, W.; Giambastiani, G.; Frediani, M.; Giachi, G.; Camaioni, N. *Energy Environ. Sci.* **2011**, *4*, 2849.

(58)   Melucci, M.; Durso, M.; Favaretto, L.; Capobianco, M. L.; Benfenati, V.; Sagnella, A.; Ruani, G.; Muccini, M.; Zamboni, R.; Fattori, V.; Camaioni, N. *RSC Adv.* **2012**, *2*, 8610.

(59)   Chowdhury, F. I.; Dick, C.; Meng, L.; Mahpeykar, S. M.; Ahvazi, B.; Wang, X. *RSC Adv.* **2017**, *7*, 32436–32441.

(60)   Geervliet, T. A.; Gavrila, I.; Iasilli, G.; Picchioni, F.; Pucci, A. *Chem. Asian J.* **2018**, *14*, 877–883.

(61) Wen, J.; Wilkes, G. L. *Chem. Mater.* **1996**, *8*, 1667–1681.

(62) Sanchez, C.; Lebeau, B.; Chaput, F.; Boilot, J.-P. *Adv. Mater.* **2003**, *15*, 1969–1994.

(63) Sanchez, C.; Julián, B.; Belleville, P.; Popall, M. *J. Mater. Chem.* **2005**, *15*, 3559.

(64) Reisfeld, R.; Levchenko, V.; Saraidarov, T. *Polym. Adv. Technol.* **2010**, *22*, 60–64.

(65) Pandey, S.; Mishra, S. B. *J. Sol-Gel Sci. Technol.* **2011**, *59*, 73–94.

(66) Parola, S.; Julián-López, B.; Carlos, L. D.; Sanchez, C. *Adv. Funct. Mater.* **2016**, *26*, 6506–6544.

(67) Rey-García, F.; Gómez-Reino, C.; Flores-Arias, M.; Fuente, G. D. L.; Durán, A.; Castro, Y. *Thin Solid Films* **2011**, *519*, 7982–7986.

(68) Graffion, J.; Cattoën, X.; Man, M. W. C.; Fernandes, V. R.; André, P. S.; Ferreira, R. A. S.; Carlos, L. D. *Chem. Mater.* **2011**, *23*, 4773–4782.

(69) Graffion, J.; Cojocariu, A. M.; Cattoën, X.; Ferreira, R. A. S.; Fernandes, V. R.; André, P. S.; Carlos, L. D.; Man, M. W. C.; Bartlett, J. R. *J. Mater. Chem.* **2012**, *22*, 13279.

(70) Freitas, V. T.; Fu, L.; Cojocariu, A. M.; Cattoën, X.; Bartlett, J. R.; Parc, R. L.; Bantignies, J.-L.; Man, M. W. C.; André, P. S.; Ferreira, R. A. S.; Carlos, L. D. *ACS Appl. Mater. Interfaces* **2015**, *7*, 8770–8778.

(71) Santilli, C. V.; Chiavacci, L. A.; Lopes, L.; Pulcinelli, S. H.; Oliveira, A. G. *Chem. Mater.* **2009**, *21*, 463–467.

(72) Nolasco, M. M.; Vaz, P. M.; Freitas, V. T.; Lima, P. P.; André, P. S.; Ferreira, R. A. S.; Vaz, P. D.; Ribeiro-Claro, P.; Carlos, L. D. *J. Mater. Chem.A* **2013**, *1*, 7339.

(73) Rondão, R.; Frias, A. R.; Correia, S. F. H.; Fu, L.; de Zea Bermudez, V.; André, P. S.; Ferreira, R. A. S.; Carlos, L. D. *ACS Appl. Mater. Interfaces* **2017**, *9*, 12540–12546.

(74) Meazzini, I.; Blayo, C.; Arlt, J.; Marques, A.-T.; Scherf, U.; Burrows, H. D.; Evans, R. C. *Mater. Chem. Front.* **2017**, *1*, 2271–2282.

(75) Correia, S. F.; Lima, P. P.; André, P. S.; Ferreira, M. R. S.; Carlos, L. A. D. *Sol. Energy Mater. Sol. Cells* **2015**, *138*, 51–57.

(76) Bernard Valeur, M. N. B.-S., *Molecular Fluorescence: Principles and Applications*; Wiley VCH Verlag GmbH: 2012.

(77) Douglas, P.; Burrows, H. D.; Evans, R. C. In *Applied Photochemistry*, Evans, R. C., Douglas, P., Burrow, H. D., Eds.; Springer Netherlands: Dordrecht, 2013, pp 1–88.

(78) Jain, A.; Blum, C.; Subramaniam, V. In *Advances in Biomedical Engineering*, Verdonck, P., Ed.; Elsevier: Amsterdam, 2009; Chapter 4, pp 147–176.

(79) Hughes, M. D.; Maher, C.; Borca-Tasciuc, D.-A.; Polanco, D.; Kaminski, D. *Renew. Energy* **2013**, *52*, 266–272.

(80) Purcell-Milton, F.; Gun'ko, Y. K. *J. Mater. Chem.* **2012**, *22*, 16687.

(81) Reisfeld, R.; Jørgensen, C. K. In *Structure and Bonding*; Springer Berlin Heidelberg: 1982, pp 1–36.

(82) Reisfeld, R.; Shamrakov, D.; Jorgensen, C. *Sol. Energy Mater. Sol. Cells* **1994**, *33*, 417–427.

(83) Coropceanu, I.; Bawendi, M. G. *Nano Lett.* **2014**, *14*, 4097–4101.

(84) Bomm, J.; Büchtemann, A.; Chatten, A. J.; Bose, R.; Farrell, D. J.; Chan, N. L.; Xiao, Y.; Slooff, L. H.; Meyer, T.; Meyer, A.; van Sark, W. G.; Koole, R. *Sol. Energy Mater. Sol. Cells* **2011**, *95*, 2087–2094.

(85) Carlos, L. D.; Ferreira, R. A. S.; de Zea Bermudez, V.; Ribeiro, S. J. L. *Adv. Mater.* **2008**, *21*, 509–534.

(86) Niedzwiedzki, D. M.; Blankenship, R. E. *Photosynth. Res.* **2010**, *106*, 227–238.

(87) Kee, H. L.; Kirmaier, C.; Tang, Q.; Diers, J. R.; Muthiah, C.; Taniguchi, M.; Laha, J. K.; Ptaszek, M.; Lindsey, J. S.; Bocian, D. F.; Holten, D. *Photochem. Photobiol.* **2007**, *83*, 1110–1124.

(88) Frommer, W. B.; Davidson, M. W.; Campbell, R. E. *Chem. Soc. Rev.* **2009**, *38*, 2833.

(89) Heikal, A. A.; Hess, S. T.; Webb, W. W. *Chem. Phys.* **2001**, *274*, 37–55.

(90) Bublitz, G.; King, B. A.; Boxer, S. G. *J. Am. Chem. Soc.* **1998**, *120*, 9370–9371.

(91) Heim, R.; Prasher, D. C.; Tsien, R. Y. *Proc. Natl. Acad. Sci. U. S. A.* **1994**, *91*, 12501–12504.

(92) Martins, M.; Ooi, C. W.; Neves, M.; Pereira, J. F.; Coutinho, J. A.; Ventura, S. *J. Chem. Technol. Biotechnol.* **2018**, *93*, 1864–1870.

(93) Dos Santos, N. V.; Martins, M.; Santos-Ebinuma, V. C.; Ventura, S. P. M.; Coutinho, J. A. P.; Valentini, S. R.; Pereira, J. F. B. *ACS Sustain. Chem. Eng.* **2018**, *6*, 9383–9393.

(94) Hench, L. L.; West, J. K. *Chem. Rev.* **1990**, *90*, 33–72.

(95) Cushing, B. L.; Kolesnichenko, V. L.; O'Connor, C. J. *Chem. Rev.* **2004**, *104*, 3893–3946.

(96) Gouterman, M. *J. Mol. Spectrosc.* **1961**, *6*, 138–163.

(97) Weiss, C. *J. Mol. Spectrosc.* **1972**, *44*, 37–80.

(98) Shipman, L. L.; Cotton, T. M.; Norris, J. R.; Katz, J. J. *J. Am. Chem. Soc.* **1976**, *98*, 8222–8230.

(99) Lichtenthaler, H. K. In *Methods in Enzymology*; Elsevier: 1987, pp 350–382.

(100) Kobayashi, M.; Akiyama, M.; Kano, H.; Kise, H. In *Chlorophylls and Bacteriochlorophylls*, Grimm, B., Porra, R. J., Rudiger, W., Scheer, H., Eds., 2006; Chapter 6.

(101) Bricker, W. P.; Shenai, P. M.; Ghosh, A.; Liu, Z.; Enriquez, M. G. M.; Lambrev, P. H.; Tan, H.-S.; Lo, C. S.; Tretiak, S.; Fernandez-Alberti, S.; Zhao, Y. *Sci. Rep.* **2015**, *5*, 13625.

(102) *Chlorophylls and Bacteriochlorophylls*; Grimm, B., Porra, R. J., Rüdiger, W., Scheer, H., Eds.; Springer Netherlands: 2006.

(103) Chen, M.; Blankenship, R. E. *Trends Plant Sci.* **2011**, *16*, 427–431.

(104) Carlos, L. D.; de Zea Bermudez, V.; Ferreira, R. A. S.; Marques, L.; Assunção, M. *Chem. Mater.* **1999**, *11*, 581–588.

(105) Murata, N.; Nishimura, M.; Takamiya, A. *Biochim. Biophys. Acta, Biophys. Incl. Photsynth.* **1966**, *126*, 234–243.

(106) Pfarrherr, A.; Teuchner, K.; Leupold, D.; Hoffmann, P. *J. Photochem. Photobiol., B* **1991**, *9*, 35–41.

(107) Shi, Y.; Liu, J.-Y.; Han, K.-L. *Chem. Phys. Lett.* **2005**, *410*, 260–263.

(108) Porcar-Castell, A.; Tyystjärvi, E.; Atherton, J.; van der Tol, C.; Flexas, J.; Pfündel, E. E.; Moreno, J.; Frankenberg, C.; Berry, J. A. *J. Exp. Bot.* **2014**, *65*, 4065–4095.

(109) Schweiger, J.; Lang, M.; Lichtenthaler, H. K. *J. Plant Physiol.* **1996**, *148*, 536–547.

(110) Adb El Baky, H.; K. El Baz, F.; El baroty, G. *Afr. J. Pharm. Pharmacol.* **2009**, *3*, 133–139.

(111) Carlos, L. D.; Ferreira, R. A. S.; Bermudez, V. D. Z.; Ribeiro, S. J. L. *Adv. Funct. Mater.* **2001**, *11*, 111–115.

(112) Freitas, V. T.; Lima, P. P.; Ferreira, R. A. S.; Pecoraro, E.; Fernandes, M.; de Zea Bermudez, V.; Carlos, L. D. *J. Sol-Gel Sci. Technol.* **2012**, *65*, 83–92.

(113) Carlos, L. D.; Ferreira, R. A. S.; Pereira, R. N.; Assunção, M.; de Zea Bermudez, V. *J. Phys. Chem. B* **2004**, *108*, 14924–14932.

(114) Nobre, S. S.; Lima, P. P.; Mafra, L.; Ferreira, R. A. S.; Freire, R. O.; Fu, L.; Pischel, U.; de Zea Bermudez, V.; Malta, O. L.; Carlos, L. D. *J. Phys. Chem. C* **2007**, *111*, 3275–3284.

(115) Brody, S. S.; Rabinowitch, E. *Science* **1957**, *125*, 555–555.

(116) Morales, F.; Cerovic, Z. G.; Moya, I. *Functional Plant Biology* **1998**, *25*, 325.

(117) Fu, L.; Ferreira, R. S.; Fernandes, M.; Nunes, S.; de Zea Bermudez, V.; Hungerford, G.; Rocha, J.; Carlos, L. *Opt. Mater.* **2008**, *30*, 1058–1064.

(118) Lima, P. P.; Nobre, S. S.; Freire, R. O.; Júnior, S. A.; Ferreira, R. A. S.; Pischel, U.; Malta, O. L.; Carlos, L. D. *The Journal of Physical Chemistry C* **2007**, *111*, 17627–17634.

(119) Hasegawa, J.-Y.; Fujimoto, K.; Swerts, B.; Miyahara, T.; Nakatsuji, H. *J. Comput. Chem.* **2007**, *28*, 2443–2452.

(120) Chattoraj, M.; King, B. A.; Bublitz, G. U.; Boxer, S. G. *Proc. Natl. Acad. Sci. U. S. A.* **1996**, *93*, 8362–8367.

(121) Völker, S.; Creemers, T.; Lock, A.; Subramaniam, V.; Jovin, T. *Nat. Struct. Biol.* **1999**, *6*, 557–560.

(122) Tonge, P. J.; Meech, S. R. *J. Photochem. Photobiol. A-Chem.* **2009**, *205*, 1–11.

(123) Remington, S. J. *Protein Sci.* **2011**, *20*, 1509–1519.

(124) Cotlet, M.; Hofkens, J.; Maus, M.; Gensch, T.; der Auweraer, M. V.; Michiels, J.; Dirix, G.; Guyse, M. V.; Vanderleyden, J.; Visser, A. J. W. G.; Schryver, F. C. D. *J. Phys. Chem. B* **2001**, *105*, 4999–5006.

(125) Mason, J. D.; Cone, M. T.; Fry, E. S. *Applied Optics* **2016**, *55*, 7163.

(126) Lakowicz, J. R. In *Principles of Fluorescence Spectroscopy*; Springer US: 2006; Chapter 16, pp 529–575.

(127) Ghisaidoobe, A.; Chung, S. *Int. J. Mol. Sci.* **2014**, *15*, 22518–22538.

(128) Yang, H.; Xiao, X.; Zhao, X.; Wu, Y. In *Proceedings of the 5th International Conference on Advanced Design and Manufacturing Engineering*, Atlantis Press: 2015.

(129) Piatkevich, K. D.; Malashkevich, V. N.; Morozova, K. S.; Nemkovich, N. A.; Almo, S. C.; Verkhusha, V. V. *Sci. Rep.* **2013**, *3*, 1847.

(130) Ferreira, R. A. S.; Carlos, L. D.; Gonçalves, R. R.; Ribeiro, S. J. L.; de Zea Bermudez, V. *Chem. Mater.* **2001**, *13*, 2991–2998.

(131) Leiderman, P.; Huppert, D.; Agmon, N. *Biophys. J.* **2006**, *90*, 1009–1018.

(132) Patterson, G.; Knobel, S.; Sharif, W.; Kain, S.; Piston, D. *Biophys. J.* **1997**, *73*, 2782–2790.

(133) Cubitt, A. B.; Woollenweber, L. A.; Heim, R. In *Methods in Cell Biology*; Elsevier: 1998, pp 19–30.

(134) Heim, R.; Tsien, R. Y. *Current Biology* **1996**, *6*, 178–182.

(135) Butkevich, A. N.; Belov, V. N.; Kolmakov, K.; Sokolov, V. V.; Shojaei, H.; Sidenstein, S. C.; Kamin, D.; Matthias, J.; Vlijm, R.; Engelhardt, J.; Hell, S. W. *Chemistry - A European Journal* **2017**, *23*, 12114–12119.

(136) Suhling, K.; Siegel, J.; Phillips, D.; French, P. M.; Lévêque-Fort, S.; Webb, S. E.; Davis, D. M. *Biophys. J.* **2002**, *83*, 3589–3595.

(137) Striker, G.; Subramaniam, V.; Seidel, C. A. M.; Volkmer, A. *J. Phys. Chem. B* **1999**, *103*, 8612–8617.

(138) Leow, S. W.; Corrado, C.; Osborn, M.; Carter, S. A. Monte Carlo ray-tracing simulations of luminescent solar concentrators for building integrated photovoltaics., 2013.

(139) Leow, S. W.; Corrado, C.; Osborn, M.; Isaacson, M.; Alers, G.; Carter, S. A. *J. Appl. Phys.* **2013**, *113*, 214510.

(140) Farrell, D. J. pvtrace: optical ray tracing for luminescent materials and spectral converter photovoltaic devices. `http://github.com/danieljfarrell/pvtrace`.

(141) Hale, G. M.; Querry, M. R. *Applied Optics* **1973**, *12*, 555.

(142) Pintossi, D.; Colombo, A.; Levi, M.; Dragonetti, C.; Turri, S.; Griffini, G. *Journal of Materials Chemistry A* **2017**, *5*, 9067–9075.

(143) Sol, J. A. H. P.; Dehm, V.; Hecht, R.; Würthner, F.; Schenning, A. P. H. J.; Debije, M. G. *Angewandte Chemie* **2017**, *130*, 1042–1045.